Physics of Fluids

Hydro- and thermo-dynamic characteristics of a circular cylinder placed in mixed convection flow

Cite as: Physics of Fluids (in press) (2022); https://doi.org/10.1063/5.0119962
Submitted: 10 August 2022 • Accepted: 01 September 2022 • Accepted Manuscript Online: 03 September 2022

Hongjun Zhu, Jiawen Zhong and Bin Liu

Accepted to Phys. Fluids 10.1063/5.0119962

Hydro- and thermo-dynamic characteristics of a circular cylinder placed in mixed convection flow

Hongjun Zhu (朱红钧),[1,a] Jiawen Zhong (钟家文),[1] and Bin Liu (刘斌)[2]

[1]*State Key Laboratory of Oil and Gas Reservoir Geology and Exploitation, Southwest Petroleum University, 8 Xindu Road, Chengdu, Sichuan 610500, China*

[2]*Department of Aeronautics, Imperial College London, London SW7 2AZ, UK*

ABSTRACT: The fluid-thermal-structure interaction (FTSI) of a heated circular cylinder is numerically investigated at $Pr = 0.71$, $Re = 60$–160, and $Ri = 0$–2.0 in this article using the stabilized finite element method (FEM). The heat convection characteristics along the cylinder's surface in both forced and mixed convection subject to cross buoyancy are discussed and linked to the fluid instabilities. Additionally, the hydrodynamic characteristics are investigated in both time and frequency domains according to the strength of thermal cross buoyancy. Multiple harmonics of hydrodynamic coefficients and heat convection are identified from their frequency domains. Reynolds stresses are utilized to study the energy cascade of fluid kinetic energy and thermal energy via the fine-scale fluid fluctuation in the wake. Furthermore, the dynamic mode decomposition (DMD) technique is employed to extract the dominant spatial-temporal modes from the original field data. It is found that more linear DMD modes are required to accurately reconstruct the vorticity and temperature contours. It implies that strong nonlinear features exist in the wake and are influenced by the thermal buoyancy.

I. INTRODUCTION

Flow around a circular cylinder is usually accompanied with heat exchange in engineering applications. Based on the Richardson number ($Ri = Gr/Re^2$, where Gr and Re are the Grashof and Reynolds numbers, respectively), the heat exchange could be classified into three main categories: forced convection, natural convection and mixed convection. The vortex shedding of a circular cylinder in mixed convection is physically more complicated in comparison with that in forced or

[a]Author to whom correspondence should be addressed: zhuhj@swpu.edu.cn

natural convection owing to the combined effects of buoyancy and viscous force. The purpose of this article is not only to characterize the hydro-thermal mechanism of the wake subject to strong cross buoyancy but also to evaluate the feasibility of dynamic mode decomposition analysis in flow-temperature field reconstruction and prediction.

The von Kármán vortex street[1] behind a circular cylinder is frequently employed as a canonical case in literature to study the hydrodynamic instability in wake and has drawn a great attention among the fluid community. In the past, the studies of this wake instability primarily focus on the study of the isothermal flow in a wide range of Reynolds number (e.g. Roshko,[2] Abernathy and Kronauer,[3] Berger and Wille,[4] Bearman[5] and Williamson[6]). Before the onset of flow transition (e.g. *Re* approximately equals to 180 for a circular cylinder[7-9]), the flow is two dimensional, periodic and behaves as a dynamic system of limited circle. A sequence of alternatively shedding vortices from the upper and lower shear layers of the cylinder is observed. Because of the negligible influence of buoyancy effect on the fluid inertia, the hydrodynamics in forced convection is practically identical to those in an isothermal incompressible flow, except for the heat convection across the thermal boundary layers of a heated cylinder.

In thermal engineering, the hot and cool fluid media are usually separated by metal tubes. The primary objective in engineering design is to improve the heat exchange efficiency across the metal tubes. Schmidt and Wenner[10] were the first to report the local heat transfer along a circular cylinder. It is known that the maximum heat transfer can be found around the forward and rear stagnation points[11-14] and the distribution of heat convection and pressure in wake are symmetric with respect to the incoming flow in the forced convection. Whereas for the mixed convection, the thermal buoyancy effect is critical and can significantly perturb the vortex dynamics in wake. Therefore, the vortex formation and wake structure are completely dependent on *Re*, *Ri* and *Pr* numbers together and are influenced by the gravitational force. A strong cross-buoyancy effect may cause a significant asymmetry of the wake in the gravitational direction, because the direction of thermal buoyancy is opposite to the direction of gravity (same direction for a cooled cylinder). Hence, the most of the research done in the past can be divided into three areas, following the terminology used by Badr:[15-16] (1) parallel flow, (2) contra-flow, and (3) horizontal cross-flow.

For the parallel flow, Joshi and Sukhatme[17] compared the difference of the heat transfer characteristics between two types of thermal boundary conditions over a cylinder's surface: a constant temperature and a variable heat flux. They analyzed the heat transfer within the cylinder's boundary layer and the wall shear stress. It was found that the local Nusselt number ($Nu_{(\theta)}$) distribution, the wall shear stress and the separation point all increase proportionally with Ri number. Therefore the thermal buoyancy force must be considered when $Ri > 2$.[17] Chatterjee[18] also reported two phenomena in parallel flow: the suppression of flow separation occurring at relatively low Reynolds numbers (10–40) and the suppression of vortex shedding at a moderate Reynolds numbers (50–150). Further numerical simulations were carried out for Re = 10–40 and three different Prandtl numbers Pr = 0.71, 7 and 50 to compute the critical Ri number for the complete suppression of flow separation around the bluff bodies of circular and square shapes.[19] By comparing the results in literature,[20-21] it is realized that as the Re number increases, a higher Ri number (the thermal buoyancy effect in parallel flow) is required to suppress the vortex shedding behind a cylinder.

For the contra-flow, Hu and Koochesfahani[23] studied the vortex shedding and the wake structure behind a cylinder in both forced and mixed convection by changing the direction of gravity with respect to the incoming flow. When the Ri number is relatively small ($Ri \leq 0.31$), the vortex shedding process in the wake behind a heated cylinder is similar to that of an unheated cylinder. As the Ri number increases to 0.50, the wake vortex shedding process is "delayed" and the vortex structures are shed much further downstream. As the value of Ri number is close to the unity ($Ri > 0.72$), the concurrent shedding of smaller vortex structures is observed in the near wake of the heated cylinder. The smaller vortex structures are found to behave more like the "Kelvin–Helmholtz" vortices instead of the Kármán vortices. Therefore, the adjacent small vortices are found coalescing into the larger vortical structures further downstream. It is also found that the shedding frequency of the vortical structures in wake decreases with the increase of Ri. In practice, this result is the same as those reported in the previous works,[24-26] changing the temperature of cylinder instead of the direction of gravity. By changing the heated ($Ri > 0$) cylinder into a cooled ($Ri < 0$) one, the effect of countercurrent thermal buoyancy can also be achieved in parallel flow. Chang and Sa[24] reported that vortex stops shedding when $Gr > 1500$ ($Ri > 0.15$) at $Re = 100$. This is identified as a "breakdown of the Kármán vortex street" in wake. Parallel flow thermal buoyancy can inhibit the vortex shedding, whereas the contra-flow thermal buoyancy can induce the vortex-shedding mechanism. The same conclusion is also drawn by Hatanaka and Kawahara.[27]

For the horizontal cross-flow, one obvious phenomenon reported in experiments[28-30] and numerical simulations[15, 31-32] is that the coherent structure in wake is deflected aside due to the thermal cross buoyancy. In the early seventies last century, this effect was investigated to determine the global effects of the induced heat on the heat exchange coefficient.[28] It was reported that the heat transfer coefficient was influenced considerably by the buoyancy-driven flow when Ri > 0.2. Furthermore the variation of vorticity, pressure and local Nusselt number around the cylinder surface in horizontal cross-flow can be acquired from Badr's result.[15] By studying the temperature distribution within the wake, the researchers also concluded that this temperature distribution can be quite well approximated by the theoretical distribution for a diffusing line vortex.[29] Kieft et al.[30, 33-34] carried out many experiments and simulations to explain the reason of deflected vortex wake structure and the phenomenon of flow transition in wake.[35,36] In literature, it was found that the deflection of wake is caused by the baroclinic vorticity. The difference of vortex strength will lead to the drift rotation of the lower side vortex around the upper side vortex.[37] Biswas and Sarkar[38] and Sarkar et al.[13] also reported in their works that the thermal buoyancy makes the steady flow separation unsteady. By comparing with literature and experiments, they noticed that boundary layer overpassed the leading edge separation phenomenon at low Re, and the vortex formed on the upper wall boundary due to the high block ratio, 0.05. In the cross buoyancy configuration, the onset of vortex shedding induced by the thermal buoyancy is shown at relatively low Reynolds numbers (10–40).[18] Recently, Garg et al.[39] reported that when Ri number is between 1 and 2, the thermal buoyancy can inhibit the vortex-induced vibration (VIV) at a low Re number (Re=50) until a critical high Re number (Re=150). However, while the Ri number is between 3 and 4, the galloping of cylinder is observed for different Re numbers. Recently Liu and Zhu[32] also noticed a secondary VIV lock-in phenomenon in mixed convection and reported the energy transfer characteristics of a vibrating cylinder subject to the cross buoyancy.

Nowadays, as the advancement of computing technique, the availability of large-scale high-fidelity data is significantly boosted and widely accessible. The reduced order modeling techniques have been developed as a reliable and robust analytical tool to study the complex dynamics embedded in the high-fidelity data in the community of fluid mechanics.[40] Dynamic mode decomposition (DMD) is a robust and widely-accepted reduced order technique to extract and analyze the spatial-temporal modes of a dynamic system based on the time sequence of high-fidelity data. In the study of flow over a cylinder, Wang and Yu[41] used the DMD method to analyze the vortex shedding of a vibrating square column, and studied the effects of *St* and *Re* on the vibration modes. Tu et al.[42-43] applied the DMD method to experimental and numerical results of flow behind a plate with an elliptic front, and discussed the interaction between shear layers in wake.

In summary, the combined effect of Reynolds and Richardson numbers on the hydrodynamics and thermodynamics characteristics of a circular cylinder in mixed convective flow is far from well understood. Furthermore, to the best of the authors' knowledge, the modal analysis of the wake behind a heated cylinder in mixed convection flow subject to cross-buoyancy effect has not been studies in the past. Therefore, the main objectives of this article are to reveal the intrinsic relationship between the thermodynamics and hydrodynamics characteristics for a heated cylinder subject to cross buoyancy and to evaluate the nonlinear features in the wake using the DMD technique. The results in the reconstruction and prediction of flow-temperature field will provide a reference for the subsequent data mining analysis or AI of thermal-fluid-structure interaction. The structure of this article is organized as follow. The governing equations, problem setup, numerical formulations and code validation are introduced in Section II. Subsequently the results and discussion are presented in Section III. Finally the conclusions are drawn in Section IV.

II. PHYSICAL MODEL AND GOVERNING EQUATIONS

A. Governing equations and problem description

The unsteady Navier–Stokes equations are coupled with the conservation of energy equation via Boussinesq approximation in this work to simulate the heat transfer and flow around the circular cylinder. The governing equations and associated boundary and initial conditions are expressed as:

$$\nabla \cdot \boldsymbol{u} = 0 \qquad \forall \boldsymbol{x} \in \Omega^f(t) \tag{1a}$$

$$\rho\left(\partial_t \boldsymbol{u} + (\boldsymbol{u}\cdot\nabla)\boldsymbol{u}\right) = \nabla\cdot\boldsymbol{\sigma} + \rho\boldsymbol{g} \qquad \forall \boldsymbol{x} \in \Omega^f(t) \tag{1b}$$

$$\partial_t T + (\boldsymbol{u}\cdot\nabla)T = \alpha\nabla^2 T \qquad \forall \boldsymbol{x} \in \Omega^f(t) \tag{1c}$$

$$\boldsymbol{u} = \tilde{\boldsymbol{u}}; \quad T = \tilde{T} \qquad \forall \boldsymbol{x} \in \Gamma_D^f(t) \tag{1d}$$

$$\boldsymbol{\sigma}\cdot\boldsymbol{n} = \tilde{\boldsymbol{h}}; \quad \alpha(\nabla T)\cdot\boldsymbol{n} = \tilde{q} \qquad \forall \boldsymbol{x} \in \Gamma_N^f(t) \tag{1e}$$

$$\boldsymbol{u} = \tilde{\boldsymbol{u}}_0 \; ; \quad T = \tilde{T}_0 \qquad\qquad \forall \boldsymbol{x} \in \Omega^f(0) \tag{1f}$$

where $\boldsymbol{u}$ is the flow velocity vector, $\boldsymbol{x}$ is the position vector, ρ is the fluid density, p is the pressure, t is the flow time, $\boldsymbol{g} = [0, -g]' = [0, -9.81]'$ is the gravitational acceleration vector, $\boldsymbol{\sigma}$ is the Cauchy stress tensor, T is the temperature, α is the thermal diffusivity, $\tilde{\boldsymbol{u}}$ represents the prescribed flow velocity imposed along the boundaries, $\tilde{T}$ represents the prescribed temperature imposed along the boundaries, $\boldsymbol{n}$ is the unit outward normal vector of the element's edge, $\tilde{h}$ and $\tilde{q}$ are the prescribed convection transfer coefficient and heat flux along the boundaries, respectively, $\tilde{\boldsymbol{u}}_0$ represents the initial flow velocity, $\tilde{T}_0$ represents the initial temperature, and Γ_D and Γ_N denote the Dirichlet and Neumann domain boundaries, respectively. The term $\partial_t(\cdot)$ represents the partial derivative with respect to time. The Cauchy stress tensor ($\boldsymbol{\sigma}$) is a function of $\boldsymbol{u}$ and p and defined as:

$$\boldsymbol{\sigma} = -p\boldsymbol{I} + 2\mu\boldsymbol{\varepsilon} \tag{2a}$$

$$\boldsymbol{\varepsilon} = \frac{1}{2}\left[\nabla\boldsymbol{u} + (\nabla\boldsymbol{u})'\right] \tag{2b}$$

where $\boldsymbol{I}$ is the Kronecker matrix, μ is the dynamic viscosity, $\boldsymbol{\varepsilon}$ is the strain rate tensor, and the superscript (') is a transpose operator.

The non-dimensional force component is $C_D = 2F_D/\rho U_\infty^2 D$ and $C_L = 2F_L/\rho U_\infty^2 D$, where $\boldsymbol{F}$ (F_D, F_L) is the fluid force imparted to the elastically mounted cylinder in the streamwise and transverse directions. The temperature is normalized by the maximum temperature differences expressed as $T^* = (T\text{-}T_{in})/(T_w\text{-}T_{in})$, where the T^* is the normalized temperature, T_w and T_{in} represent the cylinder surface (maximum) and inlet (minimum) temperatures in the computational domain, respectively. The local Nusselt number $Nu_{(\theta)}$ of a specific location on the cylinder surface and the Nu of the entire cylinder surface are defined as:

$$Nu_{(\theta)} = -\nabla T^*_{(\theta)} \cdot \boldsymbol{n}_{(\theta)} \tag{3a}$$

$$Nu = \frac{1}{\ell}\int_{\theta=0}^{\ell} Nu_{(\theta)} d\theta \tag{3b}$$

Figure 1 illustrates the employed computational domain and associated boundaries. The circular cylinder is initially placed at the origin ($x = 0$, $y = 0$), and the computational domain extends 35D downstream and 10D upstream from the cylinder center. The cylinder are placed centrally in

Accepted to Phys. Fluids 10.1063/5.0119962

the transverse direction, $25D$ from both the upper and lower boundaries. Consequently, the blocking ratio is 2%, meeting the requirement of blocking ratio less than 6%.[44-45]

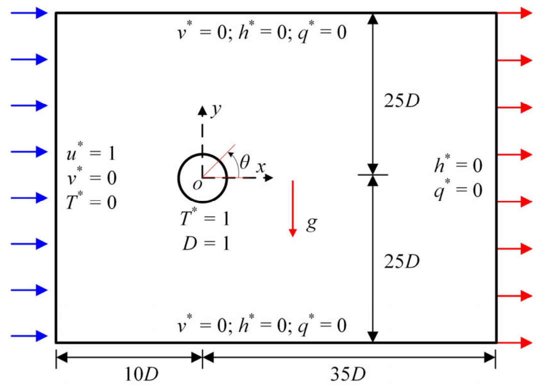

Figure 1. Schematic of the computational domain and associated boundary conditions.

The configuration of research in this article consists of a horizontal heated cylinder with constant wall temperature $T^*= 1$ and no-slip velocity boundary conditions, which is exposed to a uniform horizontal cross-flow with velocity $u^*= 1$, $v^* = 0$ and temperature $T^*= 0$. The Neumann-type boundary conditions ($h^* = 0$ and $q^* = 0$) are applied along the outlet. The two lateral boundaries are defined as the symmetry boundary condition with $v^* = 0$, $h^* = 0$ and $q^* = 0$. The Prandtl number are fixed at $Pr = 0.71$, and the Reynolds number of the heated cylinder is examined for $Re = 60–160$ with the Richardson number ranging from 0 to 2.

B. Finite-element mesh structure

In this investigation, the computational domain, $45D \times 50D$, is meshed by Gmsh in Fig. 2, where D is the diameter of the cylinder. A non-uniform grid distribution was employed with a more refined grid generated around three circular cylinders wall, and the smallest normalized grid height near the cylinder surface is set to 0.02 with $y^+ = 0.35$ less than 1. The grid was further refined along a rectangular region encompassing the cylinder to accurately capture the wake and vortex street behind the cylinder. A close-up view of the mesh around the cylinder is shown in Fig. 2. The mesh is made up of a structured part near the cylinder's surface, which is adequately refined to capture the boundary layer. The unstructured part of the mesh is created via Delaunay's triangulation technique.

Accepted to Phys. Fluids 10.1063/5.0119962

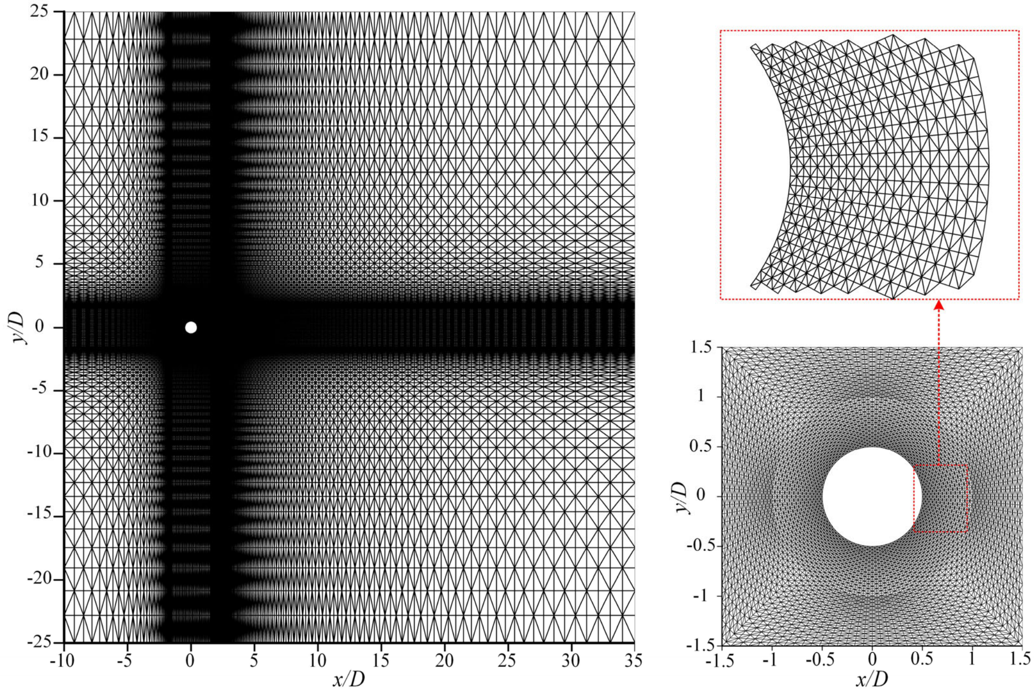

Figure 2. Finite-element mesh structure of the entire computational domain and grid distribution around the circular cylinder with zoom-in view of the boundary-layer elements.

A mesh independence check was carried out to determine a reasonable mesh resolution. The influence of mesh resolution on the key results is summarized in Table I. The relative deviations in parentheses represent the difference between the present result and that obtained with M3, where C_D^{mean}, C_L^{RMS}, St and Nu^{mean} are the time-mean drag coefficient, the root-mean-squared lift coefficient, Strouhal number and the mean Nusselt number, respectively. It is evident that the errors of hydrodynamic and thermal coefficients are within 1 % for M2. Thus, M2 is adopted in the subsequent calculation. After that, the results of time step convergence analysis together with the maximum Courant–Friedrichs–Lewy (CFL) number in the entire computational domain are listed in Table II. It shows that the normalized time step of dt = 0.01 (dt = $\Delta t U_\infty/D$, Δt is the time step) is reasonable, where the errors are within 1% compared with the referential values at dt = 0.005. Hence, the normalized time step dt = 0.01 is employed for the simulations.

Table I. Mesh independence check for flow past a circular cylinder in mixed convective flow at Re = 100, Pr = 0.71 and Ri = 1.0 with normalized time step of dt = 0.01.

Mesh	Elements	C_D^{mean}	C_L^{RMS}	St	Nu^{mean}
M1	36738	1.302 (0.68%)	0.257 (1.53%)	0.175 (0.00%)	5.119 (1.93%)

M2	58812	1.310 (0.07%)	0.261 (0.00%)	0.175 (0.00%)	5.212 (0.15%)
M3	80246	1.311	0.261	0.175	5.220

Table II. Time step convergence analysis for flow past a circular cylinder in mixed convective flow at Re = 100, Pr = 0.71 and Ri = 1.0 with M2 mesh.

Time step	C_D^{mean}	C_L^{RMS}	St	Nu^{mean}	Max CFL
dt = 0.020	1.289 (1.60%)	0.257 (1.91%)	0.175 (0.00%)	5.126 (1.80%)	1.21
dt = 0.010	1.310 (0.00%)	0.261 (0.38%)	0.175 (0.00%)	5.212 (0.15%)	0.61
dt = 0.005	1.310	0.262	0.175	5.220	0.30

C. Code Validation

The derived numerical formulation is validated for the flow around a heated isolated circular cylinder at Pr = 1 and 10, as illustrated in Fig. 3(a). Detailed code validation is done for an isolated cylinder in the literature.[32] It can be seen that the obtained mean Nusselt numbers from the derived formulation for heat convection flow match well with the literature.[13,46,47] Furthermore, it is also validated with the experimental and simulation results[7,48-50], as shown in Fig. 3(b), the Strouhal number (St) consisting with literature well for the flow around a heated isolated circular cylinder in forced convection with the Re at ranging of 60–160 in this study.

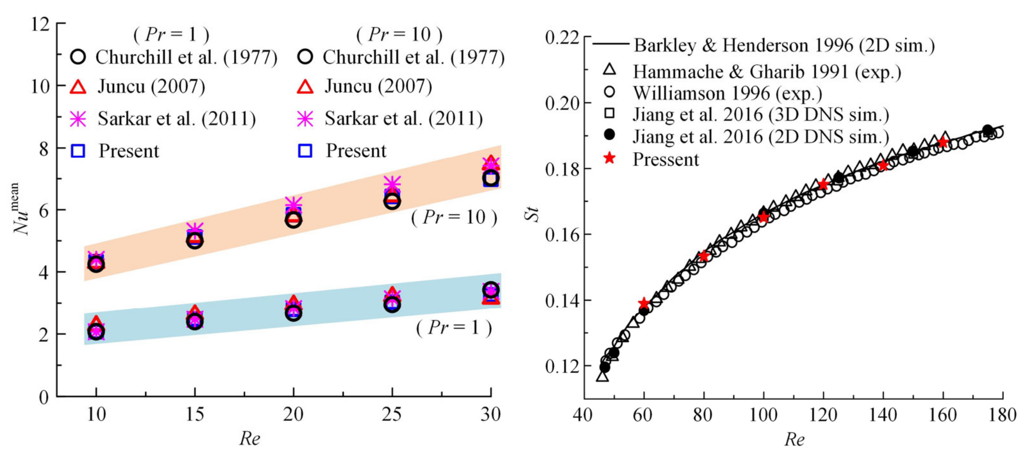

(a) (b)

Figure 3. Validation of the implemented numerical algorithm for flow past a circular cylinder in forced convection flow at: (a) Pr = 1 and Pr = 10; (b) Re = 60–160.

III. RESULTS AND DISCUSSION

A. Characteristics of heat convection

To explore the details of heat convection mechanism, the local Nusselt number $Nu_{(\theta)}$ along the cylinder's surface is recorded in Fig. 4 and Fig. 5. Figure 4 shows that the time-averaged distribution of the $Nu_{(\theta)}$ number is symmetric about the streamwise centerline behind the cylinder in forced convection (Ri = 0), which agrees well with the observations in literature.[12] The maximum value of the $Nu_{(\theta)}^{mean}$ is found around the front stagnation point (θ = 180°). However the minimum value of the $Nu_{(\theta)}^{mean}$ is not at the rear stagnation point (θ = 0°), but at θ = 50° approximately.[38] Figure 4(a) also shows that the heat convection can be significantly enhanced by increasing the value of Pr number, especially for the cases of low Pr numbers within the range of 0.7–10.[13] As shown in Fig. 4(b), the maximum $Nu_{(\theta)}^{mean}$ on the front stagnation point at Pr = 0.71 is 3.92 % higher than that at Pr = 0.7 reported by Sarkar et al.[13] Furthermore, Fig. 4(b) also shows that the distribution of the $Nu_{(\theta)}^{mean}$ along the cylinder's surface increases proportionally with the Re number, especially for the locations around the front and back stagnation points.

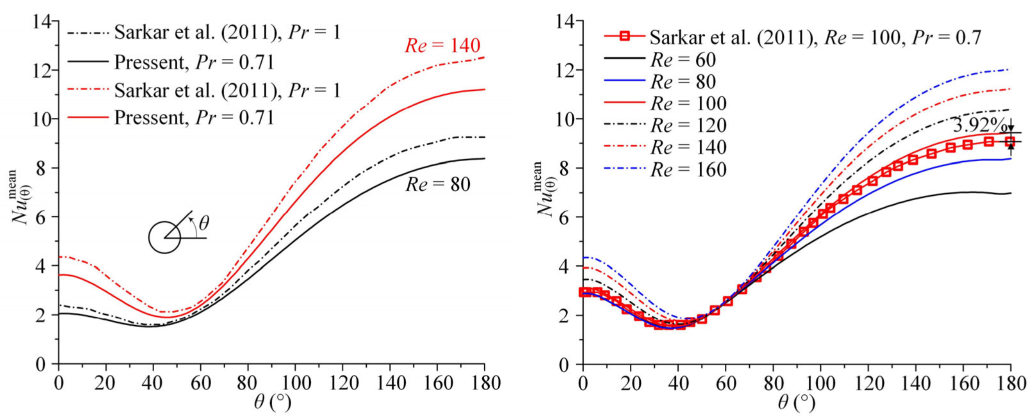

(a) (b)

Figure 4. The distribution of the time-averaged Nusselt number $Nu_{(\theta)}^{mean}$ around the cylinder in forced convection (Ri = 0): (a) comparison with reported results; (b) comparison at different Re.

Figure 5 shows the time histories of the $Nu_{(\theta)}$ distribution along the cylinder's surface measured counterclockwise from the back of the cylinder (θ = 0°). It can be seen that the fluctuation of heat convection on both sides of the cylinder is asymmetric in mixed convection. However this asymmetry can be significantly suppressed by increasing the Re number alone. Meanwhile, it is also noticed that the thermal boundary layer at the front stagnation point is very thin and results in a strong temperature gradient around these local region.

The periodic and alternatively shed vortices causes the continuous exchange of fluid momentum and thermal energy in wake and induces the fluctuation of the local $Nu_{(\theta)}$ along the

Accepted to Phys. Fluids 10.1063/5.0119962

cylinder's surface. Consequently, the most of the variation of $Nu_{(\theta)}$ usually occurs around the back stagnation point of the cylinder (θ = 0° and 360°), as shown in Fig. 5. It is also found that the shedding process starts with the generation of an upper vortex blob identified by the stretching of the vorticity strand at the upper cylinder shoulder, e.g., the case of Re = 60 and Ri = 2.0. This observation agrees well with the findings of Biswas and Sarkar.[38] Consequently, the value of local $Nu_{(\theta)}$ fluctuates periodically around θ = 0° and 360° in Fig. 5.

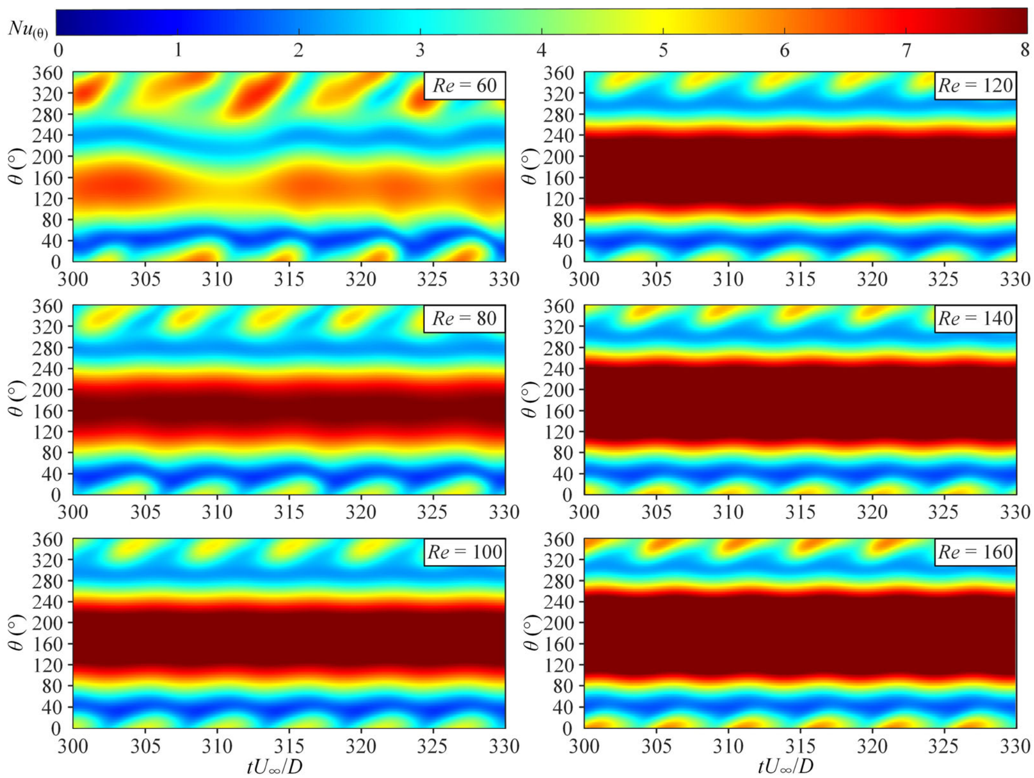

Figure 5. The spatial-temporal evolution of $Nu_{(\theta)}$ around the cylinder's surface in mixed convection (Ri = 2) for Re number ranging from 60 to 160.

The time-averaged and root-mean-square (RMS) values of the Nu number along the cylinder's surface are plotted in Fig. 6. It shows that the value of Nu^{mean} increases slowly with the increase of Ri number. Comparing with the Re number, the changes of Ri number (cross buoyancy) have very little influence on the efficiency of heat transfer across the cylinder's surface. On the other hand it is also found that the value of Nu^{mean} arises significantly with the increase of Re number (stronger fluid momentum) for a particular Ri number. Moreover, as illustrated in Fig. 6(b), the value of Nu^{RMS} is found increasing linearly with the Ri number for Re = 80–160. However, in the case of Re = 60, the value of Nu^{RMS} increases exponentially with the *Ri* number instead.

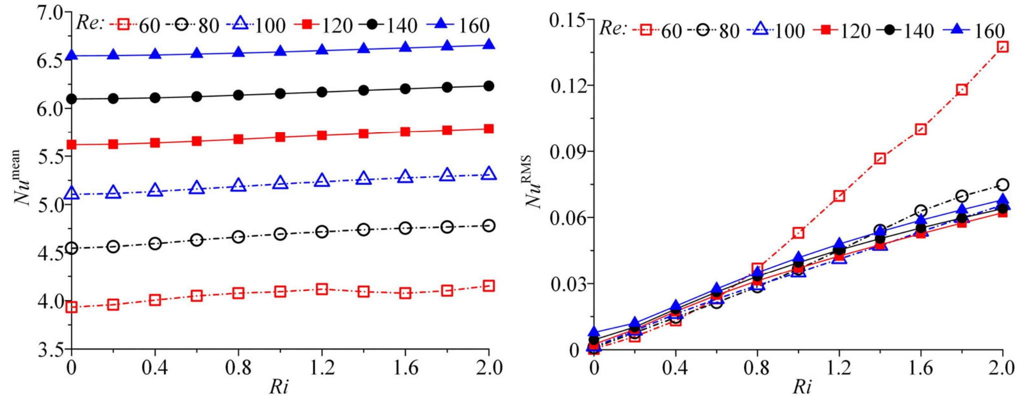

(a) (b)

Figure 6. Variation of Nusselt number along the cylinder's surface with respect to *Re* and *Ri* numbers: (a) the variation of the time-averaged Nusselt number Nu^{mean} with respect to *Ri* number; (b) the variation of the root-mean-square Nusselt number Nu^{RMS} with respect to *Ri* number.

The normalized frequency amplitude spectral density (ASD) contours of $Nu_{(\theta)}$ along the cylinder's surface are shown in Fig. 7. It shows that the ASD contours are distributed symmetrically around the cylinder's surface in forced convection (Ri = 0). The frequency of the dominant mode increases gradually with the increase of *Re* number. The second frequency component of $Nu_{(\theta)}$ (around f^* = 0.3667) also appears in the case of Re = 160 and Ri = 0 in Fig. 7. In mixed convection, similar to the results in Fig. 5, the ASD contours of $Nu_{(\theta)}$ become asymmetric, because of the existence of cross buoyancy. It is also noticed that the amplitudes of the frequency components of the $Nu_{(\theta)}$ mode increase progressively as the *Ri* number increases and are generally bounded by 0.5. Furthermore, compared with the frontal area of the cylinder (θ = 180°), the frequency spectrum of $Nu_{(\theta)}$ is much wider around the back area of the cylinder (θ = 0° or 360°). On the other hand, the dominant frequency component around the frontal area of the cylinder is found to be f^* = 0.08 in Fig. 7. In contrast, the dominant frequency component of the $Nu_{(\theta)}$ mode around the back area of the cylinder are about f^* = 0.16 instead. Furthermore, the distribution of frequency modes of local $Nu_{(\theta)}$ is found generally symmetric on both sides of the cylinder. This observation is confirmed in the representative cases of the forced and mixed convection, in which the most of the strong frequency modes are concentrated around the back area of the cylinder where the strong mixing of fluid occurs.

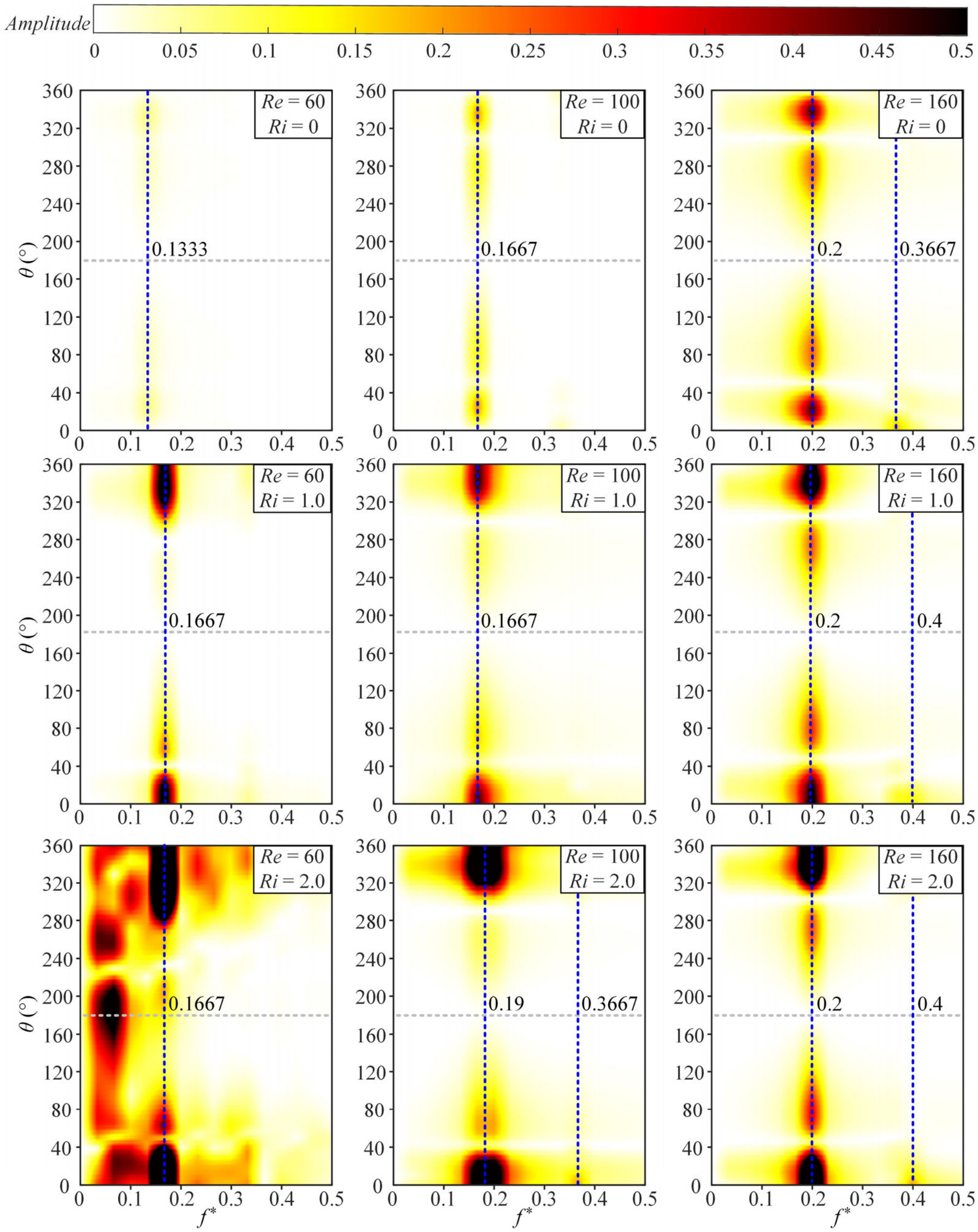

Figure 7. The spatial distribution of the frequency of $Nu_{(\theta)}$ in time domain for different *Ri* and *Re* numbers.

In mixed convection, the heat convection across the cylinder's surface is affected by both *Re* (fluid inertia) and *Ri* (buoyancy) numbers. In frequency domain, Fig. 8 shows the variation of the frequency spectrum of *Nu* with respect to *Re* and *Ri* numbers in mixed convection flow subject to cross buoyancy. The normalized frequency amplitude spectral density (ASD) contours in Fig. 8 suggest that the *Ri* number (thermal cross buoyancy) has limited influence on the frequency of *Nu* number (heat convection across the cylinder), except for the case of *Re* = 60. In the case of *Re* = 60 in Fig. 8, the strong nonlinear features in heat convection dynamics are observed and manifest as multiple frequency modes of *Nu* for Ri > 1.4 approximately. This observation can be confirmed from the time history of the frequency contours of *Nu* number computed using the wavelet scalogram in Fig. 9. In the wavelet scalogram, when the resolution of frequency is important, the Gabor wavelet can be used to plot the real part of the wavelet analysis and trace the minima and maxima of a signal.[51,52] Comparing the cases of *Re* = 60 and *Re* = 160 in Fig. 9, it can be seen that the frequency contours for *Re* = 160 are very regular in time for different *Ri* numbers. In contrast, the frequency contours for *Re* = 60 become unsteady in time for *Ri* = 2.0, which agrees with the observation in Fig. 7 and Fig. 8 for the case of *Re*=60. Figure 9 also shows that the real-valued wavelet isolates the local minima and maxima of the frequency contours of *Nu*. In addition, it is also noticed that the dominant frequency of *Nu* in forced convection is about twice of that in the mixed convection. Compared with the analysis in literature,[38] when the generation of an upper vortex blob is identified by the stretching of the vorticity strand at the upper cylinder shoulder (*Ri* ≥ 1 for *Re* = 60 in this study), the overall response of heat convection becomes oscillatory in time domain and possesses multiple modes in frequency domain.

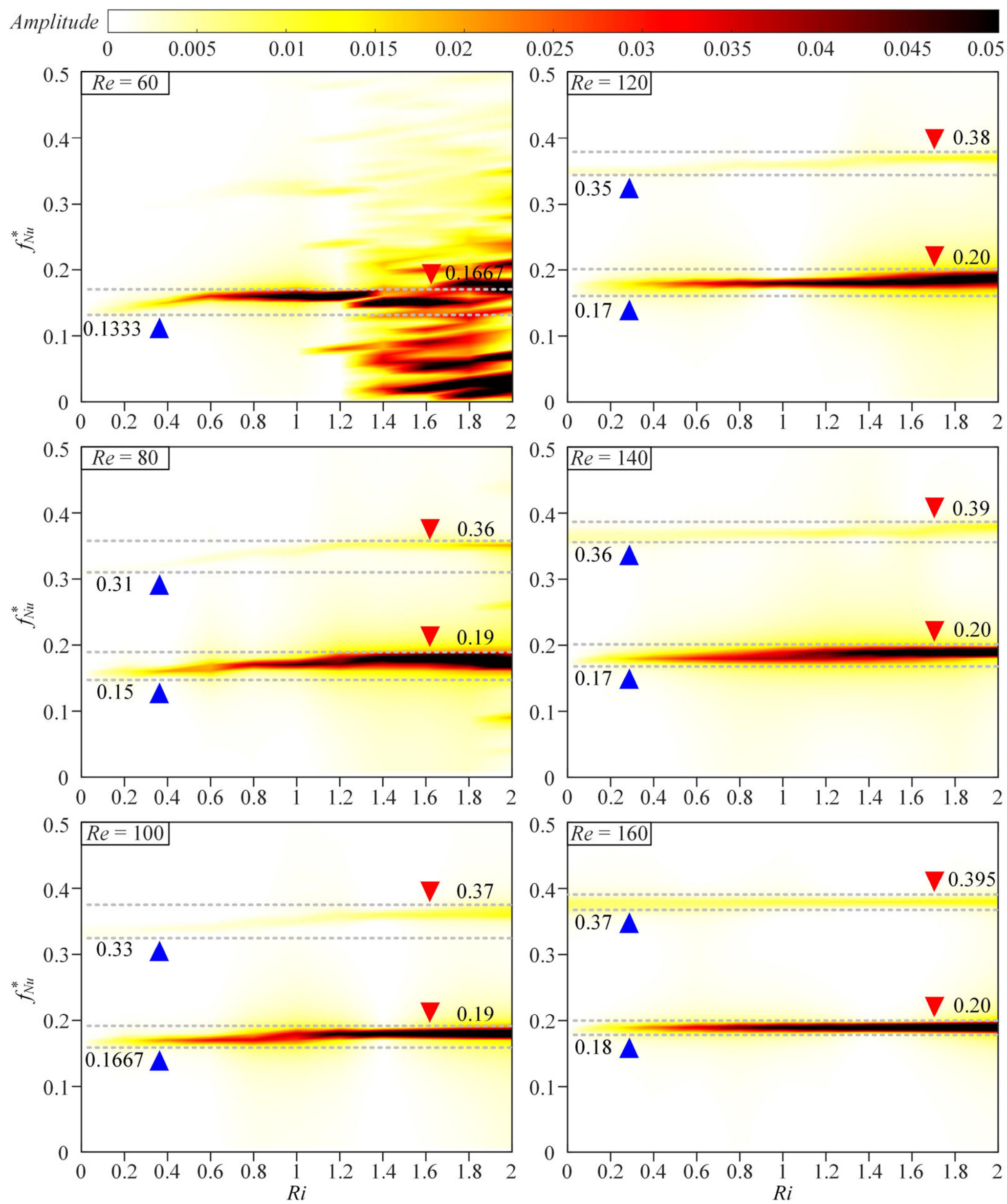

Figure 8. Variation of the frequency of Nusselt number with respect to different *Ri* and *Re* numbers, where the blue and red triangles highlight the upper and lower limit values, respectively.

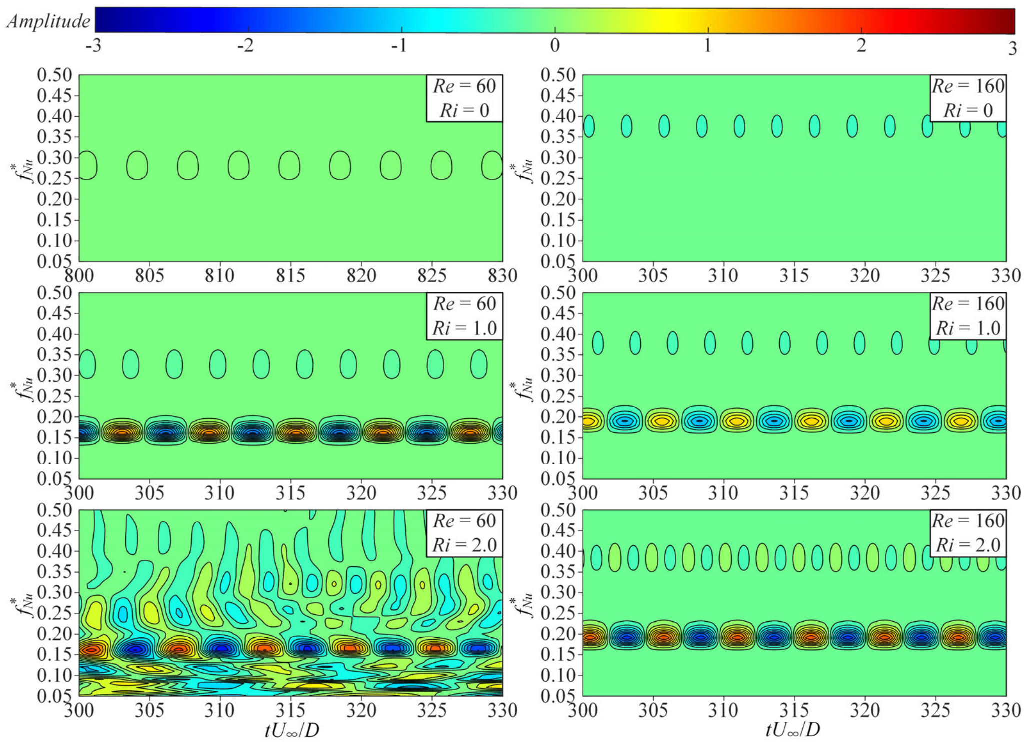

Figure 9. Time history of the frequency contours of Nusselt number for different *Re* and *Ri* numbers.

B. Hydrodynamic response subject to cross buoyancy

The vortex dynamics in mixed convection is rich of physics, since the hydrodynamics and buoyancy effect are strongly coupled in the wake. Figure 10 shows the variations of hydrodynamic coefficients of the heated cylinder with respect to the *Ri* number. In this study, a number statistical quantities are defined to quantify the complexity of dynamics in mixed convection. For instance, the time-averaged hydrodynamic coefficients ($C_{\mathrm{D}}^{\mathrm{mean}}$ and $C_{\mathrm{L}}^{\mathrm{mean}}$) and the root-mean-squared hydrodynamic coefficients ($C_{\mathrm{D}}^{\mathrm{RMS}}$ and $C_{\mathrm{L}}^{\mathrm{RMS}}$) are defined as:

$$C_{\mathrm{D}}^{\mathrm{mean}} = \frac{1}{N}\sum_{i=1}^{N}\frac{h_x^{*cyl}}{0.5\rho_0 U_\infty^2 D}\ ;\quad C_{\mathrm{L}}^{\mathrm{mean}} = \frac{1}{N}\sum_{i=1}^{N}\frac{h_y^{*cyl}}{0.5\rho_0 U_\infty^2 D} \tag{4a}$$

$$C_{\mathrm{D}}^{\mathrm{RMS}} = \sqrt{\frac{1}{N}\sum_{i=1}^{N}\left[\frac{h_x^{*cyl}}{0.5\rho_0 U_\infty^2 D}\right]^2}\ ;\quad C_{\mathrm{L}}^{\mathrm{RMS}} = \sqrt{\frac{1}{N}\sum_{i=1}^{N}\left[\frac{h_y^{*cyl}}{0.5\rho_0 U_\infty^2 D}\right]^2} \tag{4b}$$

where N is the number of sample data in the time series. The h_x^{*cyl} and h_y^{*cyl} are the dimensionless traction force exerted on the cylinder in the x and y directions, respectively.

Figure 10(a) and Figure 10(b) show that the values of $C_{\mathrm{D}}^{\mathrm{mean}}$ and $C_{\mathrm{L}}^{\mathrm{mean}}$ decrease progressively as the Ri number increases for Re =80–160. In contrast the values of both C_D^{RMS} and C_L^{RMS} increase gradually for Re =80–160 instead. However, different from the value of C_D^{mean} in Fig. 10(a), the values of C_L^{RMS} in Fig. 10(b) are very different for different Re numbers. In the cases of Re = 60, the value of C_D^{mean} decreases for Ri = 0–1 and increases for Ri = 1–2. On the other hand, in the case of Re = 60, the value of C_L^{mean} increases for Ri = 1–1.6 and decreases for Ri = 1.6–2. Overall, the values of both C_D^{RMS} and C_L^{RMS} increase significantly for Ri = 1–2. Among the three values of Ri number, the maximum value of C_L^{RMS} is found in the case of Ri = 2 and Re = 60 in Fig. 10(d).

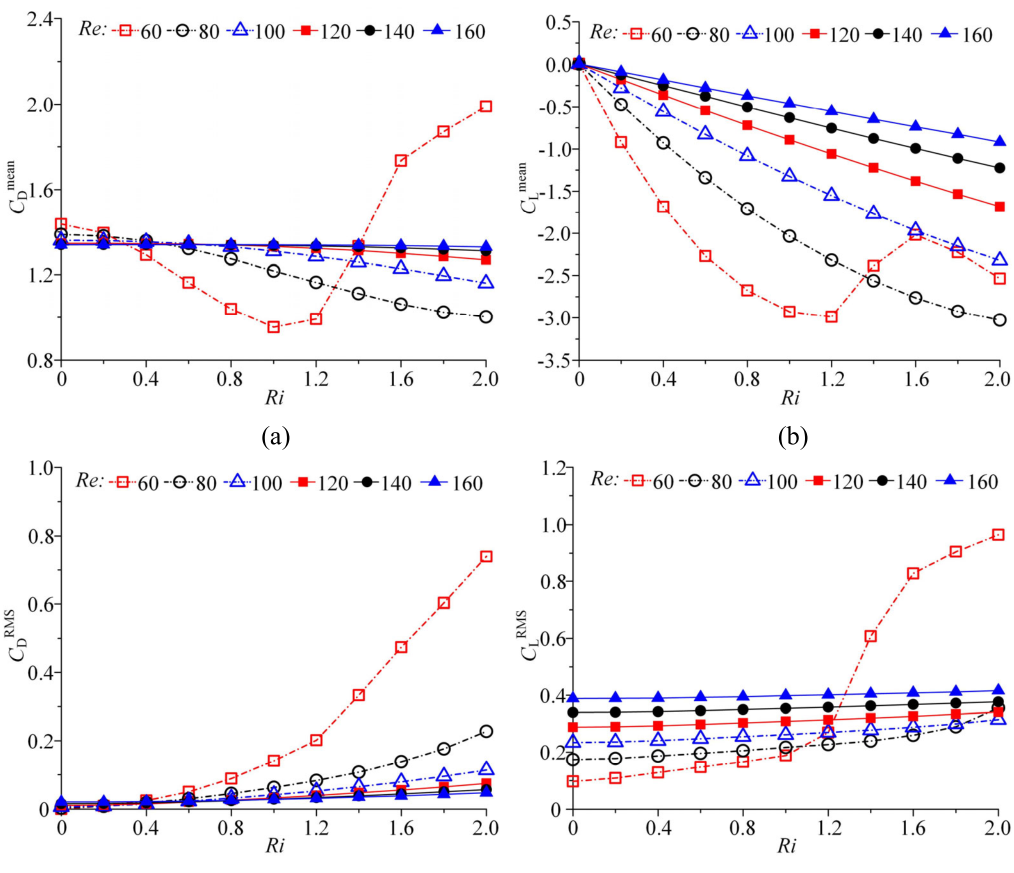

Figure 10. Variation of hydrodynamic coefficients with respect to Ri number: (a) the time-averaged drag coefficient C_D^{mean}; (b) the time-averaged lift coefficient C_L^{mean}; (c) the root-mean-square drag coefficient C_D^{RMS}; (d) the root-mean-square lift coefficient C_L^{RMS}.

Similarly, the amplitude spectral density (ASD) contours of the hydrodynamic coefficients (C_D and C_L) are plotted in Fig. 11 and Fig. 12. Figure 11 shows that the ASD contours of C_D increases with the Ri number for the cases of a fixed Re number. On the other hand, in the canonical case of flow over a cylinder, the periodic vortex shedding results in a periodic change of hydrodynamic forces. It is known that the plot of C_D vs. C_L is a typical figure "8" graph and satisfies the relationship that the dominant frequency of the C_D is twice of the C_L. However, in the case of mixed convection, due to the existence of cross buoyancy, the dynamics of C_D consists of multiple harmonics of the fundamental frequency. By comparing Fig. 11 and Fig. 12, it is noticed that the fundamental frequency of the C_D is synchronized with the C_L. The second frequency component of the C_D is about twice of its fundamental frequency. Furthermore, comparing the ASD contours of the drag coefficient C_D in Fig. 11 and those of the heat convection Nu in Fig. 8, it is found that the dynamics of C_D and Nu are also synchronized together in time domain.

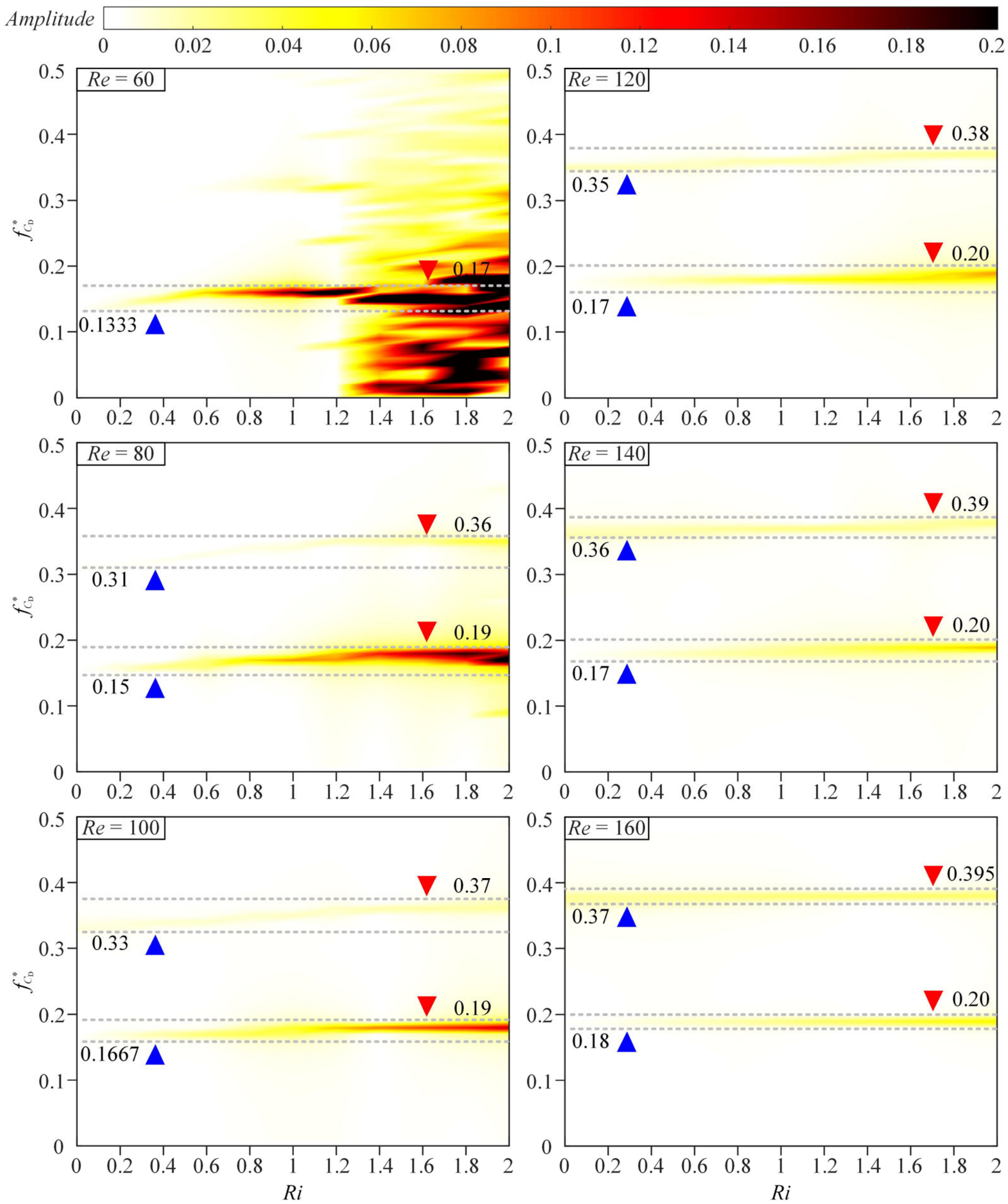

Figure 11. Variation of the frequency of drag coefficient for different *Ri* and *Re* numbers.

It is know that the frequency of vortex shedding is characterized by Strouhal number. Generally, the value of *St* is calculated by taking the Fast Fourier Transform (FFT) of the temporal evolution of the lift force and the highest peak of the harmonics in the FFT portrait represents the corresponding *St* number.[13] Recollecting results in Fig. 3, it can be confirmed that the value of *St* falls in the range of 0.136–0.188 for *Re* = 60–160. Apart from the multiple harmonics of the fundamental frequency of C_D in Fig. 11, the responses of C_L only consist of one dominating frequency for each *Ri* number in Fig. 12. It is believed that this dominating frequency component of the C_L is associated with the vortex shedding process of the heated cylinder.

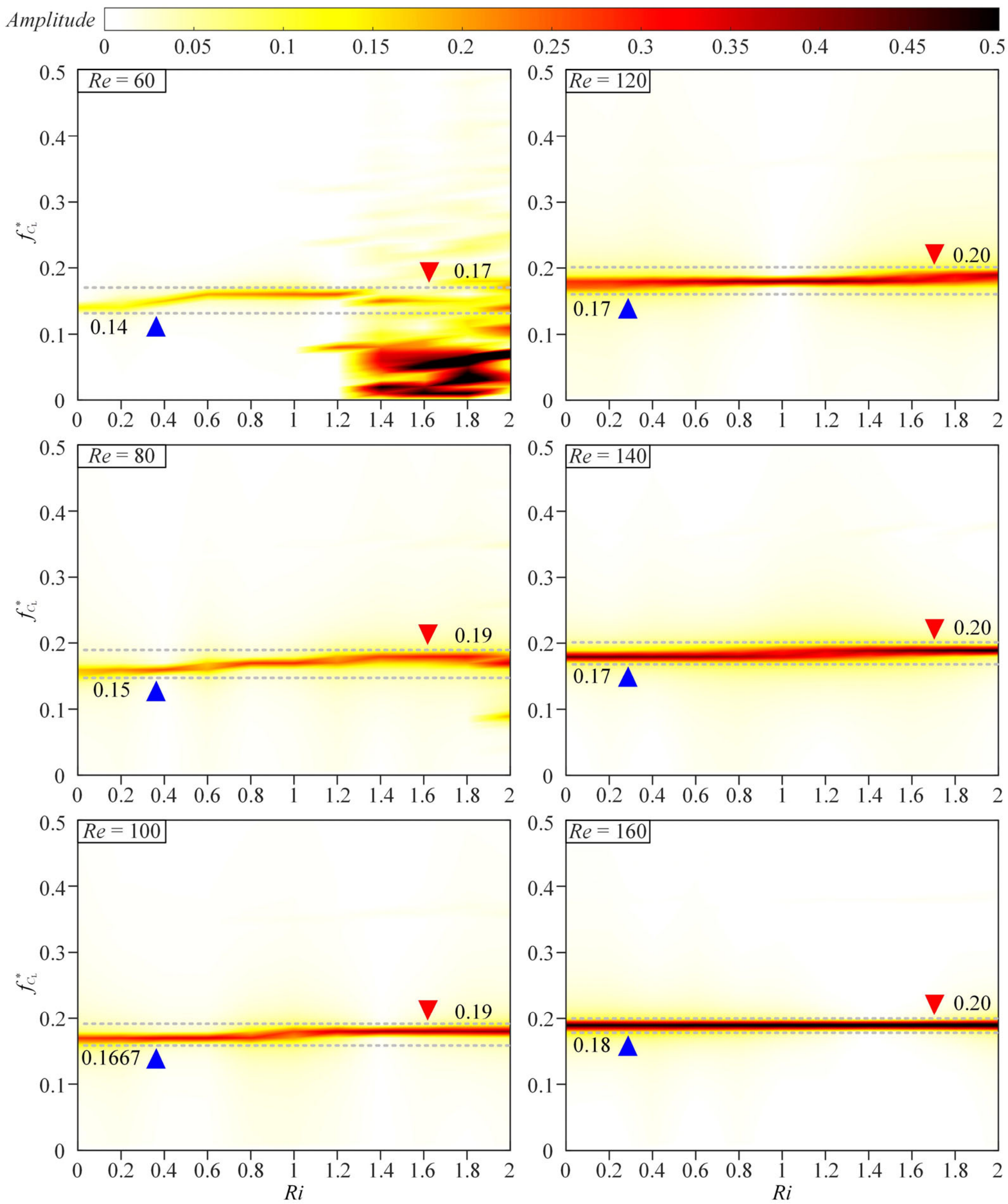

Figure 12. Variation of the frequency of lift coefficient for different *Ri* and *Re* numbers.

To explore the evolution of the local pressure coefficient ($C_{P(\theta)}$) in time domain, the space–time plots of $C_{P(\theta)}$ for Ri = 0–2 and Re = 60–160 are plotted in Figs. 13–15. The similar results were reported recently by Chopra and Mittal in the past.[53] It was found that the dynamics of vortex shedding is a periodic process with alternating values of low and high pressure.[53] In this study, it is also realized that as the vortex shedding frequency St increases, the fluctuation of $C_{P(\theta)}$ in Fig. 13 also increases in the case of forced convection (Ri = 0).

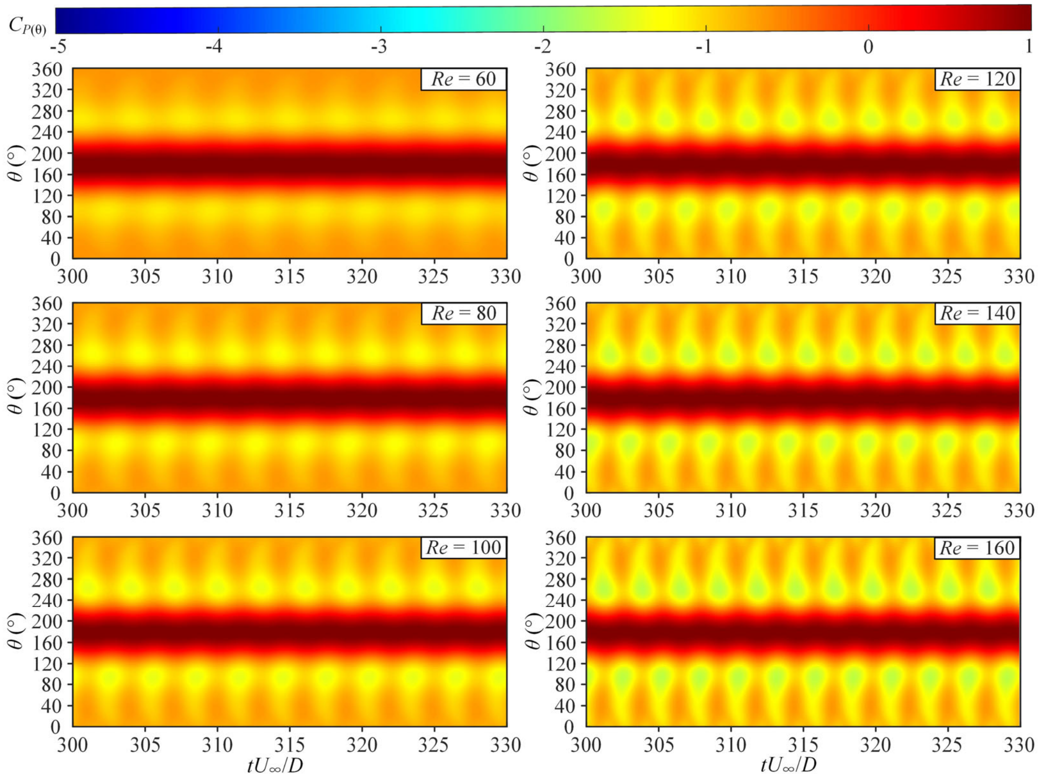

Figure 13. The space-time variation of the pressure coefficient ($C_{P(\theta)}$, t) around the cylinder's surface for *Ri* = 0 (forced convection).

Different from the case of forced convection, the wake behind the cylinder becomes significantly asymmetric due to the existence of cross buoyancy in mixed convection. Consequently, the pressure distributions along the cylinder's surface for *Ri* = 1-2 and *Re* = 60–160 are asymmetric in Figs. 14–15 in this study. It is found that the pressure on the lower side of the cylinder is lower than those on upper side. Hence it results in the negative values of $C_{\mathrm{L}}^{\mathrm{mean}}$. Therefore, as shown in Fig. 10(b), the higher the value of *Ri* number is, the larger the difference of $C_{P(\theta)}$ between the upper and lower sides of cylinder is and the smaller the value of $C_{\mathrm{L}}^{\mathrm{mean}}$ becomes. For the cases of the same *Ri* number, the symmetry of the $C_{P(\theta)}$ distribution on the upper and lower sides of the cylinder is enhanced as the *Re* number increases. Similar to the cases of forced convection in Fig. 13, as *Re* number increases, the oscillation of local $C_{P(\theta)}$ distribution along the cylinder's surface becomes stronger. This implies that the occurrence of vortex shedding and a large value of $C_{\mathrm{L}}^{\mathrm{RMS}}$.

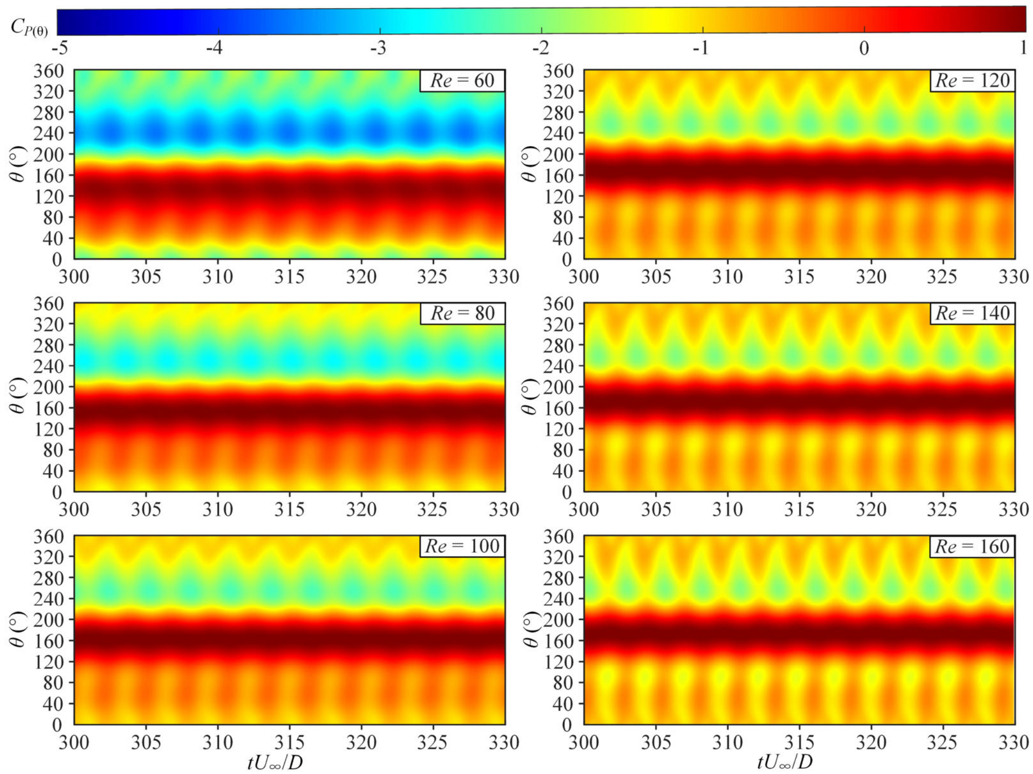

Figure 14. The space-time variation of pressure coefficient ($C_{P(\theta)}$, t) around the cylinder surface for $Ri = 1$.

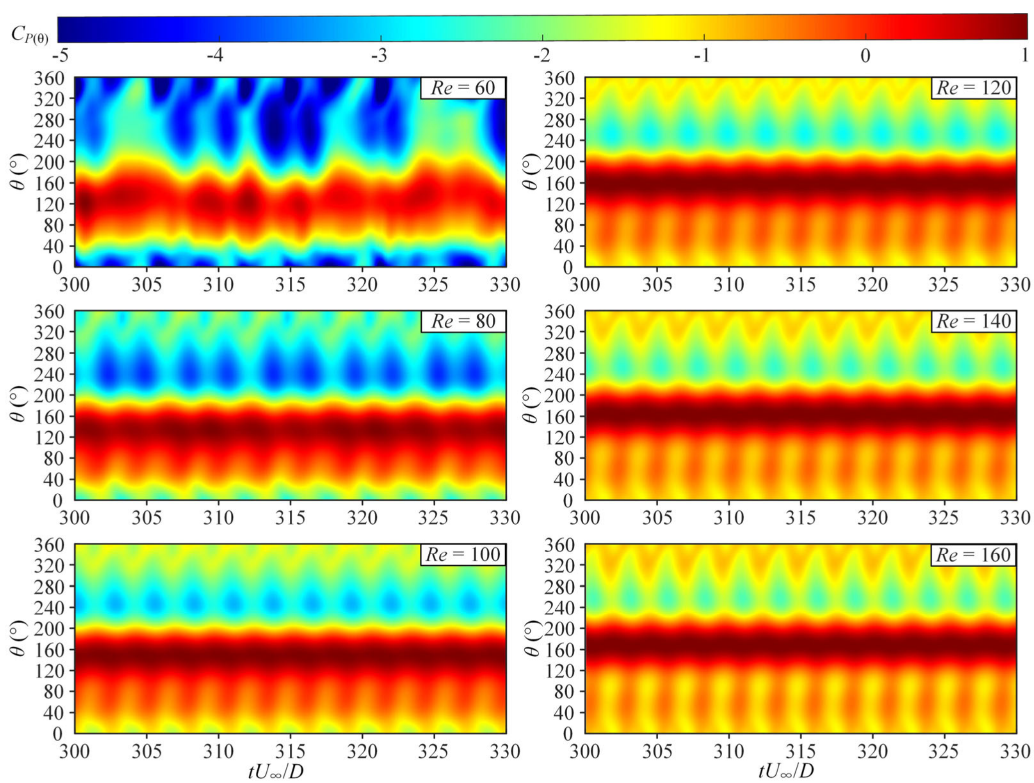

Figure 15. The space-time variation of pressure coefficient ($C_{P(\theta)}$, t) around the cylinder surface for Ri = 2.

Compared with the normalized frequency distribution of $Nu_{(\theta)}$ in Fig. 7, the fundamental frequency of the $C_{P(\theta)}$ in the case of Ri = 2 in Fig. 16 is about twice of $Nu_{(\theta)}$. Similar to the ASD contours of the drag coefficient C_{D} in Fig. 11, it is believed that the second frequency component of the C_{D} is closely associated with the dominant frequency component of $C_{P(\theta)}$, the origin of the form drag. In addition, it is also found that the amplitude of the $C_{P(\theta)}$ is bounded between 0–0.5 uniformly. The dominant frequency will increase progressively with the increase of Re number for the cases of the same Ri number. On the other hand, it is also realized that the amplitude of frequency component of $C_{P(\theta)}$ increases gradually with the increase of Ri number for the cases of the same Re number, and the frequency bandwidth is increasing as well.

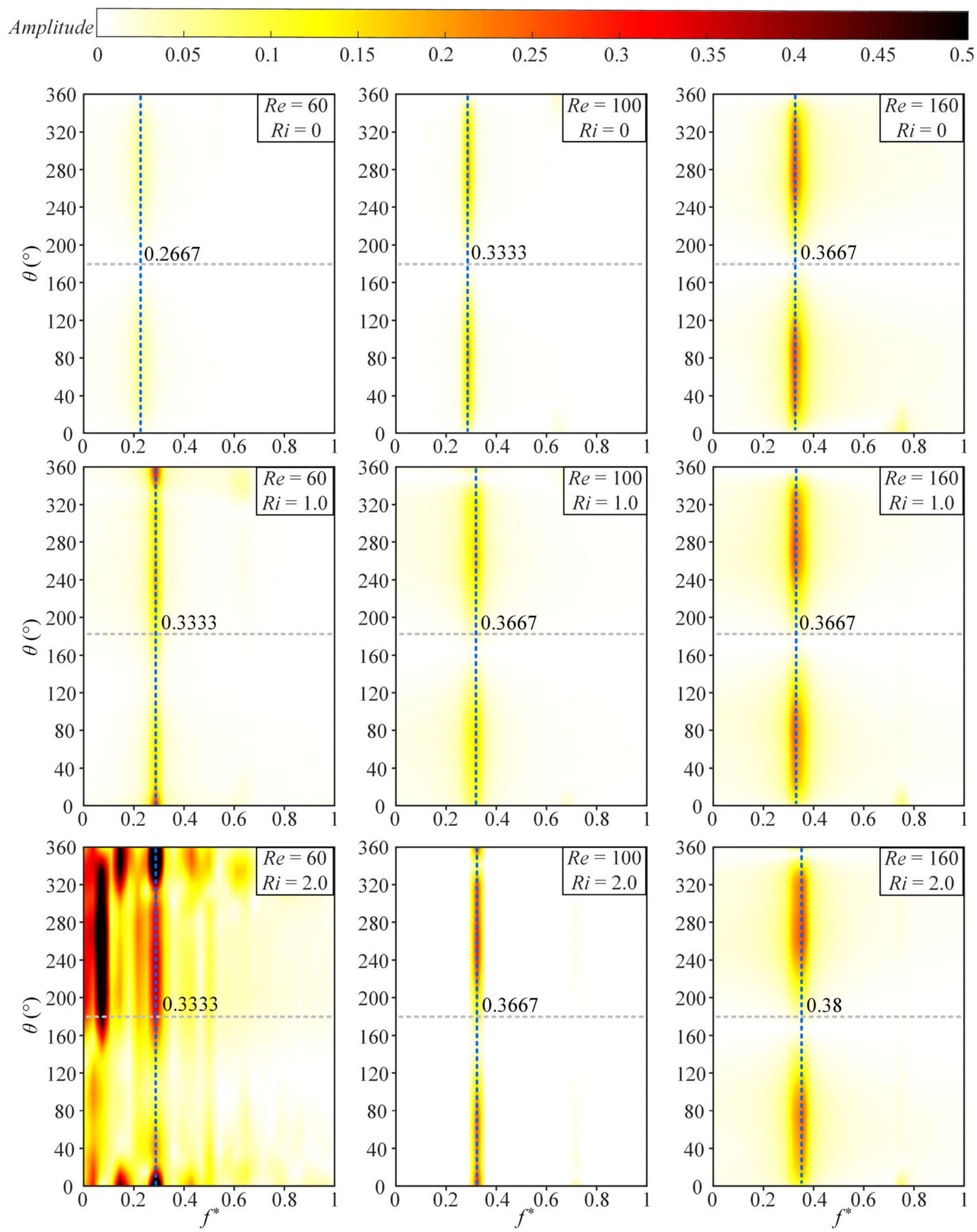

Figure 16. The spatial distribution of the frequency component of $C_{P(\theta)}$ for different *Ri* and *Re* numbers.

C. Characteristics of fluid kinetic energy and thermal energy in wake

In this session, the transportation of fluid kinetic energy and thermal energy in fine scale in forced and mixed convection are studied. The normalized time-averaged velocity field u^*_{mean} and v^*_{mean}, and the time-averaged temperature field T^*_{mean} are defined as:

$$u^*_{\text{mean}} = \frac{1}{N}\sum_{i=1}^{N} u^*_i\ ;\ \ v^*_{\text{mean}} = \frac{1}{N}\sum_{i=1}^{N} v^*_i\ ;\ \ T^*_{\text{mean}} = \frac{1}{N}\sum_{i=1}^{N} T^*_i \tag{5}$$

Where N is the number of sampled data in the time series. u^*_i, v^*_i and T^*_i are the dimensionless streamwise velocity component, transverse velocity component and temperature fields, respectively. In forced convection (Ri = 0), the coherent structures of the vortex dynamics and thermal diffusion in wake are symmetric. Although in mixed convection (Ri > 0), Fig. 17 shows that the cross buoyancy effect has a limited effect on the length of the recirculation region. However, as Ri number increases, the strong asymmetries are observed in the velocity and temperature fields due to the existence of cross buoyancy, e.g. the mean streamwise velocity component, the asymmetric flux of mean transverse velocity component in wake and the heat convection in wake in Fig. 17.

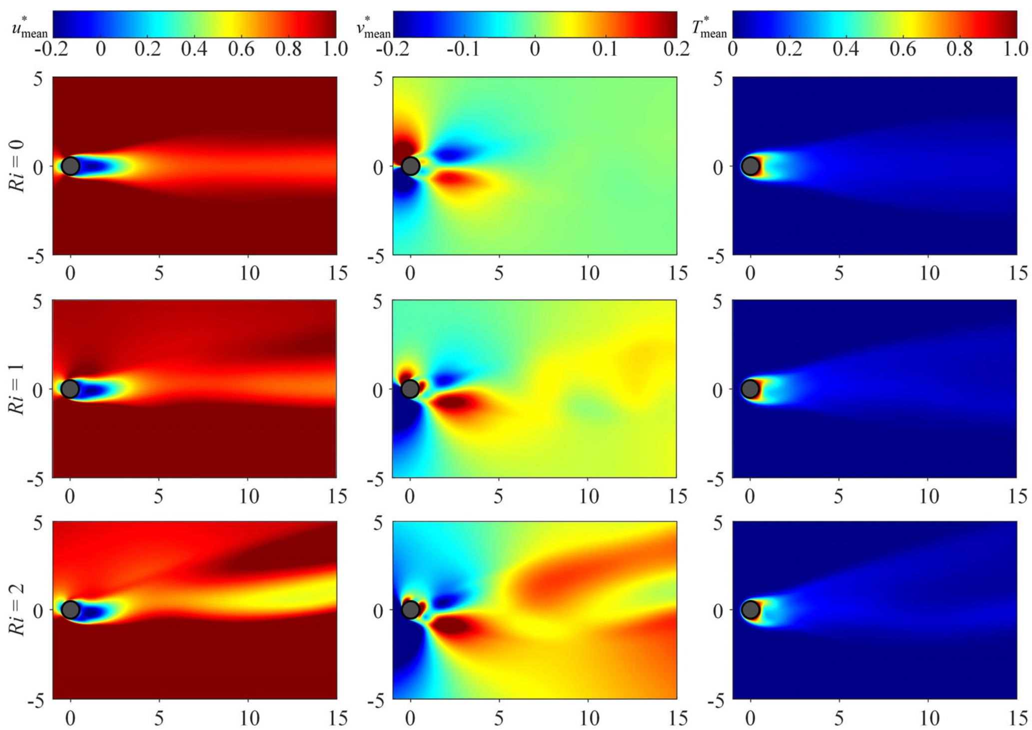

Figure 17. Contours of the normalized time-averaged flow field at Re = 100.

Besides the study of the mean flow, the study of Reynolds stresses provides an analytical approach to quantify the dynamics of the cascades of the fluid kinetic energy and thermal energy in fine scale in wake and the characteristics of the associated fluid stability. Based on the Reynolds decomposition, the Reynolds stresses can be computed as:

$$u^*_i = u^*_{\text{mean}} + u'^*_i\ ;\ \ v^*_i = v^*_{\text{mean}} + v'^*_i\ ;\ \ T^*_i = T^*_{\text{mean}} + T'^*_i \tag{6}$$

Accepted to Phys. Fluids 10.1063/5.0119962

where the ($u_i'^*$, $v_i'^*$, $T_i'^*$) is the fluctuating component. Various Reynolds averaged quantities (Reynolds normal stresses: $\overline{u'^*u'^*}$, $\overline{v'^*v'^*}$ and the shear stresses: $\overline{u'^*v'^*}$ are calculated). Similarly, the streamwise ($\overline{u'^*T'^*}$) and the transverse ($\overline{v'^*T'^*}$) velocity-temperature correlations are also computed, because these quantities are associated with the cascade of thermal energy transported by the fine-scale streamwise and transverse fluid fluctuations in wake. Refer to Zafar and Alam's definition,[54] they are defined as :

$$\overline{u'^*u'^*} = \frac{1}{N}\sum_{i=1}^{N} u_i'^* \cdot u_i'^* \tag{7a}$$

$$\overline{v'^*v'^*} = \frac{1}{N}\sum_{i=1}^{N} v_i'^* \cdot v_i'^* \tag{7b}$$

$$\overline{u'^*v'^*} = \frac{1}{N}\sum_{i=1}^{N} u_i'^* \cdot v_i'^* \tag{7c}$$

$$\overline{u'^*T'^*} = \frac{1}{N}\sum_{i=1}^{N} u_i'^* \cdot T_i'^* \tag{7d}$$

$$\overline{v'^*T'^*} = \frac{1}{N}\sum_{i=1}^{N} v_i'^* \cdot T_i'^* \tag{7e}$$

Figure 18(a) shows the contours of Reynolds normal stress $\overline{u'^*u'^*}$ for the cases of Ri = 0, 1, 2.0 and Re = 60, 100, 160. It is observed that there are two peaks in the contour of $\overline{u'^*u'^*}$ in the wake behind the cylinder. These peaks are associated with the strong vortices formed by the separated boundary layers from the upper and lower sides of the cylinder.[54] In forced convection, the peaks of $\overline{u'^*u'^*}$ are symmetric about the streamwise centerline. As the Ri number keeps increasing, Fig. 18(a) shows that the fluid kinetic energy is further transferred by the fine-scale fluid fluctuation upward in wake because of the cross-buoyancy effect. Furthermore, Fig. 18(b) also shows that the cascade of fluid kinetic energy, a large value of $\overline{u'^*u'^*}_{\max}$, is much more stronger in the case of larger Ri number and smaller Re number. In these cases, the wake is more prone to be 'turbulent', because of the presence of strong thermal cross-buoyancy against a weaker fluid inertia. Especially when $Re < 100$ and $Ri > 1$, the value of the $\overline{u'^*u'^*}_{\max}$ increases proportionally with the Ri number.

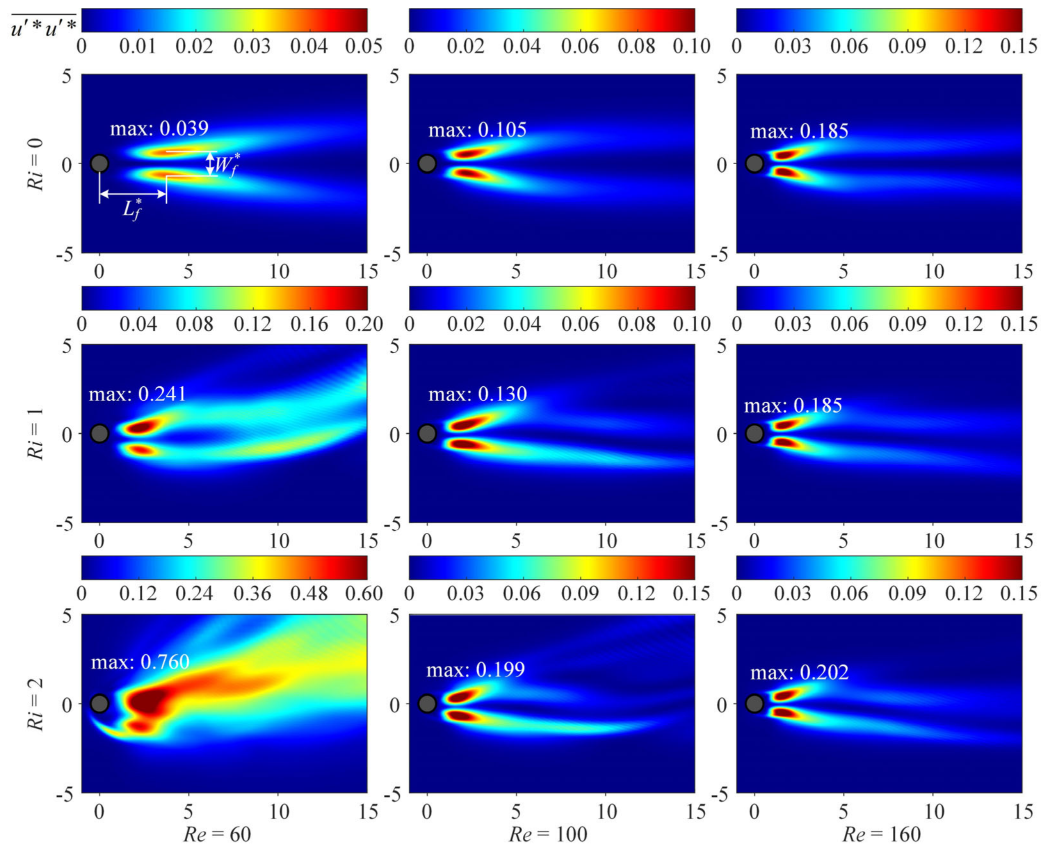

(a)

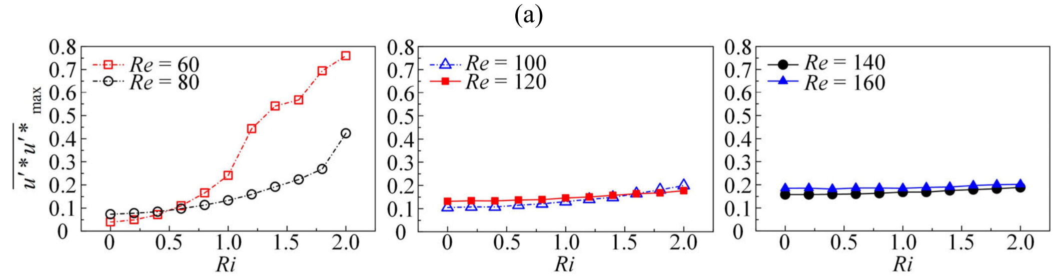

(b)

Figure 18. Reynolds normal stresses: (a) contours of the Reynolds normal stresses $\overline{u'^*u'^*}$ for different *Re* numbers; (b) variation of the maximum Reynolds normal stresses $\overline{u'^*u'^*}_{max}$ with respect to *Ri* number.

The longitudinal distance from the cylinder center to the $\overline{u'^*u'^*}_{max}$ coincides with the vortex formation length L_f^* (= L_f/D) and width W_f^* (= W_f/D), as marked in Fig. 18(a). Zafar and Alam[55] illustrates that the vortex formation length L_f^* may have a great influence on the value of Nu^{mean} along the cylinder's surface since a shorter L_f^* means that the core of the recirculating flow is close to the cylinder and results in a higher value of Nu^{mean}. Based on this discussion, it is believed that the Nu^{RMS} along the cylinder's surface is also effected, as shown previously in Fig. 6. Furthermore, it is shown by the peaks of $\overline{u'^*u'^*}$ in Fig. 18(a) that the distribution of Reynolds normal stresses are symmetric about the streamwise centerline in forced convection. Whereas this symmetry breaks down in mixed convection, because of the presence of strong cross buoyancy. As a result, the vortex formation length L_f^* and width W_f^* on upper and lower side of the cylinder are also asymmetric in mixed convection. A summary of influence of thermal cross buoyancy on the vortex formation length L_f^* and width W_f^* is plotted in Fig. 19, in which the values of L_f^* and width W_f^* on both the upper and the lower sides of the cylinder (the solid line for the upper side, the dotted line for the lower side) are presented. It can be seen that the value of L_f^* keeps reducing as the cross-buoyancy effect becomes stronger and implies a stronger heat convection over the cylinder's surface. On the other hand, the overall width W_f^* does not change remarkably as the *Ri* number increases.

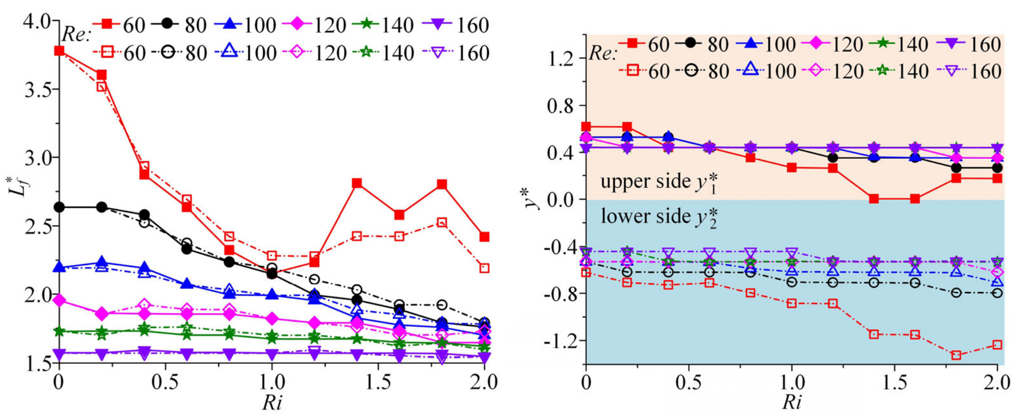

(a) (b)

Figure 19. Variation of (a) normalized vortex formation length L_f^* and (b) wake width $W_f^* (= y_1^* - y_2^*)$ with respect to *Ri* number, where y_1^* (solid line) and y_2^* (dotted line) represent the distance from the upper and lower peak of $\overline{u'^*u'^*}$ to the wake centerline, respectively.

In contrast to the Reynolds normal stress, the contours of Reynolds transverse stress $\overline{v'^*v'^*}$ manifests itself as a single peak in wake. In forced convection (*Ri* = 0), the distribution of $\overline{v'^*v'^*}$ is symmetric and located along the streamwise centerline of cylinder. Whereas the distribution of $\overline{v'^*v'^*}$ becomes asymmetric and deflects upward in mixed convection in Fig. 20(a). The peak value of $\overline{v'^*v'^*}$ shifts to the lower side as the *Ri* number increases.[54] Similarly to the maximum Reynolds normal stress $\overline{u'^*u'^*}_{max}$, the maximum transverse stress $\overline{v'^*v'^*}_{max}$ increases significantly with the increase of *Ri* number for *Re* = 60-80, and grows gradually for *Re* = 100–160 in Fig. 20(b). It is also found that the lateral spread of $\overline{v'^*v'^*}$ becomes narrow for *Ri* = 0 and is enlarged as the *Ri* number further increases.

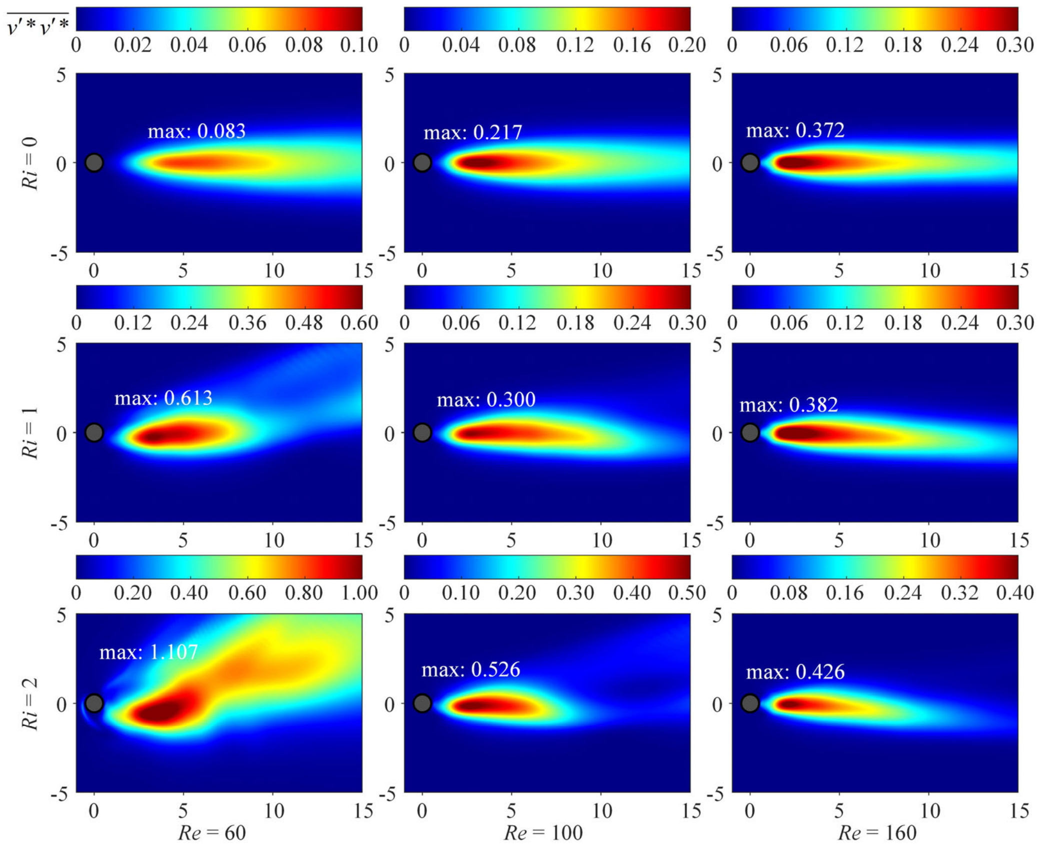

(a)

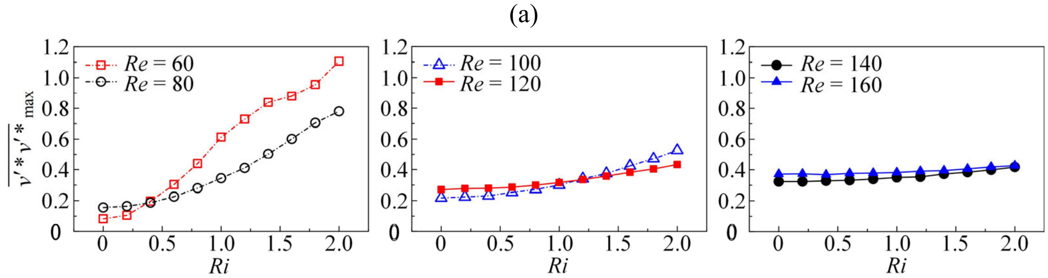

(b)

Figure 20. Reynolds transverse stresses: (a) contours of the Reynolds transverse stresses $\overline{v'^*v'^*}$ for different *Re* numbers; (b) variation of the maximum Reynolds transverse stresses $\overline{v'^*v'^*}_{max}$ with respect to *Ri* number.

Figure 21(a) displays the variation in Reynolds shear stress $\overline{u'^*v'^*}$ with respect to *Ri* and *Re* numbers. The value of $\overline{u'^*v'^*}$ gives a degree of correlation between the streamwise and transverse fluctuating velocity components. It is found that the contours of $\overline{u'^*v'^*}$ is symmetrically distributed along the centerline in wake in force convection (*Ri* = 0), but becomes asymmetric in mixed convection in Fig. 21(a) because of the presence of cross buoyancy. Two peaks of $\overline{u'^*v'^*}$

Accepted to Phys. Fluids 10.1063/5.0119962

contour emerge in the field because of the alternative vortex shedding process. The values of $\overline{u'^*v'^*}_{max}$ increases significantly with the increase of *Ri* number for *Re* = 60 and 80, and grows gradually for *Re* = 100–160 in Fig. 21(b).

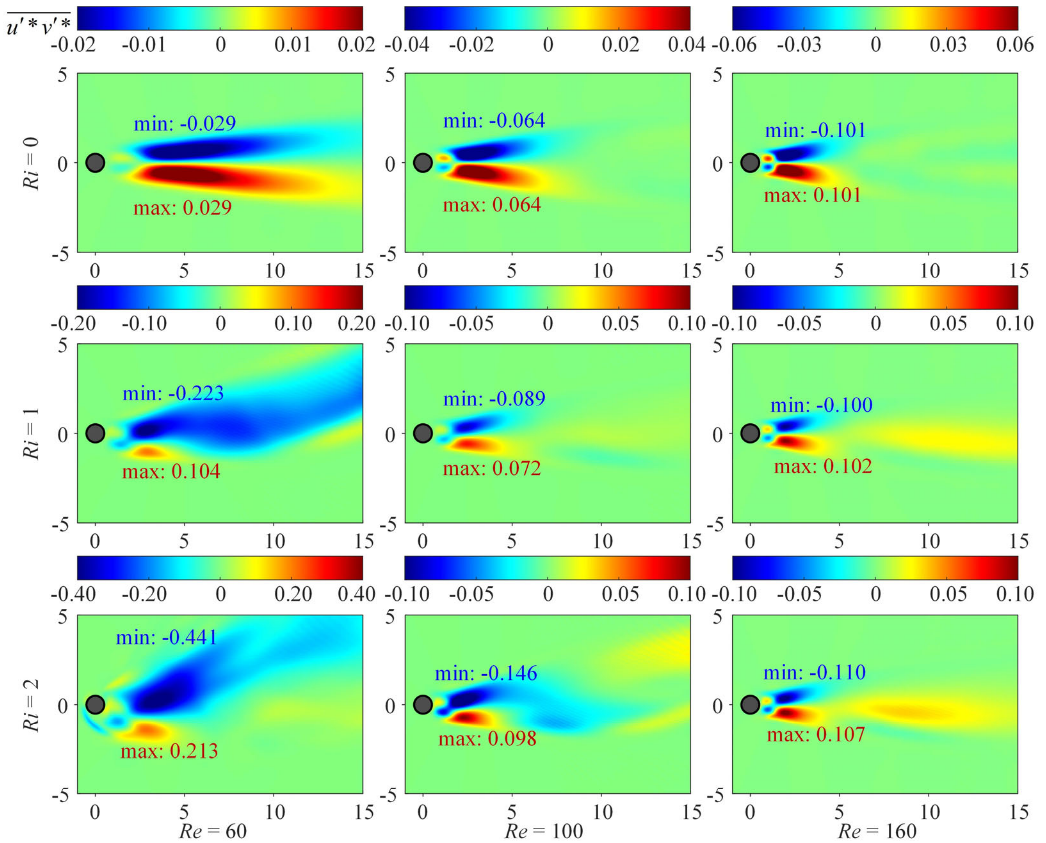

(a)

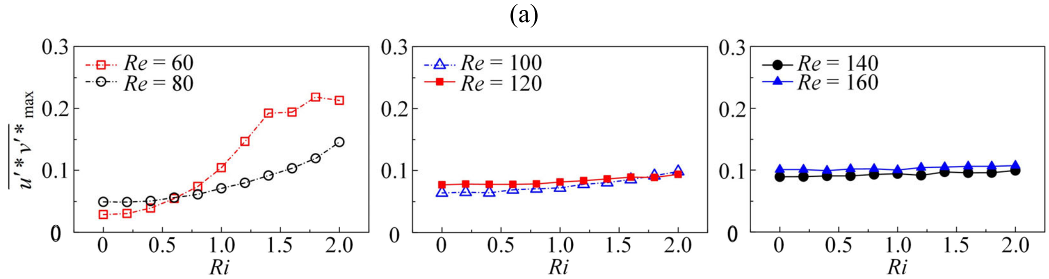

(b)

Figure 21. Reynolds shear stresses $\overline{u'^*v'^*}$: (a) contours of $\overline{u'^*v'^*}$ for different *Re* numbers; (b) variation of the maximum value $\overline{u'^*v'^*}_{max}$ with respect to *Ri* number.

Figure 22(a) shows the distribution of $\overline{u'^*T'^*}$ contours for different *Ri* and *Re* numbers. Similar to the Reynolds normal and transverse stresses, the contours of $\overline{u'^*T'^*}$ are symmetrically distributed in wake in forced convection (*Ri* = 0) and asymmetrically distributed in mixed convection (*Ri* > 0) in Fig. 22(a). For *Ri* = 0, a strong peak (positive) and a small peak (negative) form on each side of the cylinder. The streamwise positions of the positive peak match with that of Reynolds normal stress $\overline{u'^{*}u'^{*}}$ in Fig. 18. It means that the heat convection in wake is primarily driven by the vortex shedding and fluid momentum in forced convection.[55] However, this conclusion does not apply to the cases of low *Re* number and high *Ri* number in this study. In accordance to the study in the literature,[38] it is believed that when the formation of an upper vortex blob originates from the stretching of the vorticity strand at the upper cylinder shoulder ($Ri \geq 1$ for $Re = 60$, in this study), the entire heat convection becomes unsteady and oscillates in time. This results in a dynamics of mixing process involving multiple frequency components, as shown previously in Figs. 7–9. In addition, Fig. 22(b) also shows that the values of $\overline{u'^{*}T'^{*}}_{max}$ increases significantly with the increase of the *Ri* number for $Re = 60$ and 80, and grows gradually for $Re = 100$–160.

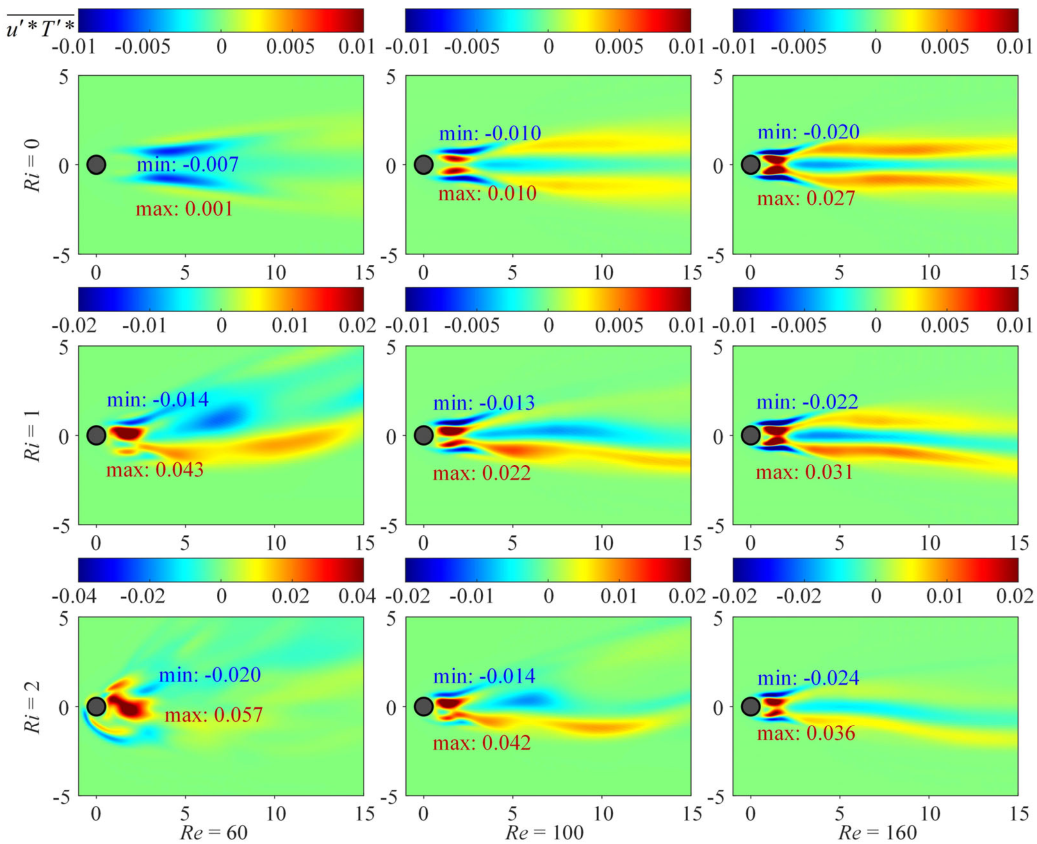

(a)

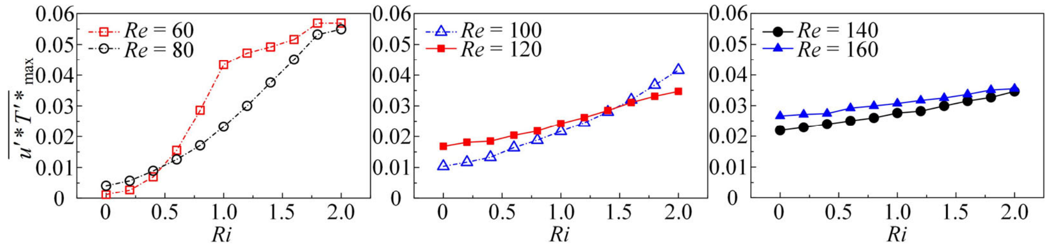

(b)

Figure 22. The time-averaged heat fluxes in the streamwise direction ($\overline{u'^* T'^*}$): (a) contours of $\overline{u'^* T'^*}$ for different *Re* numbers; (b) variation of the maximum value $\overline{u'^*T'^*}_{\max}$ with respect to *Ri* numbers.

In terms of the thermal energy dissipation in the transverse direction, Fig. 23(a) shows that the positive and negative contours of $\overline{v'^* T'^*}$ appear in pairs in wake, a positive peak on the upper side and a negative peak on the lower side of the cylinder. It means that the fluid momentum brings in more cold fluid into the wake towards the centerline behind the cylinder. It can be seen that the contour of $\overline{v'^* T'^*}$ is symmetrically distributed in wake in forced convection (*Ri* = 0) and asymmetrically distributed in mixed convection (*Ri* > 0) as shown in Fig. 22(a). As *Ri* number increases in the cases of *Re* = 60–160, the positive peak of $\overline{v'^* T'^*}$ contour is strengthened and stretched upward due to the thermal cross-buoyancy effect. Whereas the negative contour of $\overline{v'^* T'^*}$ is vanishing instead. It means that there is a stronger heat exchange happening on the upper side of the cylinder. A summary of the dependency of $\overline{v'^*T'^*}_{\max}$ on the *Ri* number is plotted in Figure 23(b). It shows that the value of $\overline{v'^*T'^*}_{\max}$ increases significantly with the *Ri* number for *Re* = 60 -80, and grows gradually for *Re* = 100–160 instead.

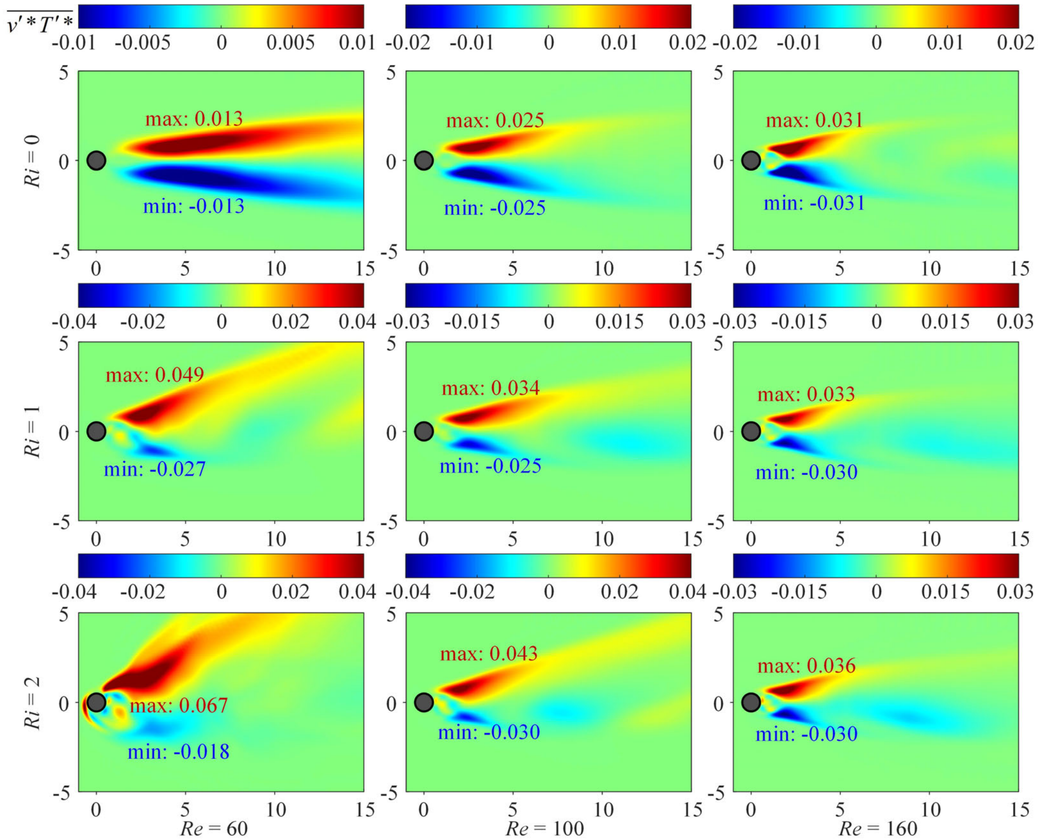

(a)

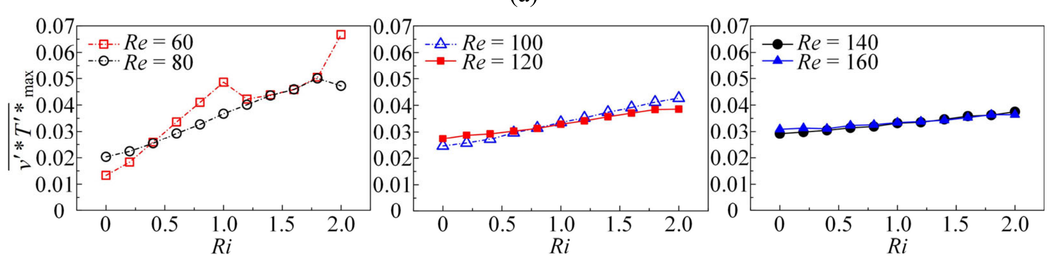

(b)

Figure 23. Time-averaged heat fluxes in the transverse direction ($\overline{v'^*T'^*}$): (a) contours of $\overline{v'^*T'^*}$ for different *Re* numbers; (b) variation of the maximum value $\overline{v'^*T'^*}_{max}$ with respect to *Ri* number.

Figure 24 shows the variation of the boundary layer separation points with *Ri*, where θ_{s1} and θ_{s2} represent the locations of the upper and lower separation points, respectively, measured from the rear stagnation point. On account of the crossflow thermal buoyancy, the two separation points are asymmetrically distributed in mixed convection ($Ri > 0$). For the same *Re*, the values of θ_{s1} at $Ri > 0$ are generally smaller than that at $Ri = 0$. In contrast, the value of θ_{s2} gradually increases with *Ri* at the same *Re*. Consequently, the asymmetrical recirculation region and wake are generated behind

Accepted to Phys. Fluids 10.1063/5.0119962

the cylinder in mixed convection. Particularly, θ_{s2} reaches 180° at Ri = 2.0 when Re = 60, signifying the separation point of the lower boundary layer shifts to the front stagnation point. It implies that the thermal buoyancy at Ri = 2.0 overcomes the inertia force at Re = 60. The same phenomenon was observed by Biswas and Sarkar.[38]

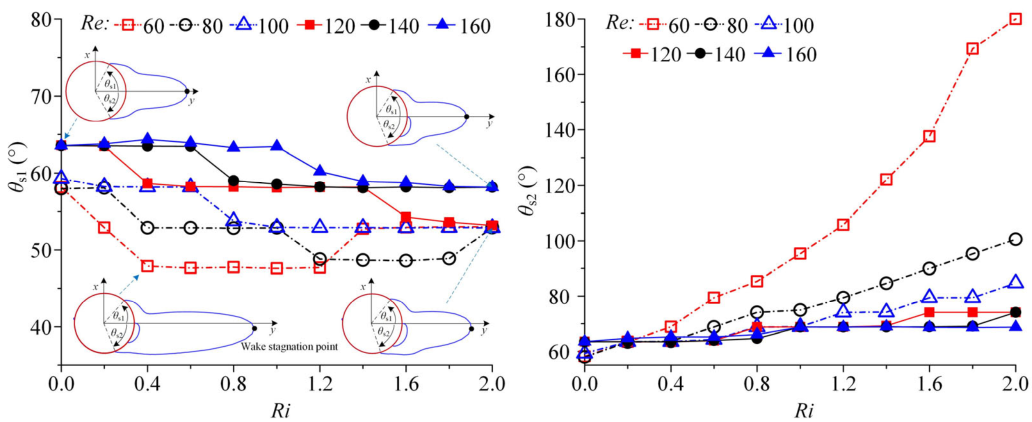

Figure 24. Variation of the boundary layer separation points with Ri.

D. Dynamic mode decomposition

In this section, a modal analysis is conducted based on the dynamic mode decomposition (DMD) technique so as to extract the spatial-temporal modes that play an important role in flow and heat convection processes. Since the application of DMD technique in fluid flow, it has been widely accepted in the fluid community for modal analysis of flow field, especially the isothermal flow over a bluff body.[56] In this study, one of the primary focus is to explore the fundamental mechanism in fluid-thermal-solid interaction by extracting the dominant spatial-temporal modes.

Figure 25(a, b) shows that the step-by-step procedures to apply the DMD algorithm on the spanwise vorticity ω_z in forced convection (Ri = 0) and mixed convection (Ri = 2), respectively. Unlike the proper orthogonal decomposition (POD), the DMD algorithm can not only extract the spatial-temporal modes but also a set of eigenvalues associated with each one of them to approximate their temporal characteristics, e.g., delay or growth. The mean flow mode is not subtracted in the DMD calculation in this study. Therefore, the first mode (shown as mode1 in the DMD process) presents the background mode (mean flow) that does not change in time (i.e., it has zero eigenvalue), as shown in Fig. 25.

For the case of forced convection in Fig. 25(a), it is found that the spatial distribution of the

DMD modes are symmetric and similar to the Bagheri's simulation works[57] and Tu et al.'s experimental results[43]. Figure 25(a) further demonstrates that the first 9 modes account for the 99.00% of cumulative energy. As a result, the vorticity structure reconstructed by these modes is able to precisely approximate the original field data. However, due to the influence of thermal cross buoyancy, it is noticed in Fig. 25(b) that the spatial distribution of DMD modes is asymmetric in wake in mixed convection (Ri = 2). Furthermore it is also noticed that the first 12 DMD modes account for 99.02% of the cumulative energy in the case of mixed convection. The requirement of relatively more DMD modes means that stronger non-linear features exist in wake compared with the case of forced convection. Consequently more linear DMD modes are required to accurately reconstruct the original vorticity field in mixed convection.

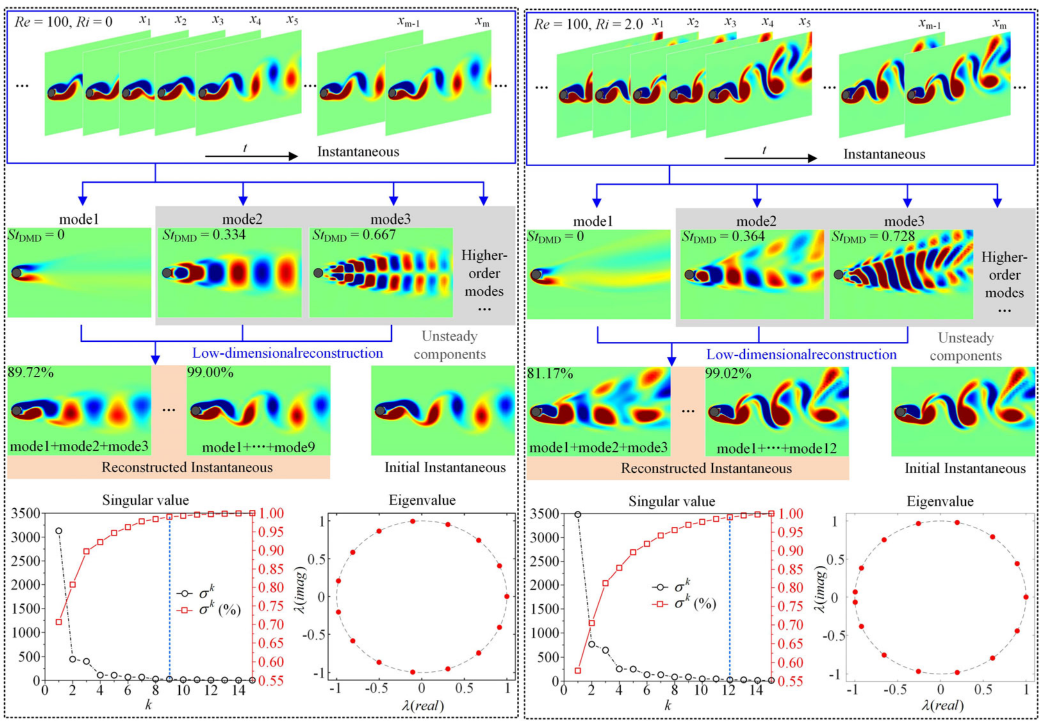

(a) (b)

Figure 25. Schematic diagram of the data processing with DMD algorithm for the spanwise vorticity ω_z for (a) $Ri = 0$ and (b) $Ri = 2$.

The value of k in DMD algorithm is an important parameter. Normally the condition $\sigma^k(\%) \geq$ 99.0% (k < 15) is chosen to determine a suitable value of k to accurately reconstruct the original field data. Based on the aforementioned criteria, the spatial distribution of the DMD modes of the Z vorticity (ω_z) field is presented in Fig. 26. It is observed that when Ri > 1, the cumulative energy $\sigma^k(\%)$ of the first 14 modes cannot reach 99% for Re = 60 because of the existence of strong cross buoyancy. Therefore, it is believed that the much stronger nonlinear features exist in mixed convection and require more linear DMD modes to reconstruct the original field. The modal analysis in the case of Ri = 2 and Re = 80 also agree with this observation. This can also be linked to the aforementioned multiple harmonics characters of C_L^{RMS} in Fig. 10(d) and the ASD contours of C_L in Fig. 12, in which multiple modes are induced by cross-buoyancy effect in frequency domain. In addition, it is also found that the energy of the first DMD mode decreases with the increase of Ri number in the case of the same Re number. On the other hand, the number of DMD modes required to reconstruct the original field data is also found increased as Re number increases in the case of the same Ri number.

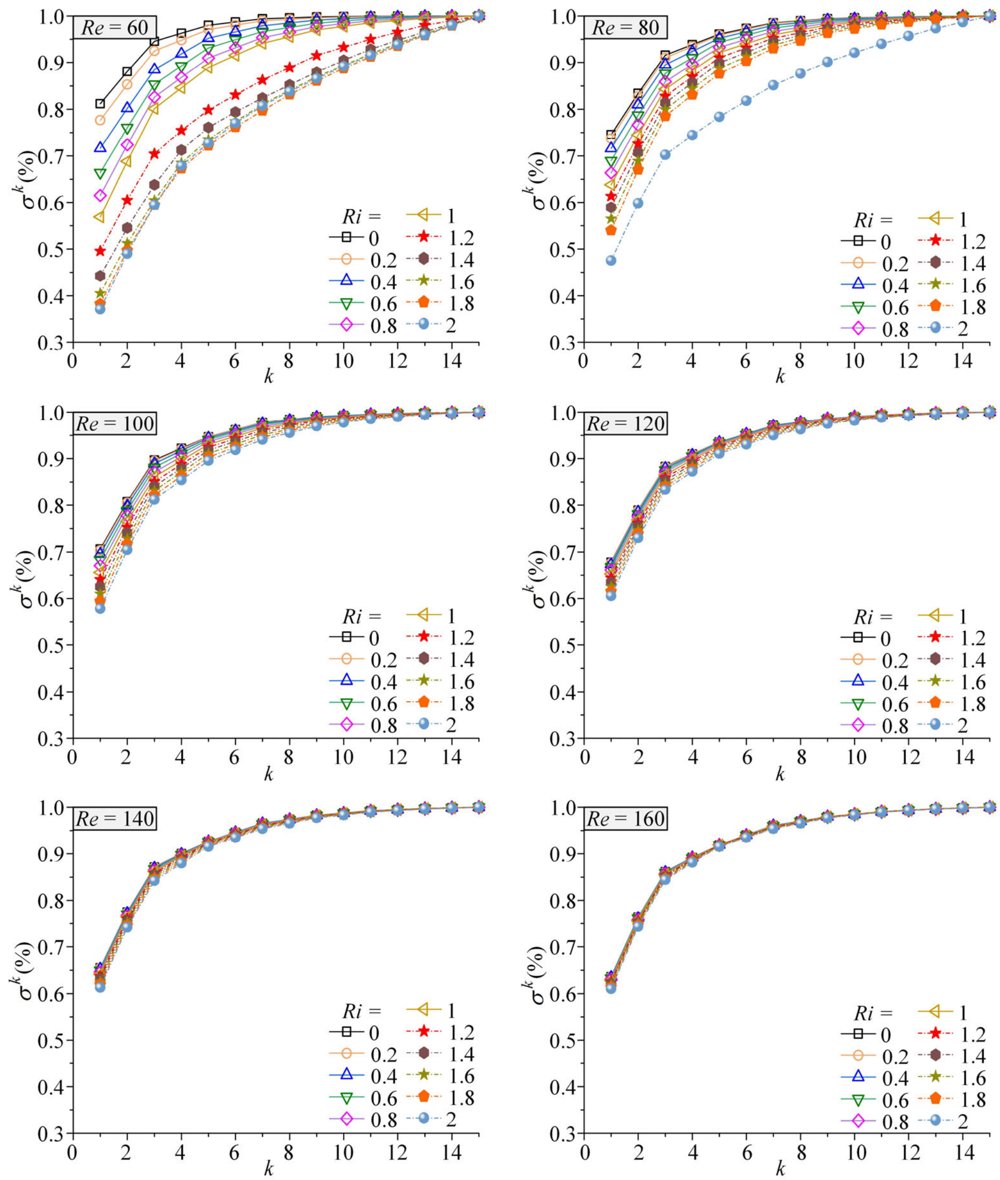

Figure 26. Dependence of σ^k (%) on the value of k for the spanwise vorticity ω_z field.

In terms of the normalized temperature field T^*, Fig. 27(a, b) shows that the modal analysis conducted for the T^* field in forced convection ($Ri = 0$) and mixed convection ($Ri = 2$), respectively. As shown in Fig. 27(a), the first 9 modes account for 99.30% of the cumulative and represents an accurate reconstruction of the temperature field. However, due to the influence of cross-buoyancy effect, for instance the case of $Ri = 2$, the instantaneous temperature field and the associated DMD modes are significantly perturbed and asymmetrically distributed in space. Furthermore, it is also noticed that the first 10 modes of T^* account for 99.00% of the cumulative energy in mixed convection, which is slightly higher than those in forced convection. It suggests that there exist stronger the nonlinear features in the temperature field. Whereas, compared with the spanwise vorticity field in Fig. 25(b), the normalized temperature field requires less DMD modes to reconstruct the original field data instead.

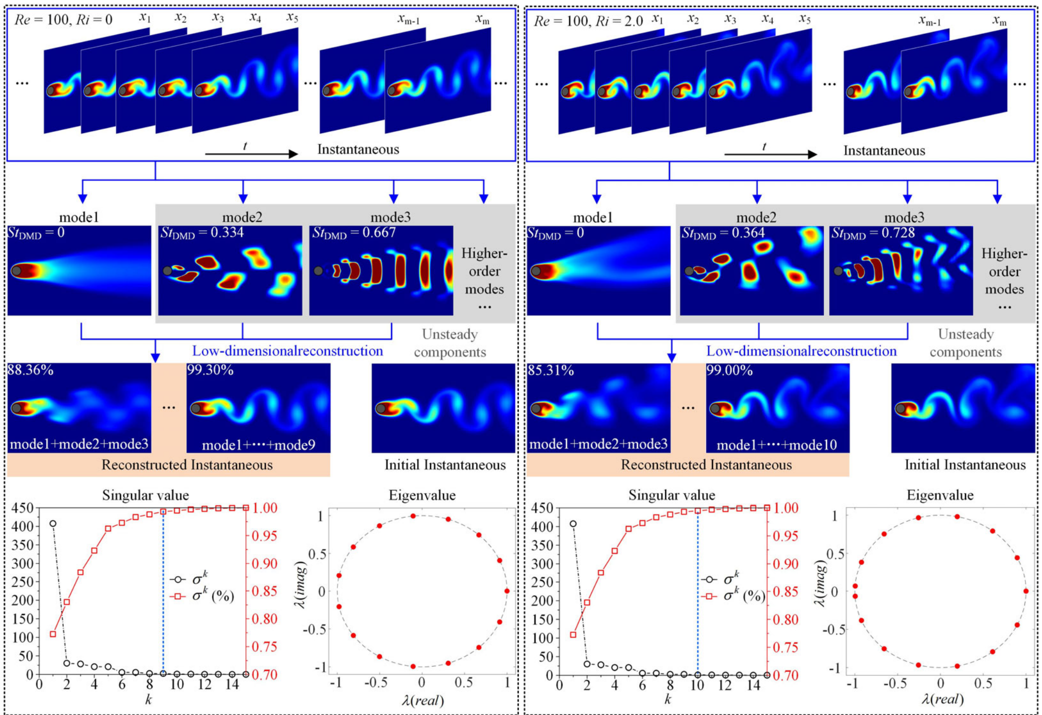

(a) (b)

Figure 27. Schematic diagram of the data processing with DMD algorithm for the normalized temperature (T^*) for (a) Ri = 0 and (b) Ri = 2.

The spatial distribution of the DMD modes of the normalized temperature (T^*) field can be found in Fig. 28. Analogous to the criteria used to determine the value of k for the vorticity field, a suitable value of k is also chosen to reconstruct the instantaneous temperature field based on the criteria σ^k (%) ≥ 99.0% (k < 15). Figure 28 shows that when Ri > 1, the cumulative energy σ^k (%) of the first 14 modes cannot reach 99% for Re = 60. It means that stronger nonlinear feature exist in the temperature field for the wake subject to the cross-buoyancy effect and more linear DMD modes are required to accurately reconstruct the original temperature field. The same conclusion applies for the case of Ri = 2 and Re = 80 as well.

Similar to the discussion of ω_z field, an appropriate value of k parameter should be chosen for the reconstruction of T^* field in advance. Overall, Fig. 28 shows that a higher value of k (more DMD modes) should be chosen for a larger Ri number (strong cross buoyancy) to accurate reconstruct the original temperature field. On the other hand, it is also realized that influence of the cross-buoyancy

Accepted to Phys. Fluids 10.1063/5.0119962

effect is weakened as the fluid inertia force keeps increasing (higher Reynolds number). This can be observed from the curves in Fig. 28, which are converging for different values of Ri numbers. Overall, it is found that the value of $k > 15$ can return an accurate approximation of the original field data in this study.

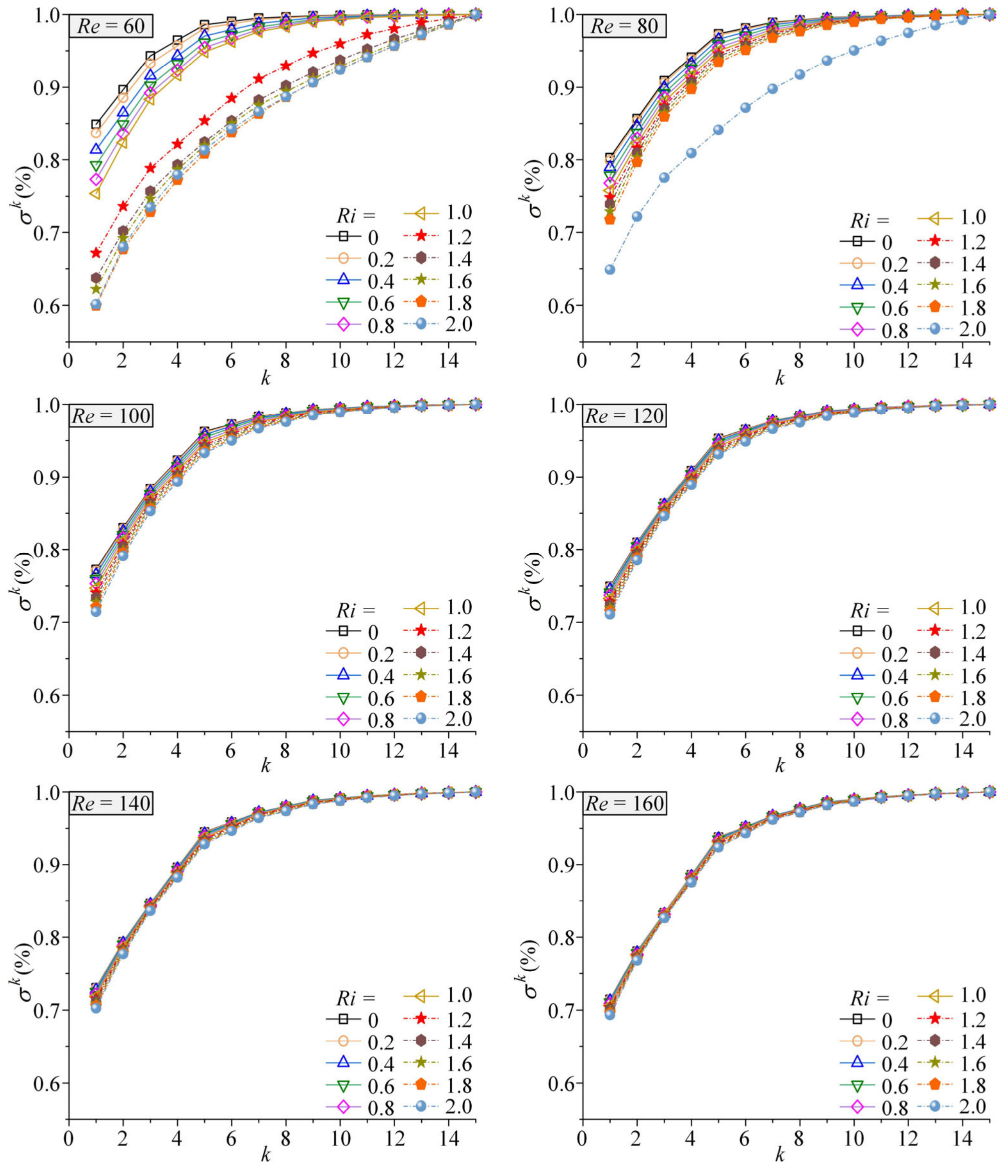

Figure 28. Dependence of σ^k (%) on the value of k for the normalized temperature T^* field.

IV. CONCLUSIONS

Flow over a heated circular cylinder is a canonical issue in thermal engineering. In comparison with the isothermal fluid flow, the buoyancy effect introduced by mixed convective flow may enhance the hydrodynamic instability of a circular cylinder and hence complicated flow regimes in wake. To investigate the hydro- and thermo-dynamic characteristics of a circular cylinder, a numerical study was conducted to investigate the complex mechanism of vortex dynamics in wake and the heat convection along a heated cylinder in mixed convection flow subject to cross buoyancy at $Pr = 0.71$, $Re = 60$–160, and $Ri = 0$–2.0. The employed numerical formulation was validated with the numerical and experimental data in literature.

Since the cross-buoyancy effect is negligible in forced convection ($Ri = 0$), similar to the isothermal fluid flow, it was found that both the distributions of $Nu_{(\theta)}^{\mathrm{mean}}$ and $C_{P(\theta)}$ along the cylinder's surface and the wake structure are symmetric, including the fluid momentum and thermal energy transport (u^*_{mean}, v^*_{mean}, T^*_{mean}, $\overline{u'^*u'^*}$, $\overline{v'^*v'^*}$, $\overline{u'^*v'^*}$, $\overline{u'^*T'^*}$ and $\overline{v'^*T'^*}$). In contrast, because of the presence of thermal cross buoyancy in mixed convection ($Ri > 0$), the wake behind a heated cylinder became significantly asymmetric and deflected against the gravitational direction. In mixed convection, the heat convection across the cylinder's surface is affected by both Re (fluid inertia) and Ri (buoyancy) numbers. In comparison with the Re number, the change of Ri number has less influence on the efficiency of heat transfer across the cylinder's surface. Nevertheless, the value of Nu^{RMS} increases exponentially with the Ri number at $Re = 60$, where the thermal buoyancy overcomes the inertia force with the results of strong nonlinear features and multiple frequency modes. The maximum $C_{\mathrm{L}}^{\mathrm{RMS}}$ of 0.96 is found in the case of $Ri = 2$ and $Re = 60$. Due to the thermal cross buoyancy, multiple harmonics exist in the frequency domain for the dynamics of $Nu_{(\theta)}$, Nu, C_{D} and C_{L}. The fundamental frequency of C_{D} is synchronized with the C_{L} and the second frequency component is about twice of the fundamental one. Furthermore, the dynamics of C_{D} and Nu are synchronized together in time domain, suggesting the strong coupling between the hydrodynamics and buoyancy effects. The pressure on the lower side of the cylinder is lower than that on the upper side, resulting in the negative value of $C_{\mathrm{L}}^{\mathrm{mean}}$. The higher the value of Ri number, the smaller the value of $C_{\mathrm{L}}^{\mathrm{mean}}$.

By quantifying the Reynolds stresses, the cascade of fluid kinetic energy and thermal energy via the fine-scale fluid fluctuation in wake were studied. As Ri number increases, amplified asymmetries are observed in both the velocity and temperature fields. Larger Reynolds stresses are observed in the cases of larger Ri number and smaller Re number, indicating the presence of strong thermal cross-buoyancy against a weaker fluid inertia. As the cross-buoyancy effect becomes stronger, the vortex formation length is reduced, contributing to the enhanced Nu^{RMS} and C_L^{RMS}.

A number of dominant spatial-temporal modes of vorticity and temperature fields were extracted by applying the dynamic mode decomposition technique. It was realized that stronger nonlinear features exist in the wake in mixed convection subject to cross buoyancy as *Ri* number increases, compared with the forced convection. For the reconstruction of spanwise vorticity field at $Ri = 2$ and $Re = 100$, the first 9 DMD modes account for 99.00% of the cumulative energy in the case of forced convection, while the first 12 DMD modes are required in mixed convection. The energy of the first DMD mode decreases with the increase of the *Ri* number. The same phenomenon is found in the reconstruction of temperature field.

In general, the present study reports an insight into the hydro- and thermo-dynamic characteristics of a heated circular cylinder in mixed convection subject to cross buoyancy. The numerical results may provide references for the design of heat exchange tubes and the operation of exchangers.

ACKNOWLEDGMENTS

This research was supported by the National Natural Science Foundation of China (No. 51979238), the Fundamental Research Funds of National Center for International Research of Subsea Engineering and Equipment (No. 3132022354) and the Graduate Research Innovation Fund project of Southwest Petroleum University (No. 2021CXYB52). The work was carried out in the computer cluster of the laboratory of offshore oil and gas engineering at Southwest Petroleum University.

DATA AVAILABILITY STATEMENT

The data that support the findings of this study are available from the corresponding author upon reasonable request.

REFERENCES

[1]T. von Kármán and H. Rubach, “Über den Mechanismus des Flüssigkeits-und Luft-widerstandes,” Phys. Z. **13** 49–59 (1912).

[2]A. Roshko, “On the development of turbulent wakes from vortex streets,” No. NACA-TR-1191 (1954).

[3]F. H. Abernathy and R. E. Kronauer, “The formation of vortex streets,” J. Fluid Mech. **13** 1–20 (1962).

[4]E. Berger and R. Wille, “Periodic flow phenomena,” Annu. Rev. Fluid Mech. **4** 313–340 (1972).

[5]P. W. Bearman, “Vortex shedding from oscillating bluff bodies,” Annu. Rev. Fluid Mech. **16** 195–222

(1984).

[6]C. Williamson, "The existence of two stages in the transition to three-dimensionality of a cylinder wake," Phys. Fluids **31** 3165–3168 (1988).

[7]H. Jiang, L. Cheng, S. Draper, H. An, and F. Tong, "Three-dimensional direct numerical simulation of wake transitions of a circular cylinder," J. Fluid Mech. **801** 353–391 (2016).

[8]C. H. Williamson, "Oblique and parallel modes of vortex shedding in the wake of a circular cylinder at low Reynolds numbers," J. Fluid Mech. **206** 579–627 (1989).

[9]R. D. Henderson, "Nonlinear dynamics and pattern formation in turbulent wake transition," J. Fluid Mech. **352** 65–112 (1997).

[10]E. Schmidt and K. Wenner, "Heat transfer over the circumference of a heated cylinder in transverse flow," Forsch. Auf Dem Geb. Ingenieurwesens **12** (1943).

[11]G. E. Karniadakis, "Numerical simulation of forced convection heat transfer from a cylinder in crossflow," Int. J. Heat Mass Transf. **31** 107–118 (1988).

[12]C. Gau, J. M. Wu, and C. Y. Liang, "Heat transfer enhancement and vortex flow structure over a heated cylinder oscillating in the crossflow direction," J. Heat Transf. **121** 789–795 (1999).

[13]S. Sarkar, A. Dalal, and G. Biswas, "Unsteady wake dynamics and heat transfer in forced and mixed convection past a circular cylinder in cross flow for high Prandtl numbers," Int. J. Heat Mass Transf. **54** 3536–3551 (2011).

[14]I. Paul, K. Arul Prakash, S. Vengadesan, and V. Pulletikurthi, "Analysis and characterisation of momentum and thermal wakes of elliptic cylinders," J. Fluid Mech. **807** 303–323 (2016).

[15]H. Badr, "A theoretical study of laminar mixed convection from a horizontal cylinder in a cross stream," Int. J. Heat Mass Transf. **26** 639–653 (1983).

[16]H. Badr, "Laminar combined convection from a horizontal cylinder—parallel and contra flow regimes," Int. J. Heat Mass Transf. **27** 15–27 (1984).

[17]N. D. Joshi and S. P. Sukhatme, "An analysis of combined free and forced convection heat transfer from a horizontal circular cylinder to a transverse flow," J. Heat Transf. **93** 441–448 (1971).

[18]D. Chatterjee, "Dual role of thermal buoyancy in controlling boundary layer separation around bluff obstacles," Int. Commun. Heat Mass Transf. **56** 152–158 (2014).

[19]D. Chatterjee and B. Mondal, "Control of flow separation around bluff obstacles by superimposed thermal buoyancy," Int. J. Heat Mass Transf. **72** 128–138 (2014).

[20]S. Singh and D. Chandar, “Effects of thermal induced buoyancy forces on the vortex shedding of a circular cylinder,” Int. Commun. Heat Mass Transf. **76** 215–224 (2016).

[21]L. Houssem, “Suppression of flow separation of power-law fluids flow around a confined circular cylinder by superimposed thermal buoyancy,” Mechanics **23** 220–227 (2017).

[22]G. F. Al-Sumaily, H. A. Dhahad, H. M. Hussen, and M. C. Thompson, “Influence of thermal buoyancy on vortex shedding behind a circular cylinder in parallel flow,” Int. J. Therm. Sci. **156** 106434 (2020).

[23]H. Hu and M. M. Koochesfahani, “Thermal effects on the wake of a heated circular cylinder operating in mixed convection regime,” J. Fluid Mech. **685** 235–270 (2011).

[24]K. S. Chang and J. Y. Sa, “The effect of buoyancy on vortex shedding in the near wake of a circular cylinder,” J. Fluid Mech. **220** 253–266 (1990).

[25]B. S. V. Patnaik, P. A. A. Narayana, and K. N. Seetharamu, “Numerical simulation of vortex shedding past a circular cylinder under the influence of buoyancy,” Int J Heat Mass Transf. **42** 3495–3507 (1999).

[26]H. Garg, A. K. Soti, and R. Bhardwaj, “Vortex-induced vibration of a cooled circular cylinder,” Phys. Fluids **31** 083608 (2019).

[27]K. Hatanaka and M. Kawahara, “A numerical study of vortex shedding around a heated/cooled circular cylinder by the three-step Taylor-Galerkin method,” Int. J. Numer. Methods Fluids **21** 857–867 (1995).

[28]A. Hatton, D. James, and H. Swire, “Combined forced and natural convection with low-speed air flow over horizontal cylinders,” J. Fluid Mech. **42** 17–31 (1970).

[29]J. Mi and R. Antonia, “Temperature distribution within vortices in the wake of a cylinder,” Int. J. Heat Mass Transf. **37** 1048–1050 (1994).

[30]R. N. Kieft, C. C. M. Rindt, A. A. van STEENHOVEN, and G. J. F. van HEIJST, “On the wake structure behind a heated horizontal cylinder in cross-flow,” J. Fluid Mech. **486** 189–211 (2003).

[31]D. Chatterjee and B. Mondal, “Effect of thermal buoyancy on fluid flow and heat transfer across a semicircular cylinder in cross-flow at low reynolds numbers,” Numer. Heat Transf. Part Appl. **67** 436–453 (2015).

[32]B. Liu and H. Zhu, “Secondary lock-in of vortex-induced vibration and energy transfer characteristics of a vibrating cylinder subject to cross buoyancy,” Phys. Fluids **33** 073607 (2021).

[33]R. Kieft, C. C. Rindt, and A. A. Van Steenhoven, “The influence of buoyancy on the behavior of the vortex structures in a cylinder wake,” Heat Transf. **3** 219–224 (1998).

[34]R. N. Kieft, C. C. M. Rindt, and A. A. van Steenhoven, “The wake behaviour behind a heated horizontal

cylinder," Exp. Therm. Fluid Sci. **19** 183–193 (1999).

[35]R. Kieft, K. Schreel, G. van der Plas, and C. Rindt, "The application of a 3D PTV algorithm to a mixed convection flow," Exp. Fluids **33** 603–611 (2002).

[36]R. Kieft, C. Rindt, and A. Van Steenhoven, "Heat induced transition of a stable vortex street," Int. J. Heat Mass Transf. **45** 2739–2753 (2002).

[37]A. A. van Steenhoven and C. C. M. Rindt, "Flow transition behind a heated cylinder," Int. J. Heat Fluid Flow **24** 322–333 (2003).

[38]G. Biswas and S. Sarkar, "Effect of thermal buoyancy on vortex shedding past a circular cylinder in cross-flow at low Reynolds numbers," Int. J. Heat Mass Transf. **52** 1897–1912 (2009).

[39]H. Garg, A. K. Soti, and R. Bhardwaj, "Vortex-induced vibration and galloping of a circular cylinder in presence of cross-flow thermal buoyancy," Phys. Fluids **31** 113603 (2019).

[40]K. Taira et al., "Modal Analysis of Fluid Flows: An Overview," AIAA J. **55** 4013–4041 (2017).

[41]B. Wang and M. Yu, "Analysis of wake structures behind an oscillating square cylinder using dynamic mode decomposition," 46th AIAA Fluid Dynamics Conference 3779 (2016).

[42]J. Tu, C. Rowley, E. Aram, and R. Mittal, "Koopman spectral analysis of separated flow over a finite-thickness flat plate with elliptical leading edge," 49th AIAA Aerospace Sciences Meeting including the New Horizons Forum and Aerospace Exposition (2011).

[43]J. H. Tu, J. Griffin, A. Hart, C. W. Rowley, L. N. Cattafesta, and L. S. Ukeiley, "Integration of non-time-resolved PIV and time-resolved velocity point sensors for dynamic estimation of velocity fields," Exp. Fluids **54** 1–20 (2013).

[44]T. K. Prasanth, S. Behara, S. P. Singh, R. Kumar, and S. Mittal, "Effect of blockage on vortex-induced vibrations at low Reynolds numbers," J. Fluids Struct. **22** 865–876 (2006).

[45]M. Zhao, F. Tong, and L. Cheng, "Numerical simulation of two-degree-of-freedom vortex-induced vibration of a circular cylinder between two lateral plane walls in steady currents," J. Fluids Eng. **134** 104501 (2012).

[46]S. W. Churchill and M. Bernstein, "A correlating equation for forced convection from gases and liquids to a circular cylinder in crossflow," J. Heat Transf. **99** 300–306 (1977).

[47]G. Juncu, "A numerical study of momentum and forced convection heat transfer around two tandem circular cylinders at low Reynolds numbers. Part II: Forced convection heat transfer," Int. J. Heat Mass Transf. **50** 3799–3808 (2007).

[48]D. Barkley and R. D. Henderson, “Three-dimensional Floquet stability analysis of the wake of a circular cylinder,” J. Fluid Mech. **322** 215–241 (1996).

[49]M. Hammache and M. Gharib, “An experimental study of the parallel and oblique vortex shedding from circular cylinders,” J. Fluid Mech. **232** 567–590 (1991).

[50]C. H. K. Williamson, “Vortex Dynamics in the Cylinder Wake,” Annu. Rev. Fluid Mech. **28** 477–539 (1996).

[51]W. Chen, C. Ji, M. M. Alam, J. Williams, and D. Xu, “Numerical simulations of flow past three circular cylinders in equilateral-triangular arrangements,” J. Fluid Mech. **891** (2020).

[52]F. Zafar and Md. M. Alam, “A low Reynolds number flow and heat transfer topology of a cylinder in a wake,” Phys. Fluids **30** 083603 (2018).

[53]G. Chopra and S. Mittal, “Secondary vortex, laminar separation bubble and vortex shedding in flow past a low aspect ratio circular cylinder,” J. Fluid Mech. **930** (2022).

[54]F. Zafar and Md. M. Alam, “Mixed convection heat transfer from a circular cylinder submerged in wake,” Int. J. Mech. Sci. **183** 105733 (2020).

[55]F. Zafar and Md. M. Alam, “Flow structure around and heat transfer from cylinders modified from square to circular,” Phys. Fluids **31** 083604 (2019).

[56]K. Taira et al., “Modal analysis of fluid flows: applications and outlook,” AIAA J. **58** 998–1022 (2020).

[57]S. Bagheri, “Koopman-mode decomposition of the cylinder wake,” J. Fluid Mech. **726** 596–623 (2013).

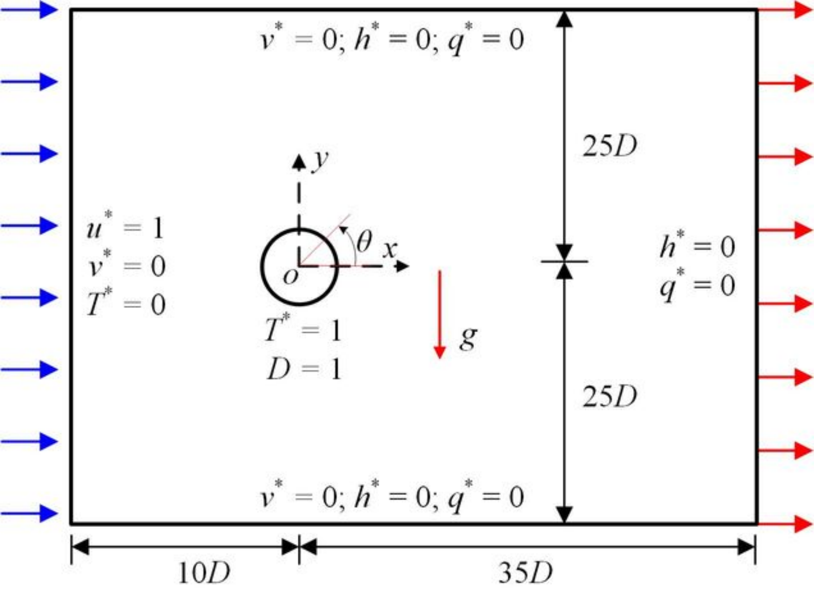

$v^* = 0; h^* = 0; q^* = 0$
25D
y
$u^* = 1$
$v^* = 0$
$T^* = 0$
θ
x
o
$h^* = 0$
$q^* = 0$
$T^* = 1$
$D = 1$
g
25D
$v^* = 0; h^* = 0; q^* = 0$
10D
35D

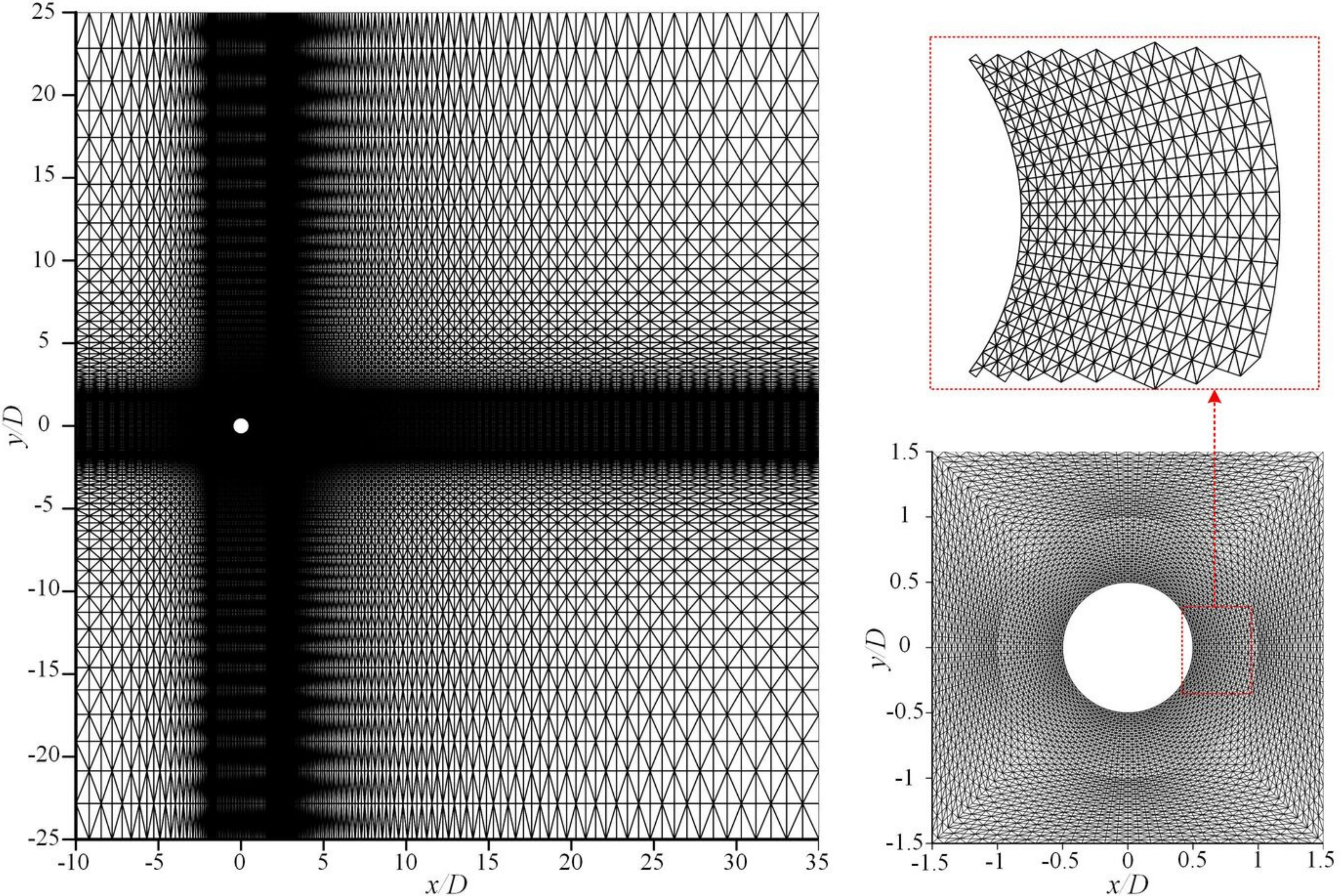

y/D
x/D
25
20
15
10
5
0
-5
-10
-15
-20
-25
-10
-5
0
5
10
15
20
25
30
35
1.5
1
0.5
0
-0.5
-1
-1.5

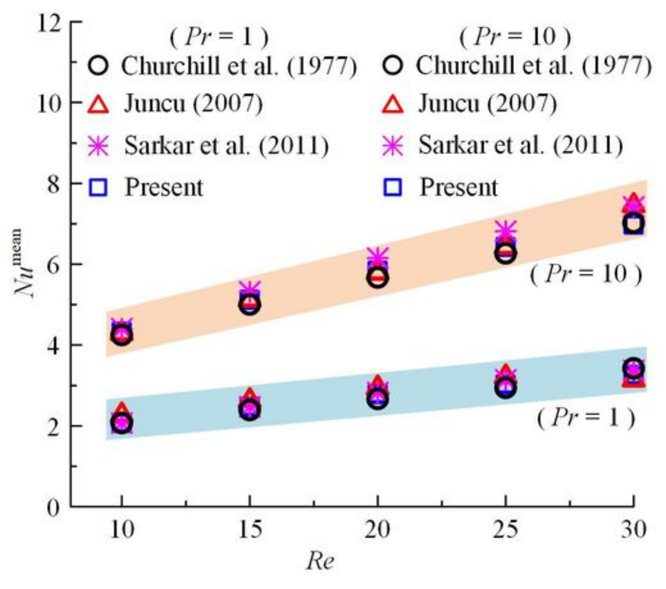

(Pr = 1)
Churchill et al. (1977)
Juncu (2007)
Sarkar et al. (2011)
Present
(Pr = 10)
Churchill et al. (1977)
Juncu (2007)
Sarkar et al. (2011)
Present
(Pr = 10)
(Pr = 1)
Nu^{mean}
Re
0
2
4
6
8
10
12
10
15
20
25
30

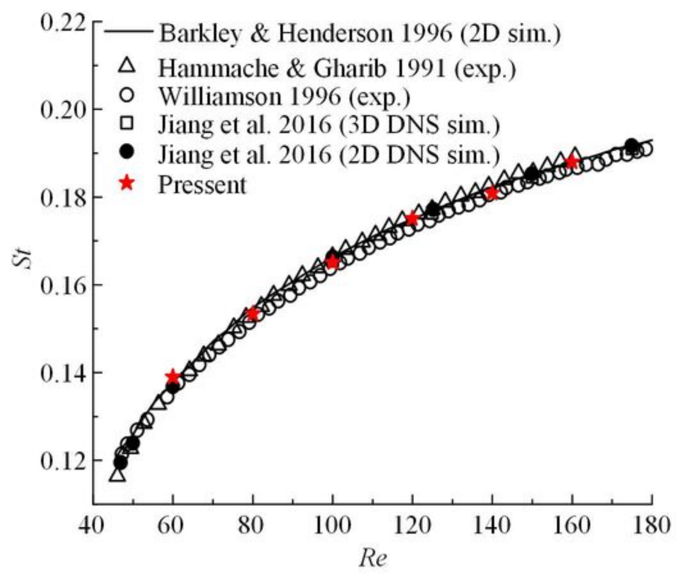

Barkley & Henderson 1996 (2D sim.)
Hammache & Gharib 1991 (exp.)
Williamson 1996 (exp.)
Jiang et al. 2016 (3D DNS sim.)
Jiang et al. 2016 (2D DNS sim.)
Pressent
St
Re
0.22
0.20
0.18
0.16
0.14
0.12
40
60
80
100
120
140
160
180

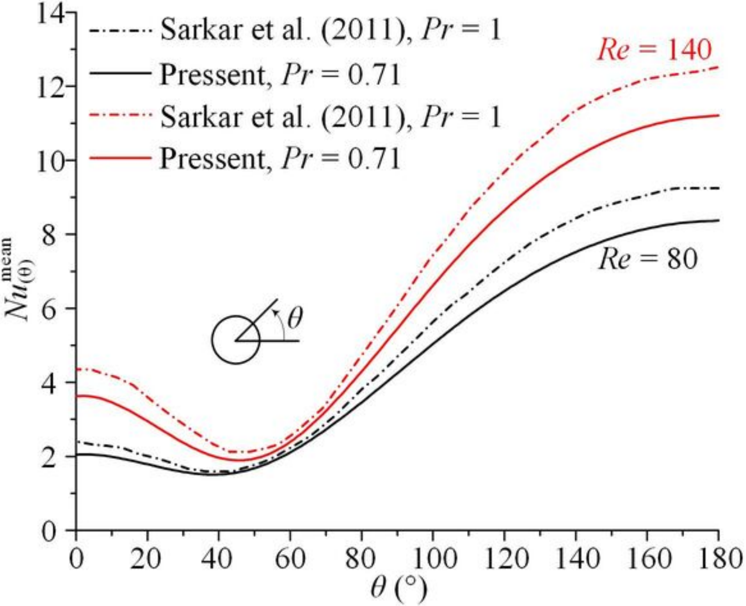

Sarkar et al. (2011), Pr = 1
Pressent, Pr = 0.71
Sarkar et al. (2011), Pr = 1
Pressent, Pr = 0.71
Re = 140
Re = 80
θ
$Nu_{(\theta)}^{\text{mean}}$
θ (°)
0
2
4
6
8
10
12
14
0
20
40
60
80
100
120
140
160
180

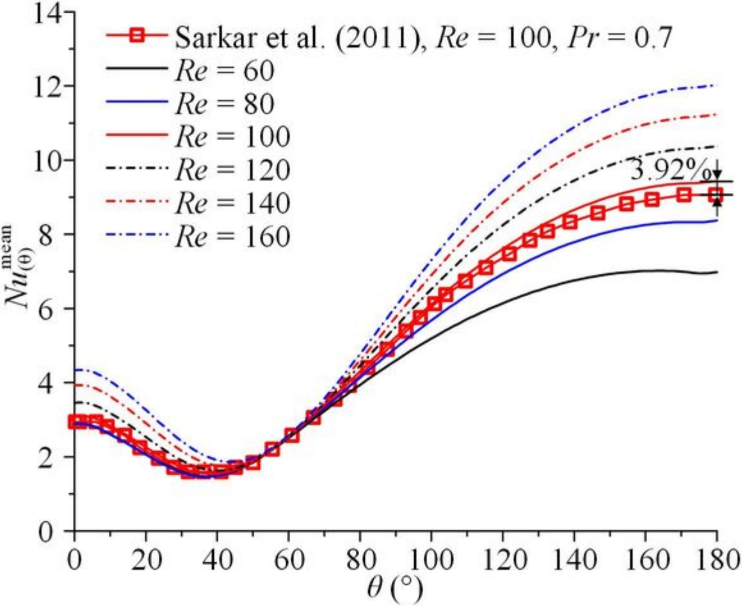

Sarkar et al. (2011), Re = 100, Pr = 0.7
Re = 60
Re = 80
Re = 100
Re = 120
Re = 140
Re = 160
3.92%
$Nu_{(\theta)}^{mean}$
θ (°)
0
2
4
6
8
10
12
14
0
20
40
60
80
100
120
140
160
180

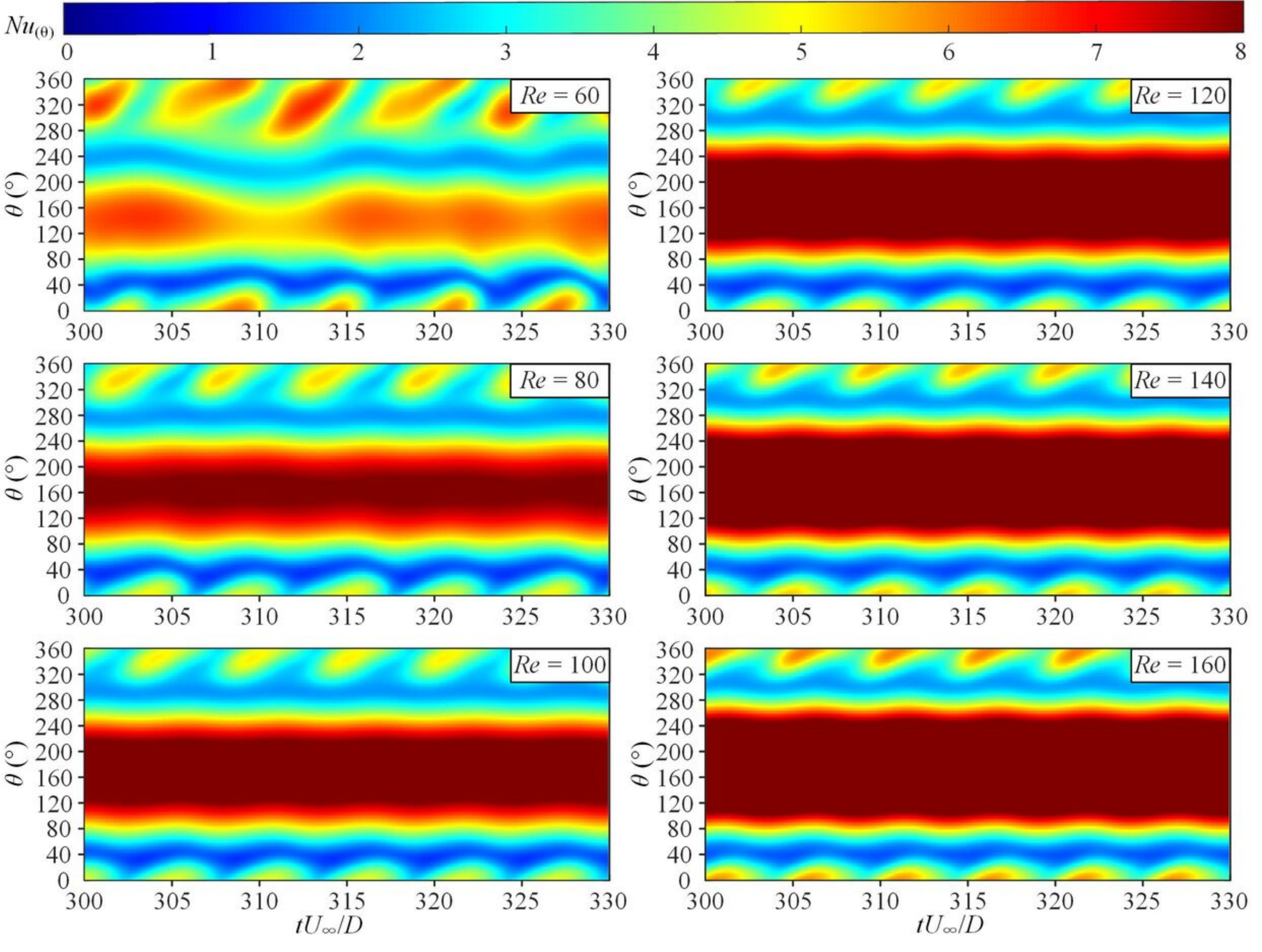

$Nu_{(\theta)}$
0
1
2
3
4
5
6
7
8
Re = 60
Re = 80
Re = 100
Re = 120
Re = 140
Re = 160
θ (°)
tU_∞/D

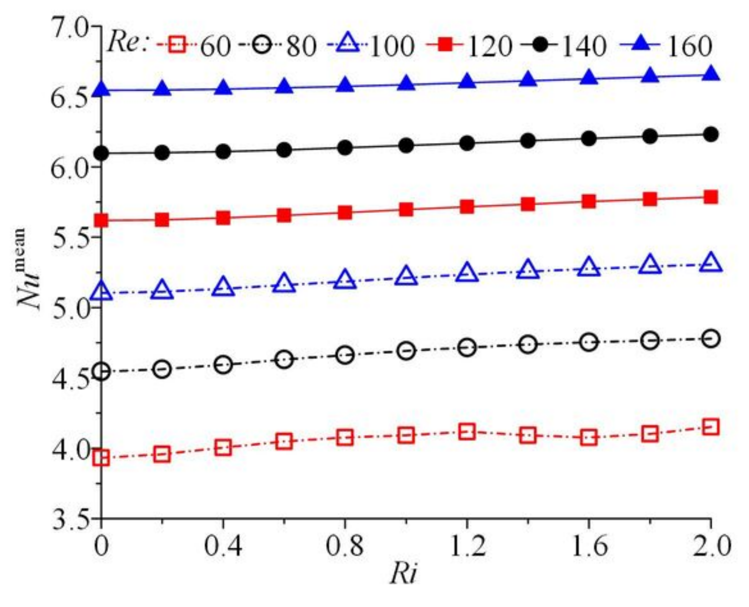

Re: 60 80 100 120 140 160
7.0
6.5
6.0
5.5
5.0
4.5
4.0
3.5
Nu^{mean}
0
0.4
0.8
1.2
1.6
2.0
Ri

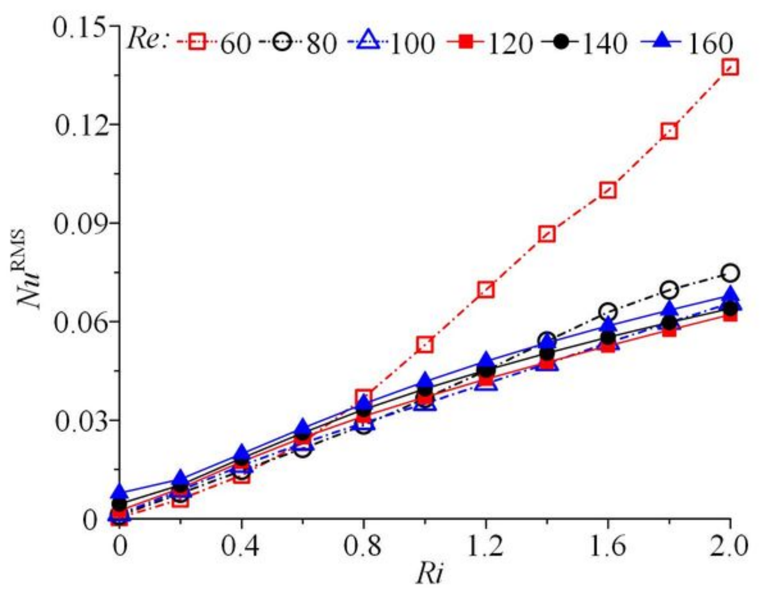
Re: 60 80 100 120 140 160
0.15
0.12
0.09
0.06
0.03
0
Nu^{RMS}
0
0.4
0.8
1.2
1.6
2.0
Ri

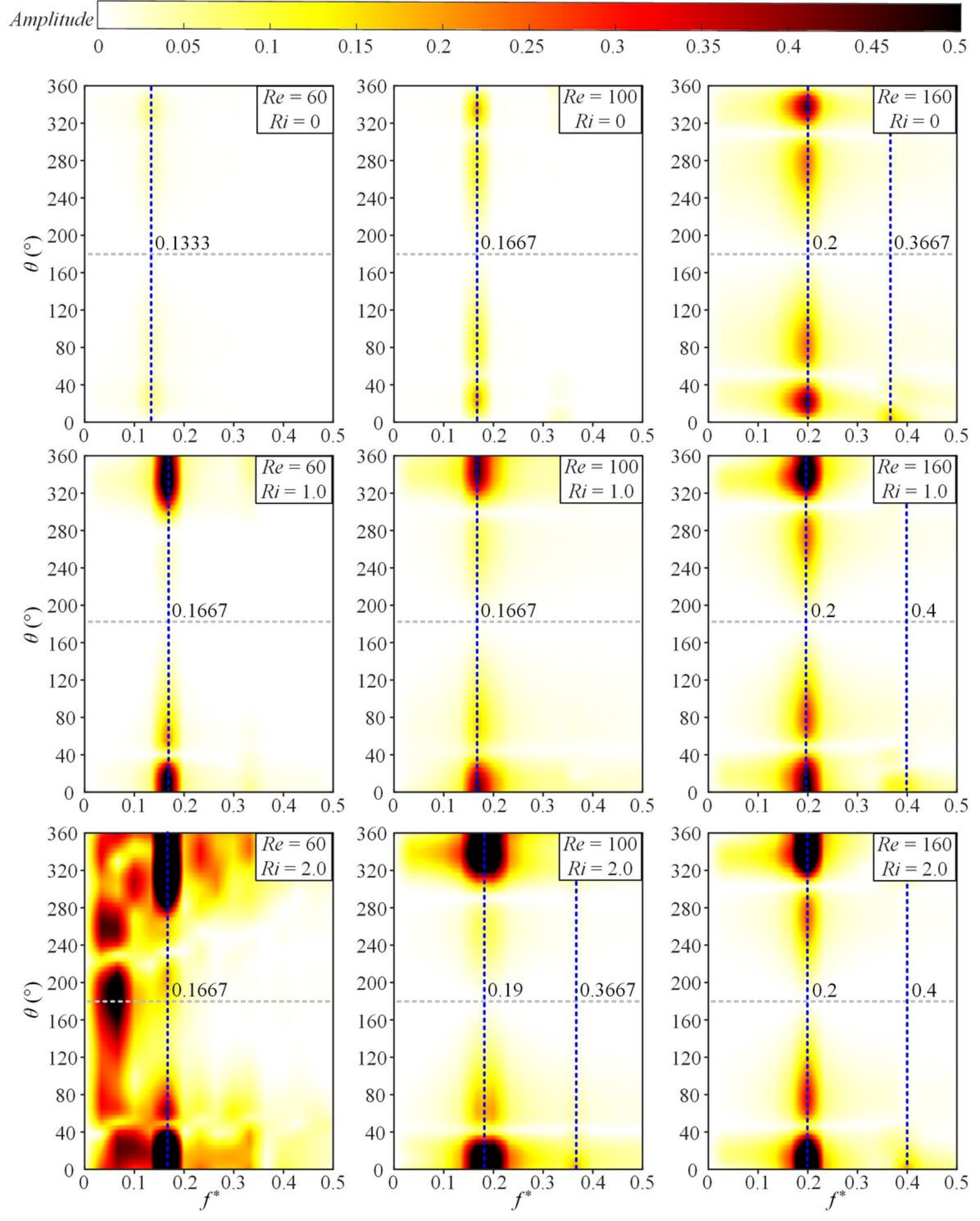

Amplitude
0
0.05
0.1
0.15
0.2
0.25
0.3
0.35
0.4
0.45
0.5
Re = 60
Ri = 0
0.1333
Re = 100
Ri = 0
0.1667
Re = 160
Ri = 0
0.2
0.3667
Re = 60
Ri = 1.0
0.1667
Re = 100
Ri = 1.0
0.1667
Re = 160
Ri = 1.0
0.2
0.4
Re = 60
Ri = 2.0
0.1667
Re = 100
Ri = 2.0
0.19
0.3667
Re = 160
Ri = 2.0
0.2
0.4
θ (°)
f*

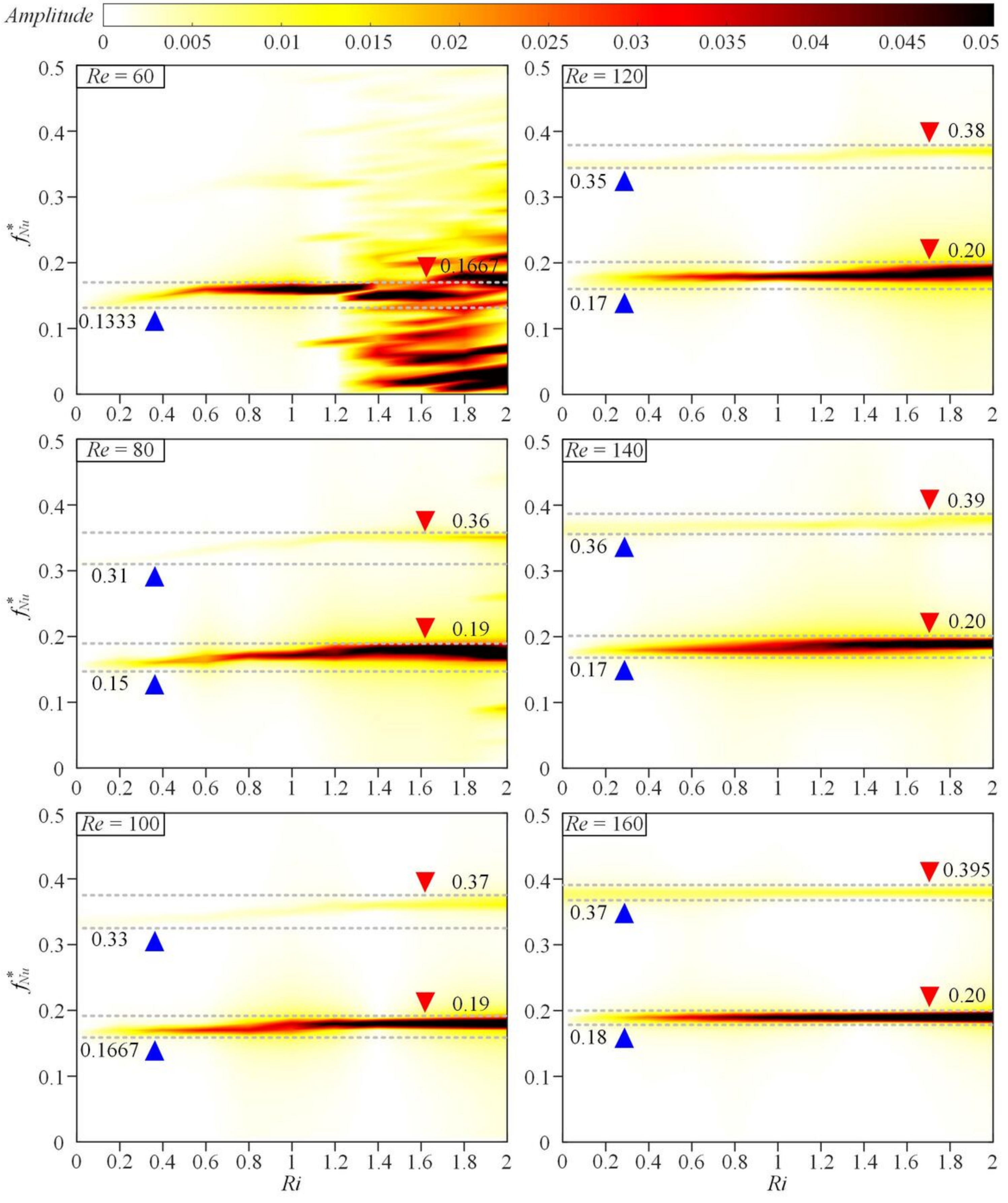

Amplitude
0
0.005
0.01
0.015
0.02
0.025
0.03
0.035
0.04
0.045
0.05
Re = 60
Re = 120
Re = 80
Re = 140
Re = 100
Re = 160
f^*_{Nu}
Ri
0.1667
0.1333
0.38
0.35
0.20
0.17
0.36
0.31
0.19
0.15
0.39
0.36
0.20
0.17
0.37
0.33
0.19
0.1667
0.395
0.37
0.20
0.18

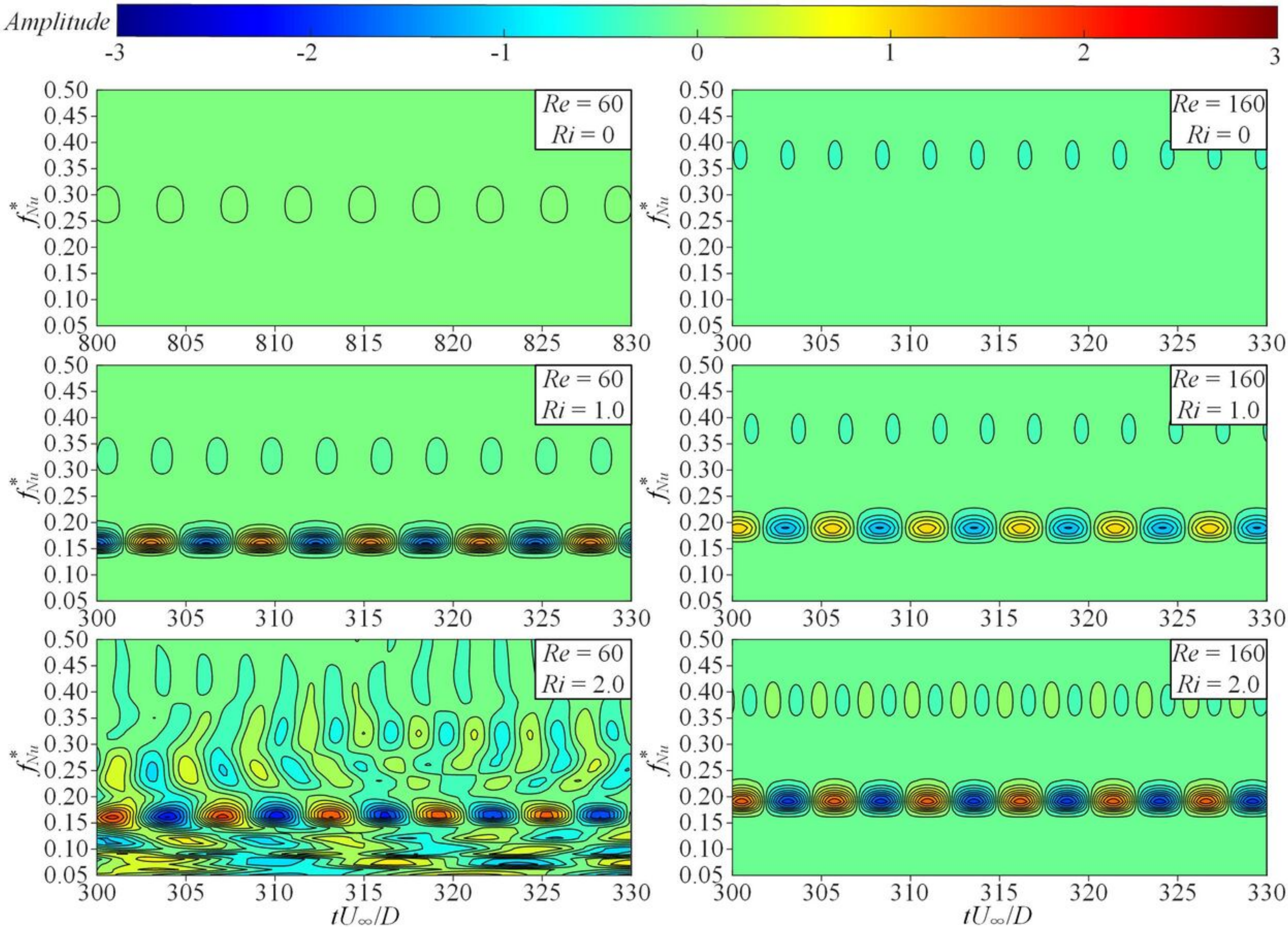

Amplitude
-3
-2
-1
0
1
2
3
Re = 60
Ri = 0
Re = 160
Ri = 0
Re = 60
Ri = 1.0
Re = 160
Ri = 1.0
Re = 60
Ri = 2.0
Re = 160
Ri = 2.0
f^*_{Nu}
tU_∞/D

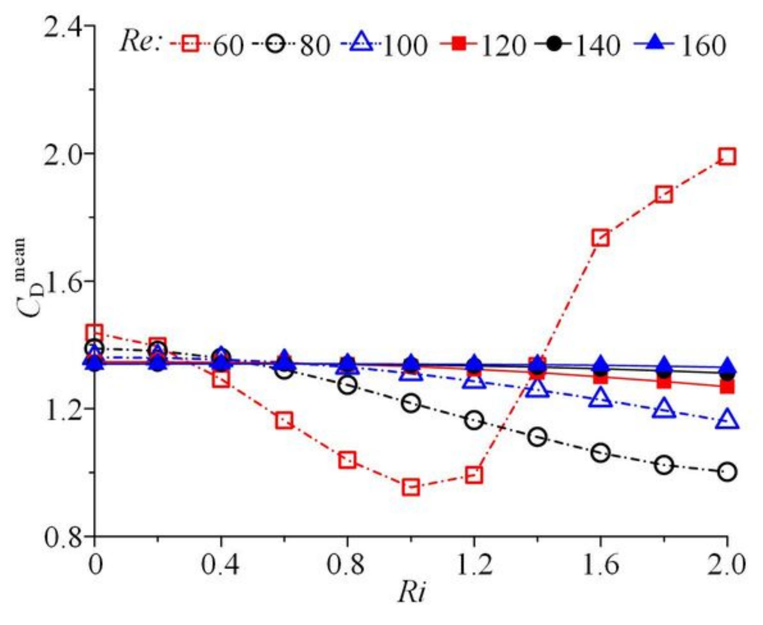

Re:
60
80
100
120
140
160
2.4
2.0
1.6
1.2
0.8
C_D^{mean}
0
0.4
0.8
1.2
1.6
2.0
Ri

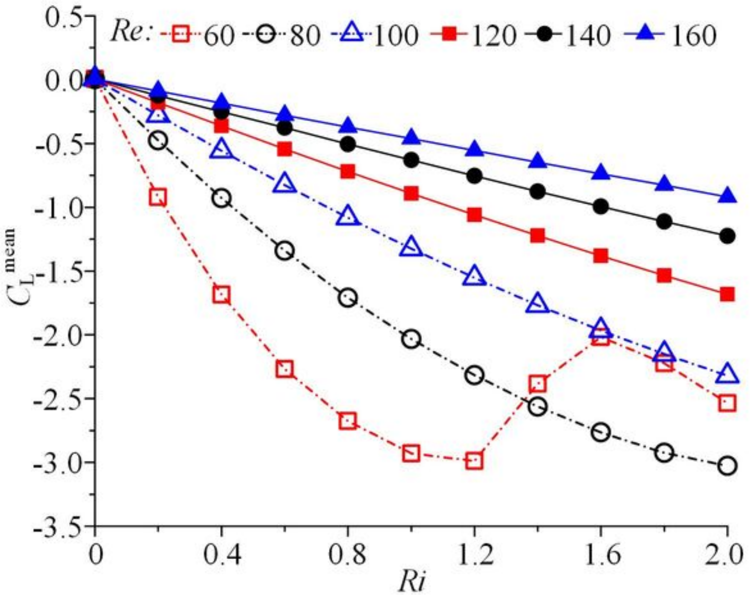

Re: 60 80 100 120 140 160
C_L^{mean}
0.5
0.0
-0.5
-1.0
-1.5
-2.0
-2.5
-3.0
-3.5
0
0.4
0.8
1.2
1.6
2.0
Ri

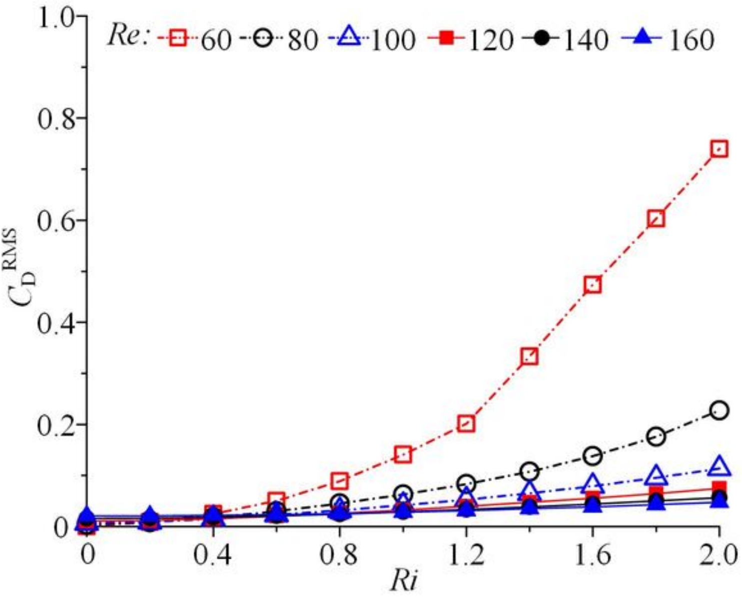

Re: 60 80 100 120 140 160
C_D^{RMS}
Ri
1.0
0.8
0.6
0.4
0.2
0
0.4
0.8
1.2
1.6
2.0

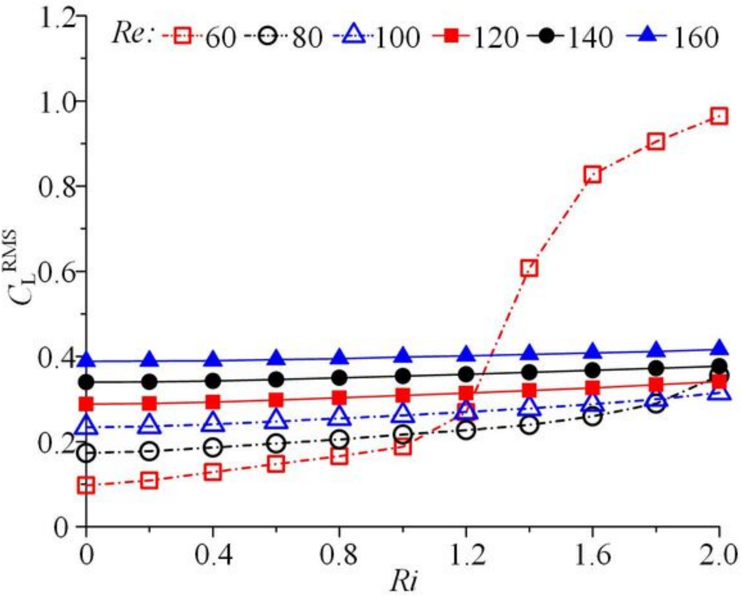

Re: 60 80 100 120 140 160
C_L^{RMS}
Ri
0
0.2
0.4
0.6
0.8
1.0
1.2
0
0.4
0.8
1.2
1.6
2.0

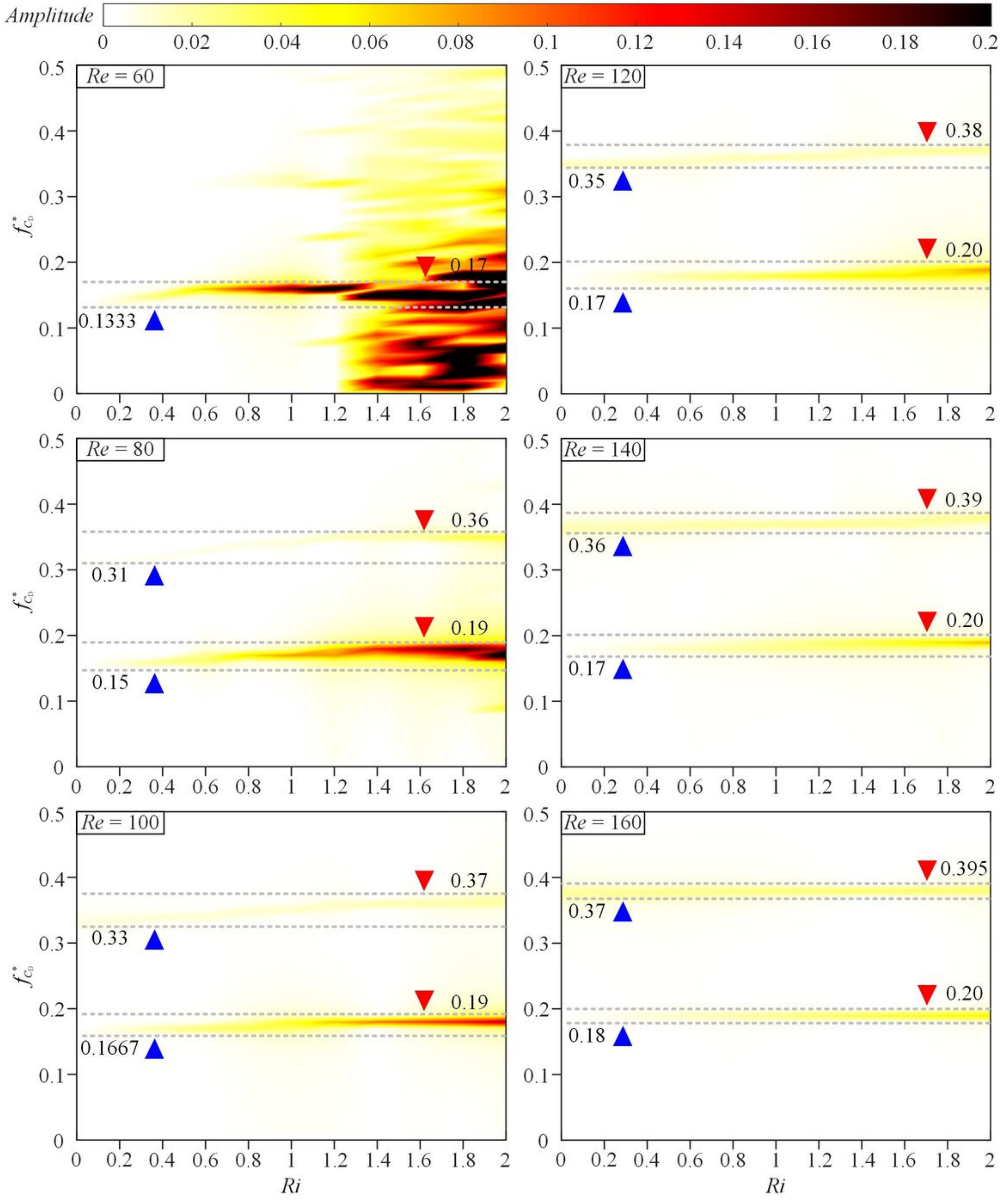

Amplitude
0
0.02
0.04
0.06
0.08
0.1
0.12
0.14
0.16
0.18
0.2
Re = 60
0.17
0.1333
Re = 120
0.38
0.35
0.20
0.17
Re = 80
0.36
0.31
0.19
0.15
Re = 140
0.39
0.36
0.20
0.17
Re = 100
0.37
0.33
0.19
0.1667
Re = 160
0.395
0.37
0.20
0.18
$f^*_{C_D}$
Ri

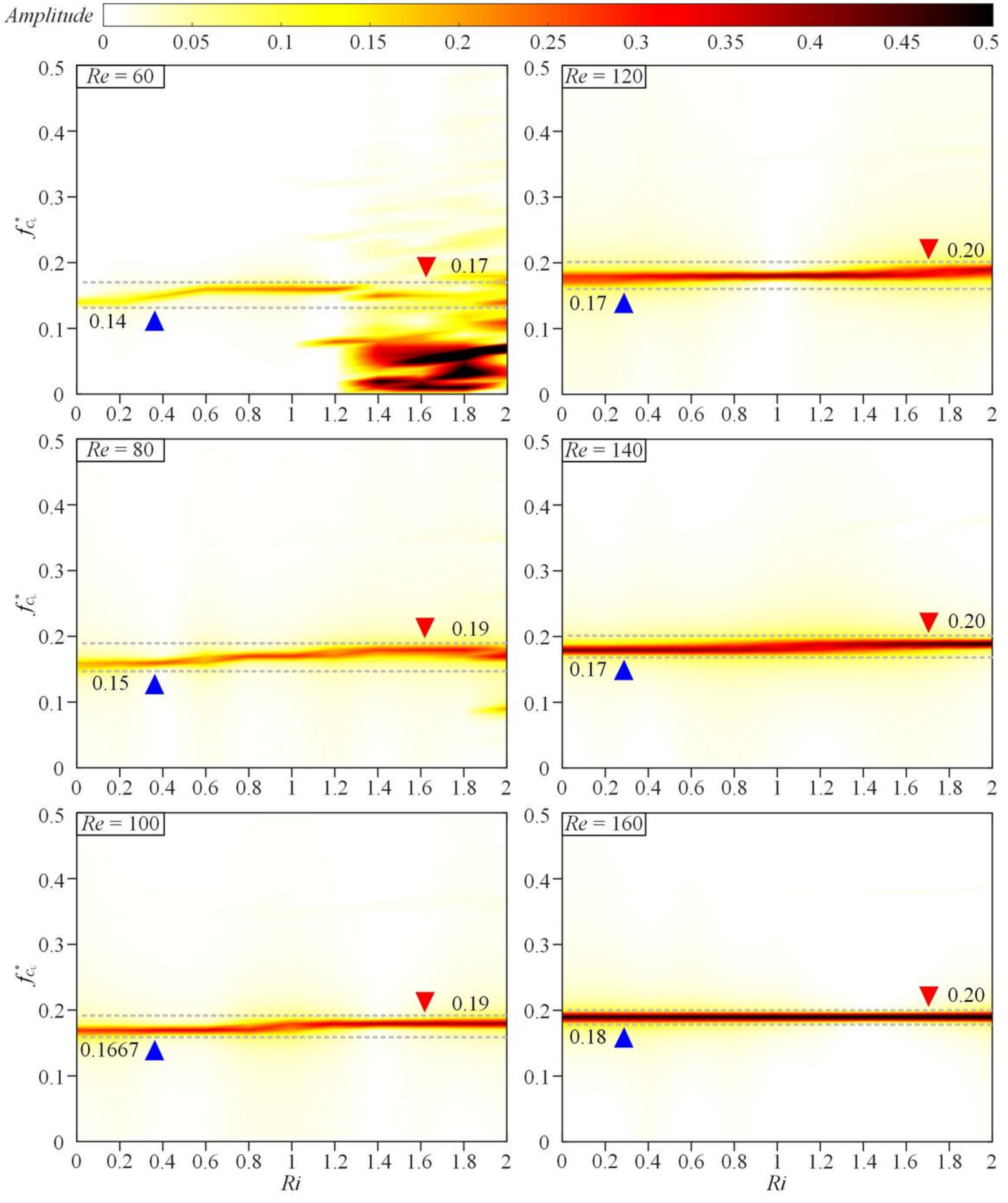

Amplitude
0
0.05
0.1
0.15
0.2
0.25
0.3
0.35
0.4
0.45
0.5
Re = 60
0.17
0.14
Re = 120
0.20
0.17
Re = 80
0.19
0.15
Re = 140
0.20
0.17
Re = 100
0.19
0.1667
Re = 160
0.20
0.18
$f^*_{C_L}$
Ri

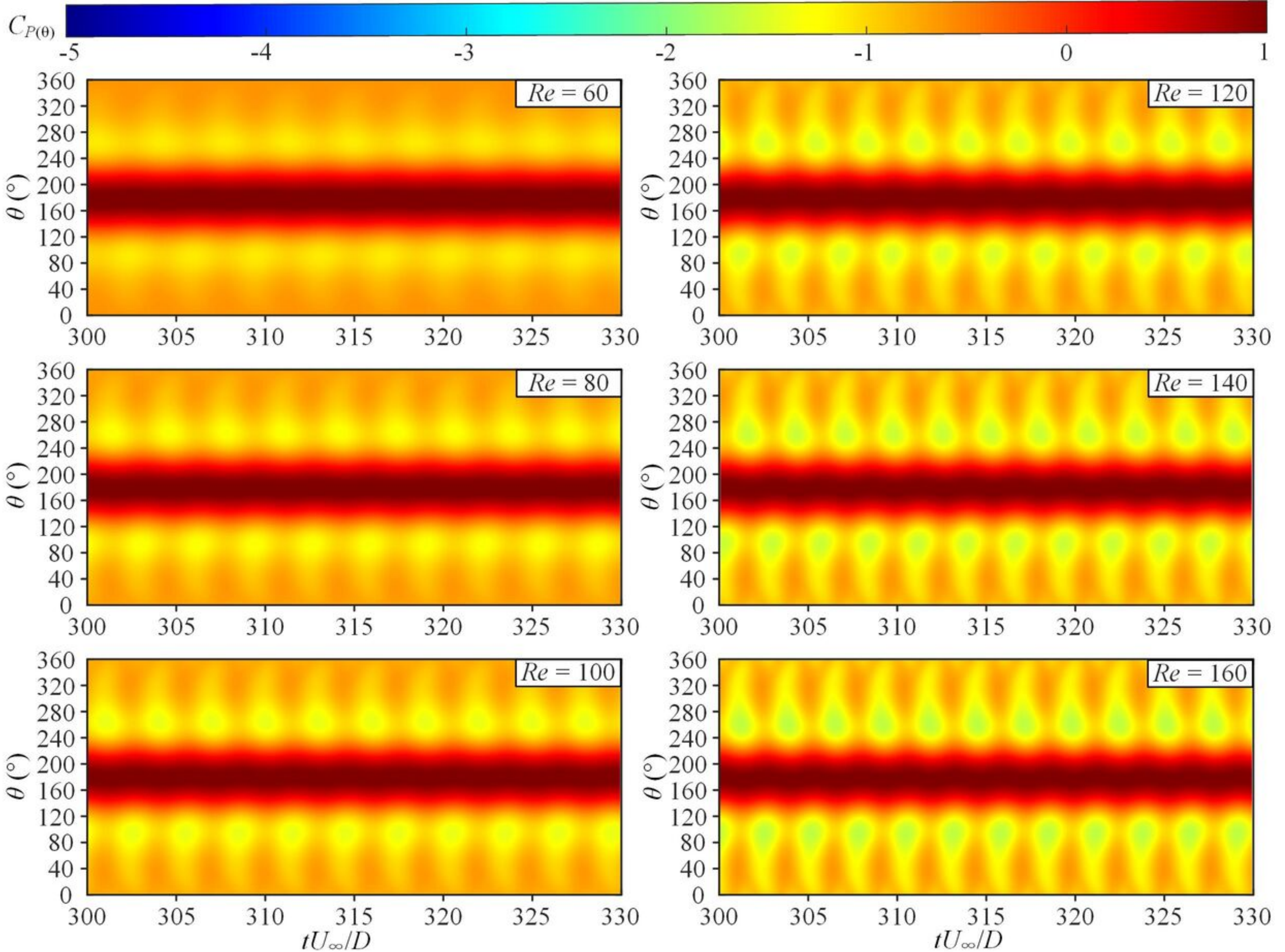

$C_{P(\theta)}$
-5
-4
-3
-2
-1
0
1
Re = 60
Re = 80
Re = 100
Re = 120
Re = 140
Re = 160
θ (°)
tU_∞/D

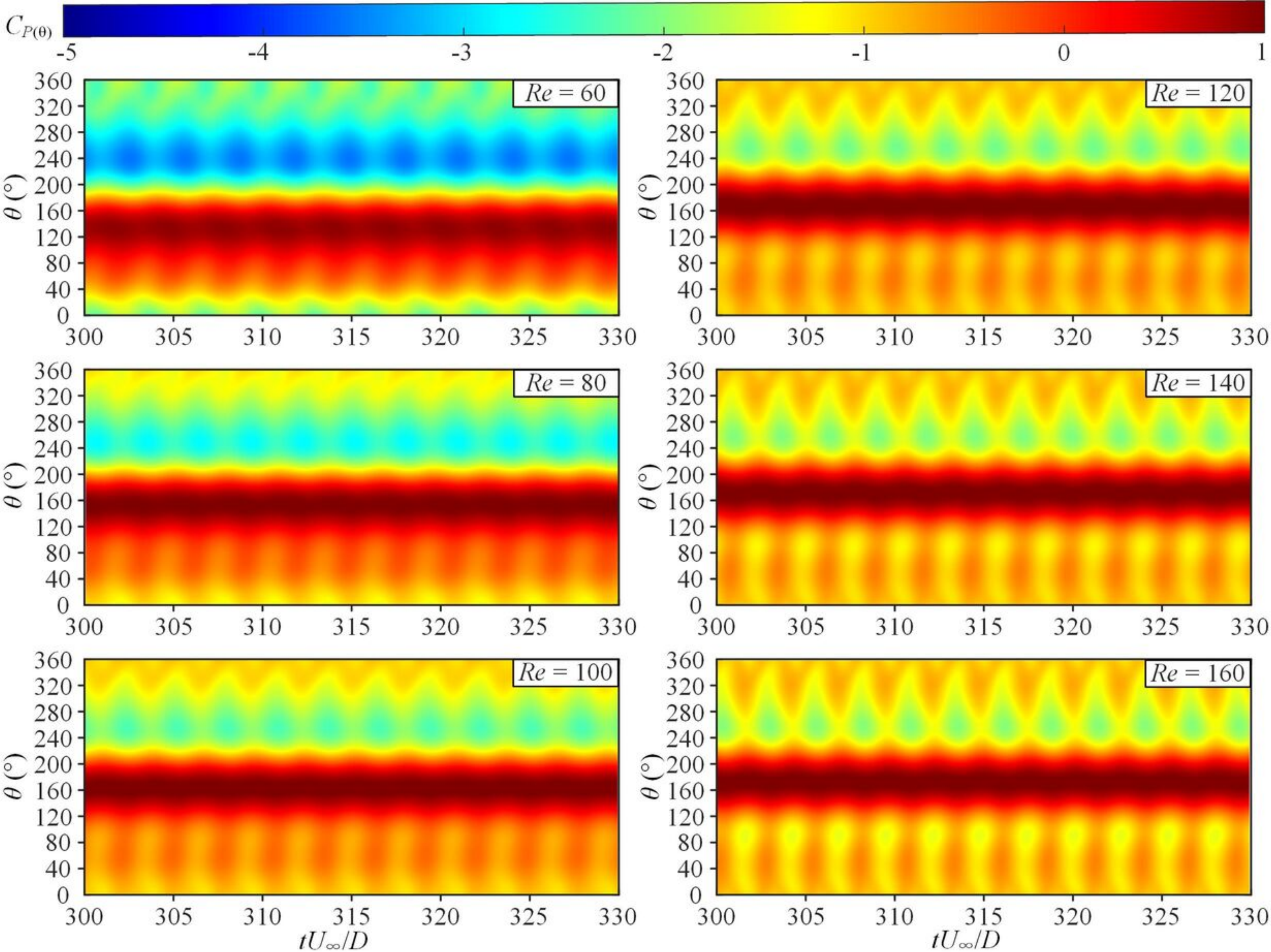

$C_{P(\theta)}$
-5
-4
-3
-2
-1
0
1
Re = 60
Re = 80
Re = 100
Re = 120
Re = 140
Re = 160
θ (°)
0
40
80
120
160
200
240
280
320
360
300
305
310
315
320
325
330
tU_∞/D

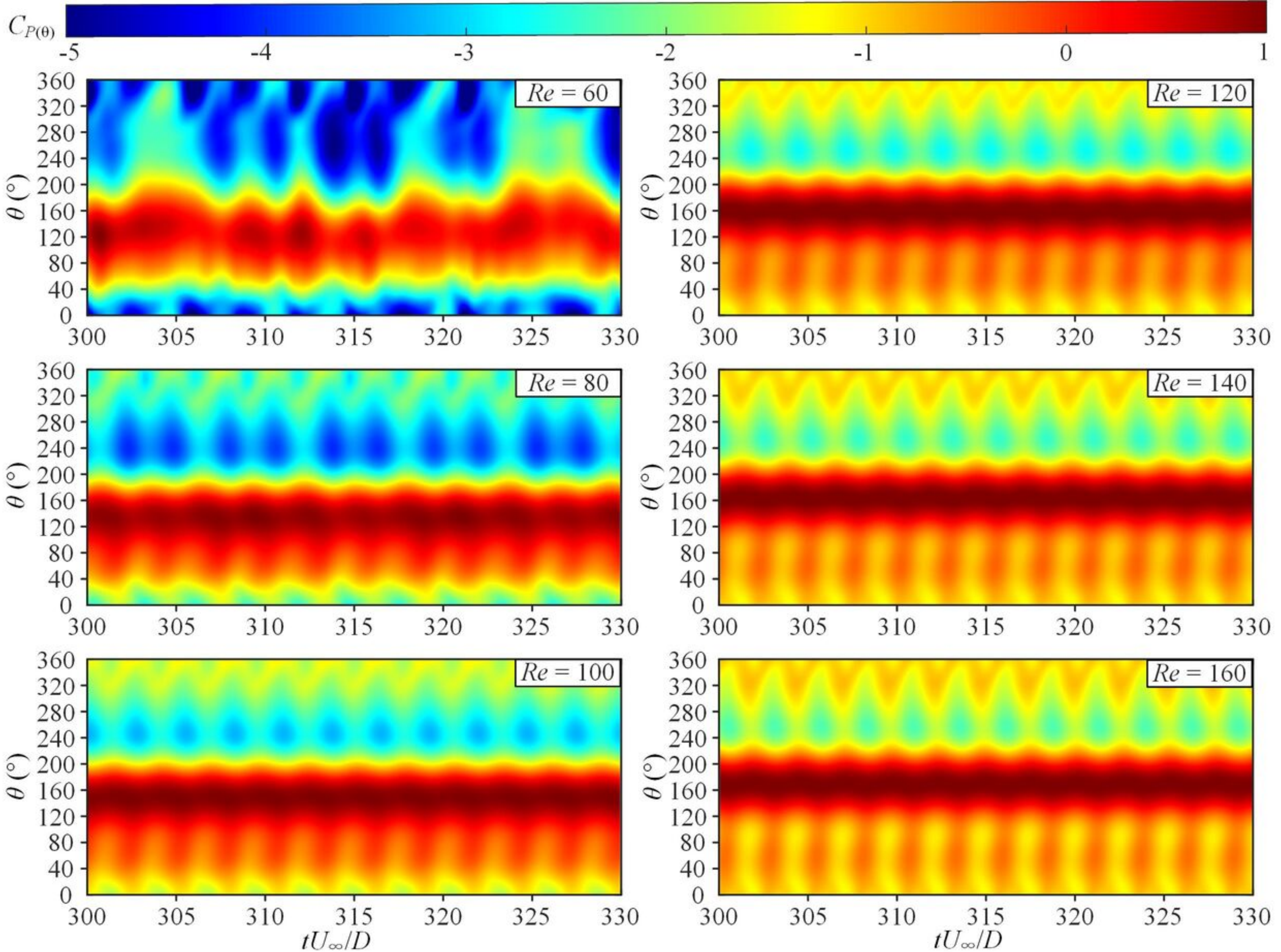

$C_{P(\theta)}$
-5
-4
-3
-2
-1
0
1
Re = 60
Re = 80
Re = 100
Re = 120
Re = 140
Re = 160
θ (°)
360
320
280
240
200
160
120
80
40
0
300
305
310
315
320
325
330
tU_∞/D

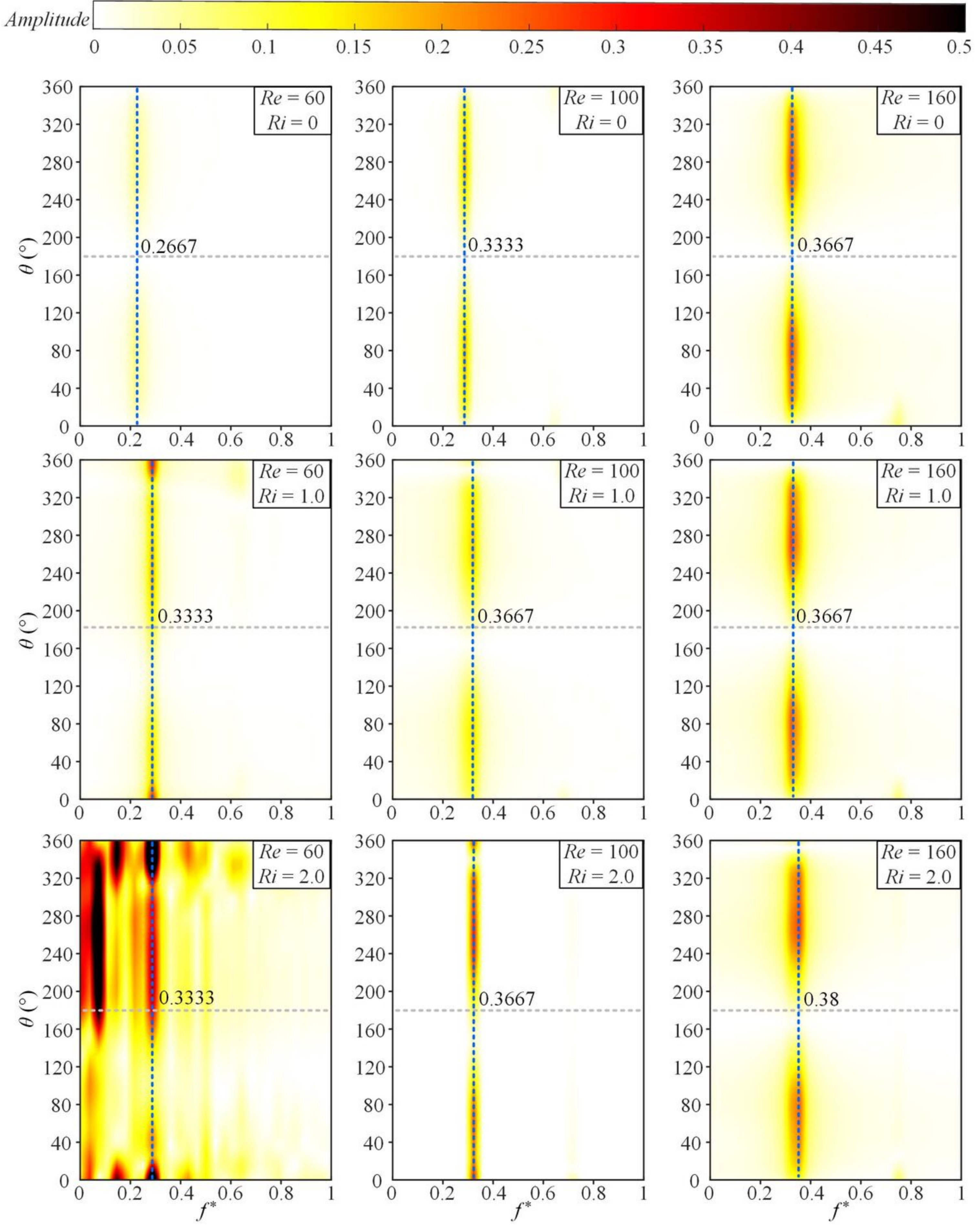

Amplitude
0
0.05
0.1
0.15
0.2
0.25
0.3
0.35
0.4
0.45
0.5
Re = 60
Ri = 0
0.2667
Re = 100
Ri = 0
0.3333
Re = 160
Ri = 0
0.3667
Re = 60
Ri = 1.0
0.3333
Re = 100
Ri = 1.0
0.3667
Re = 160
Ri = 1.0
0.3667
Re = 60
Ri = 2.0
0.3333
Re = 100
Ri = 2.0
0.3667
Re = 160
Ri = 2.0
0.38
θ (°)
f*

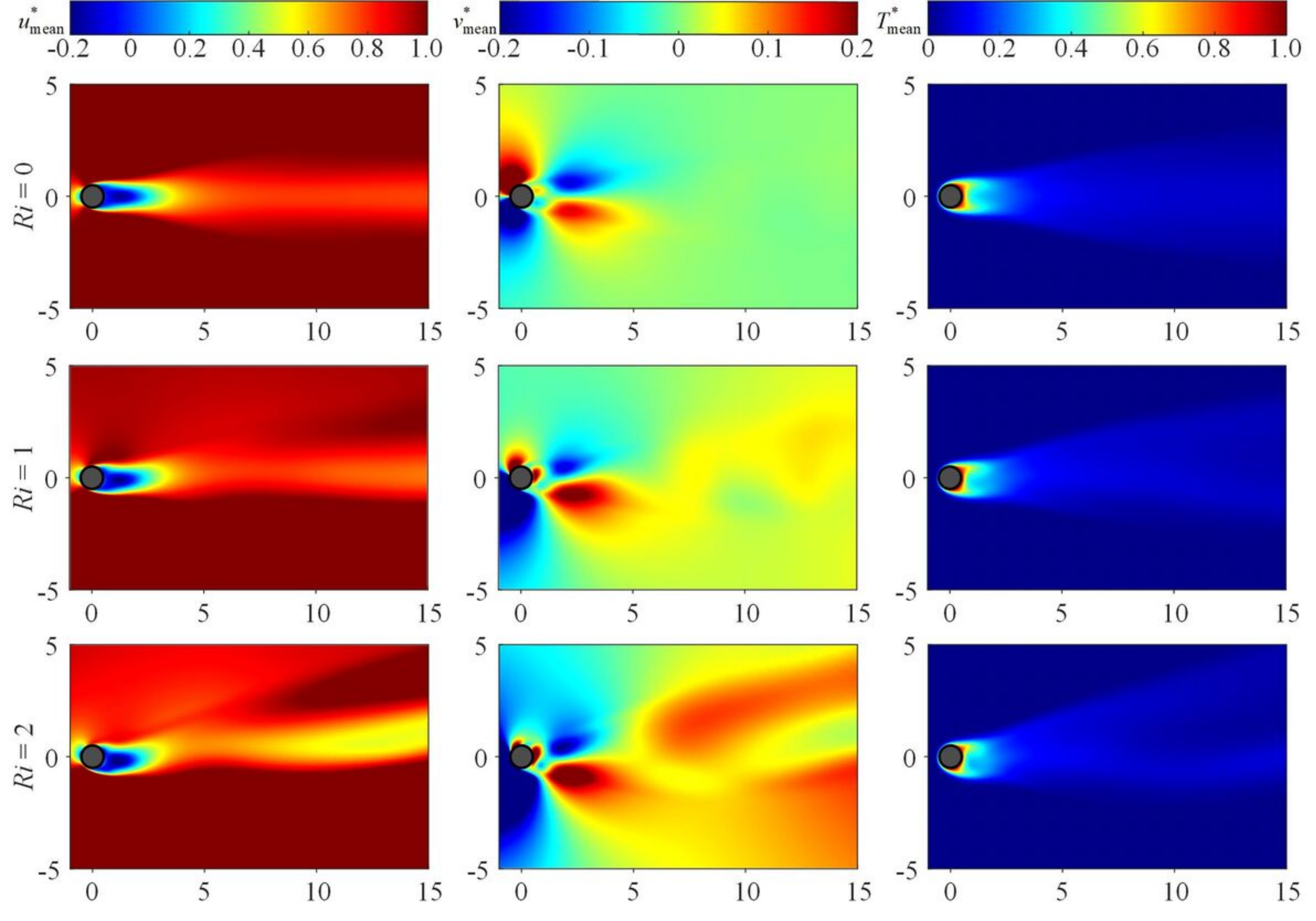

u^*_{mean}
-0.2 0 0.2 0.4 0.6 0.8 1.0
v^*_{mean}
-0.2 -0.1 0 0.1 0.2
T^*_{mean}
0 0.2 0.4 0.6 0.8 1.0
$Ri = 0$
$Ri = 1$
$Ri = 2$
5
0
-5
0 5 10 15

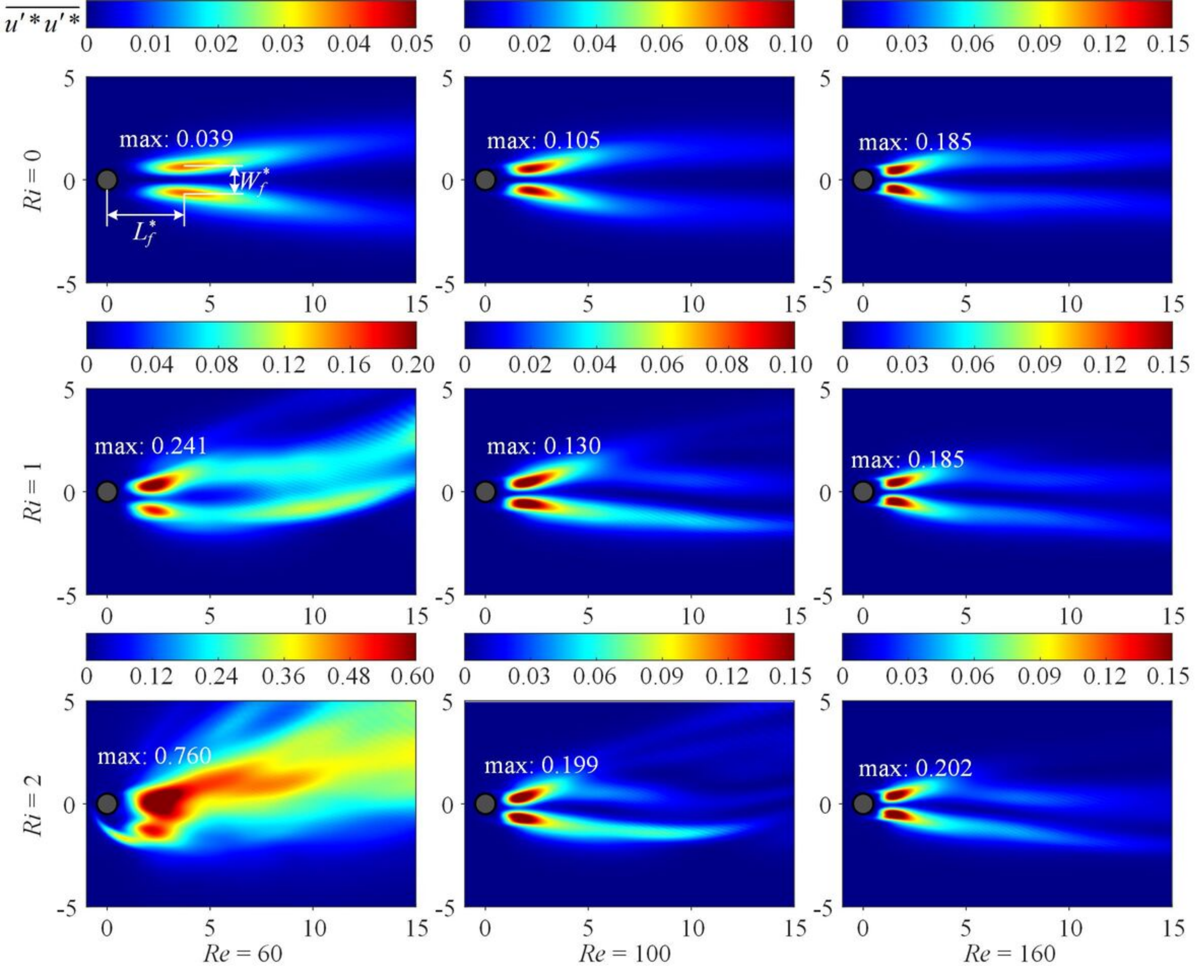

$\overline{u'^*u'^*}$
0 0.01 0.02 0.03 0.04 0.05
0 0.02 0.04 0.06 0.08 0.10
0 0.03 0.06 0.09 0.12 0.15
$Ri = 0$
max: 0.039
W_f^*
L_f^*
max: 0.105
max: 0.185
0 0.04 0.08 0.12 0.16 0.20
0 0.02 0.04 0.06 0.08 0.10
0 0.03 0.06 0.09 0.12 0.15
$Ri = 1$
max: 0.241
max: 0.130
max: 0.185
0 0.12 0.24 0.36 0.48 0.60
0 0.03 0.06 0.09 0.12 0.15
0 0.03 0.06 0.09 0.12 0.15
$Ri = 2$
max: 0.760
max: 0.199
max: 0.202
$Re = 60$
$Re = 100$
$Re = 160$

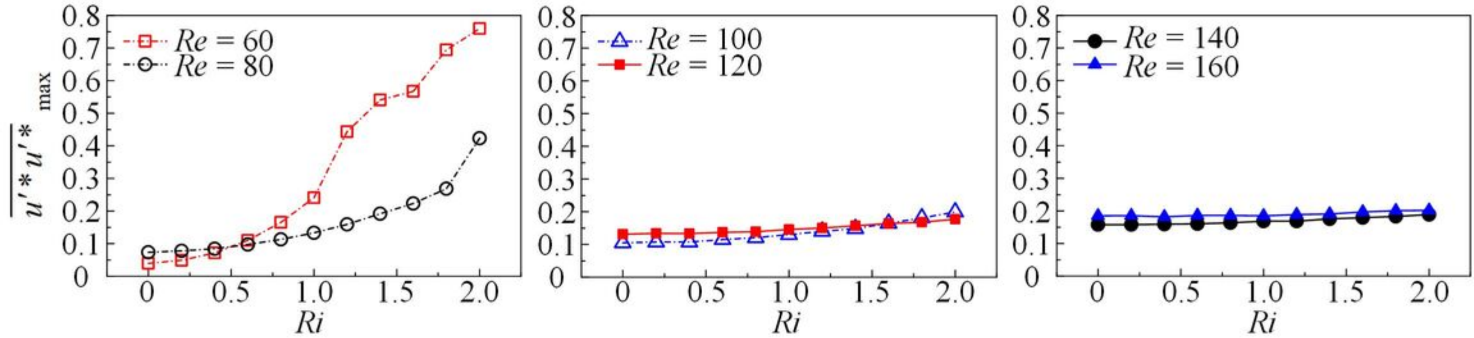

$\overline{u'^*u'^*}_{max}$
Re = 60
Re = 80
Re = 100
Re = 120
Re = 140
Re = 160
Ri
Ri
Ri

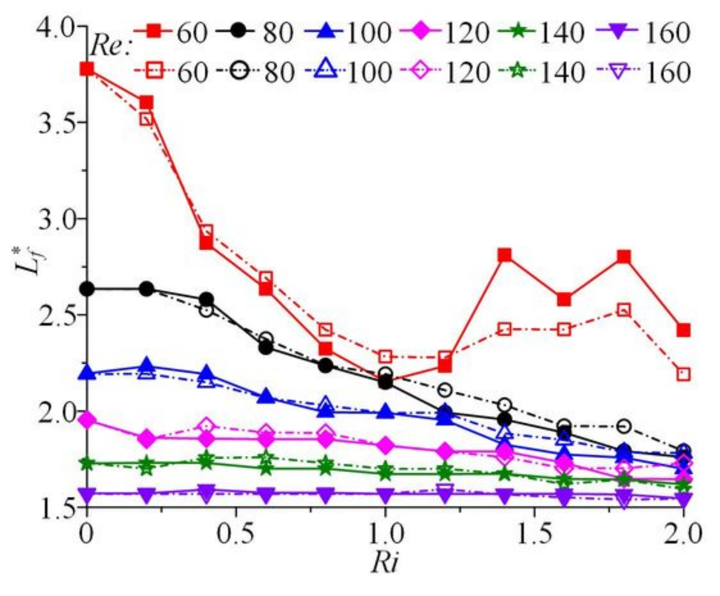

Re:
60
80
100
120
140
160
60
80
100
120
140
160
4.0
3.5
3.0
2.5
2.0
1.5
L_f^*
0
0.5
1.0
1.5
2.0
Ri

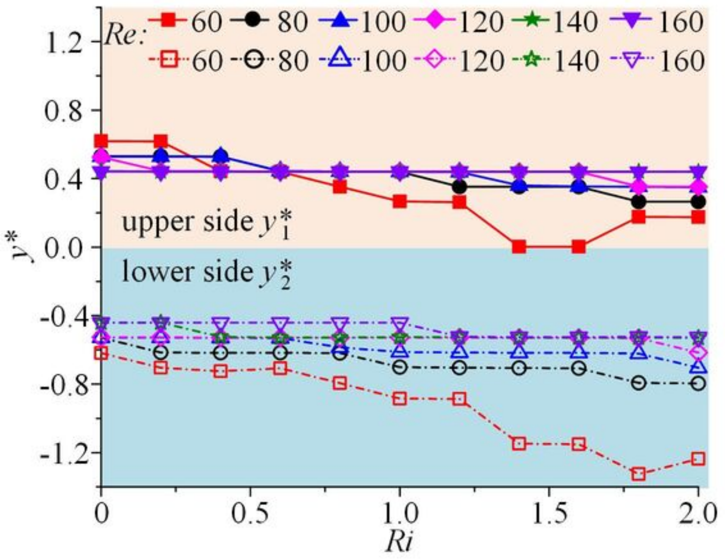

Re:
60
80
100
120
140
160
60
80
100
120
140
160
1.2
0.8
0.4
0.0
-0.4
-0.8
-1.2
upper side y_1^*
lower side y_2^*
y^*
0
0.5
1.0
1.5
2.0
Ri

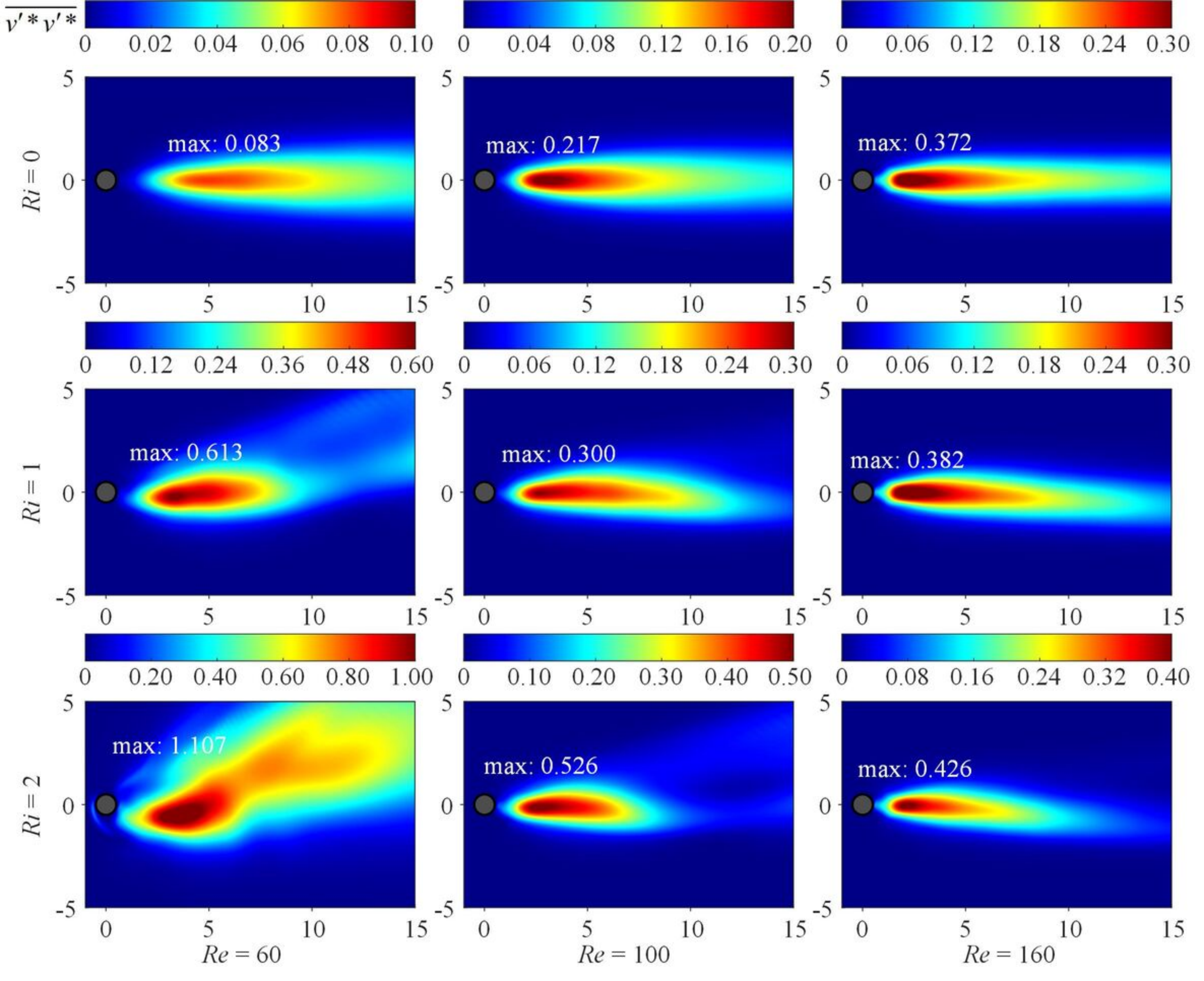

$\overline{v'^* v'^*}$
0 0.02 0.04 0.06 0.08 0.10
0 0.04 0.08 0.12 0.16 0.20
0 0.06 0.12 0.18 0.24 0.30
max: 0.083
max: 0.217
max: 0.372
0 0.12 0.24 0.36 0.48 0.60
0 0.06 0.12 0.18 0.24 0.30
0 0.06 0.12 0.18 0.24 0.30
max: 0.613
max: 0.300
max: 0.382
0 0.20 0.40 0.60 0.80 1.00
0 0.10 0.20 0.30 0.40 0.50
0 0.08 0.16 0.24 0.32 0.40
max: 1.107
max: 0.526
max: 0.426
$Ri = 0$
$Ri = 1$
$Ri = 2$
$Re = 60$
$Re = 100$
$Re = 160$

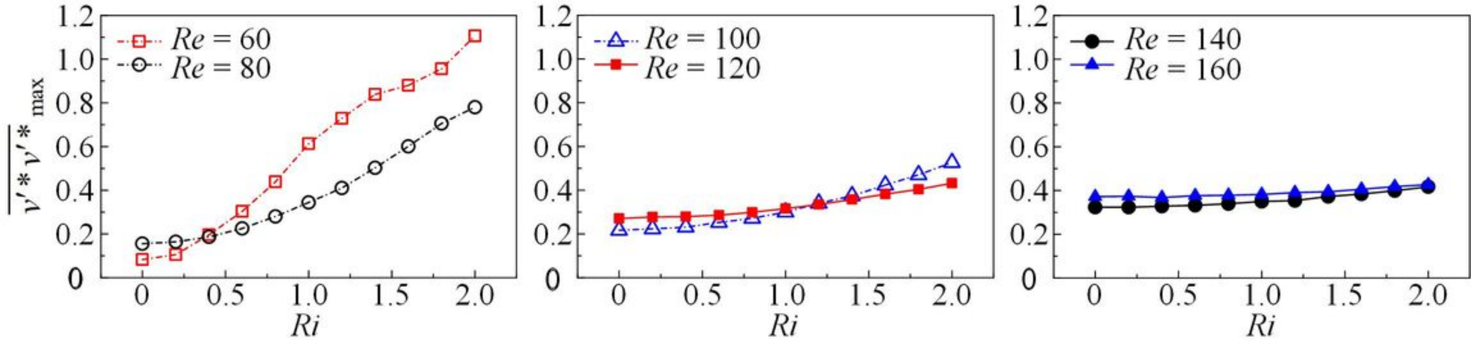

Re = 60
Re = 80
Re = 100
Re = 120
Re = 140
Re = 160
$\overline{v'^* v'^*}_{\max}$
Ri

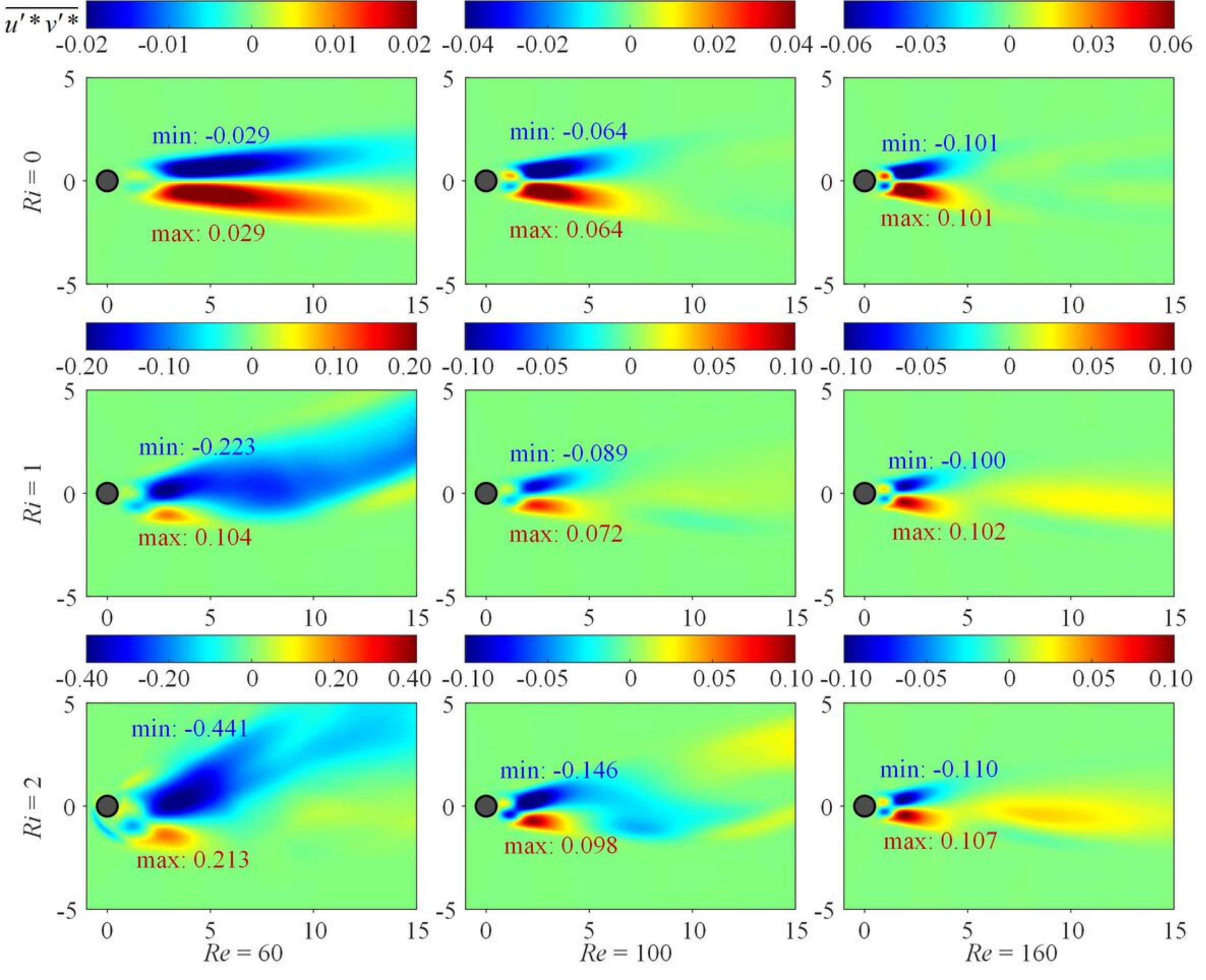

$\overline{u'^* v'^*}$
Ri = 0
Ri = 1
Ri = 2
min: -0.029
max: 0.029
min: -0.064
max: 0.064
min: -0.101
max: 0.101
min: -0.223
max: 0.104
min: -0.089
max: 0.072
min: -0.100
max: 0.102
min: -0.441
max: 0.213
min: -0.146
max: 0.098
min: -0.110
max: 0.107
Re = 60
Re = 100
Re = 160

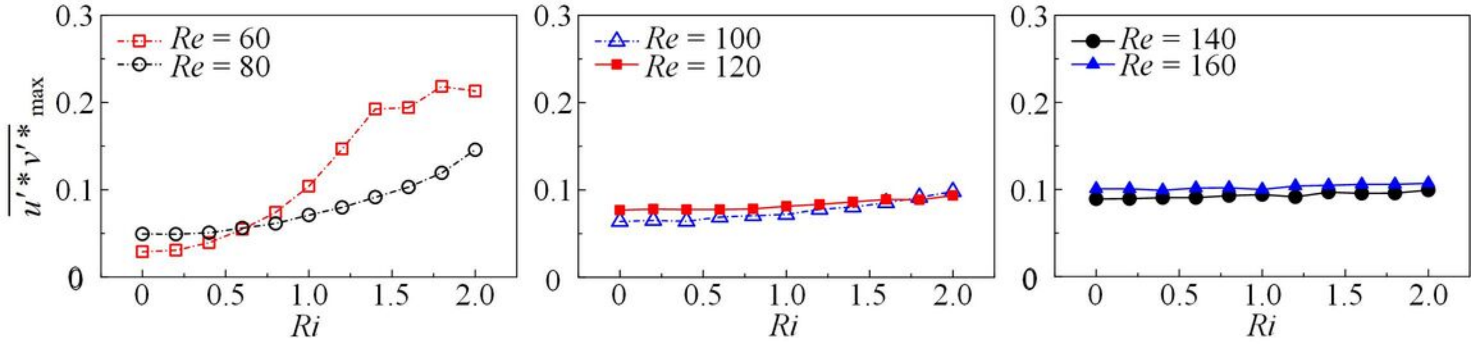

Re = 60
Re = 80
Re = 100
Re = 120
Re = 140
Re = 160
Ri
Ri
Ri
0.3
0.2
0.1
0
0.5
1.0
1.5
2.0

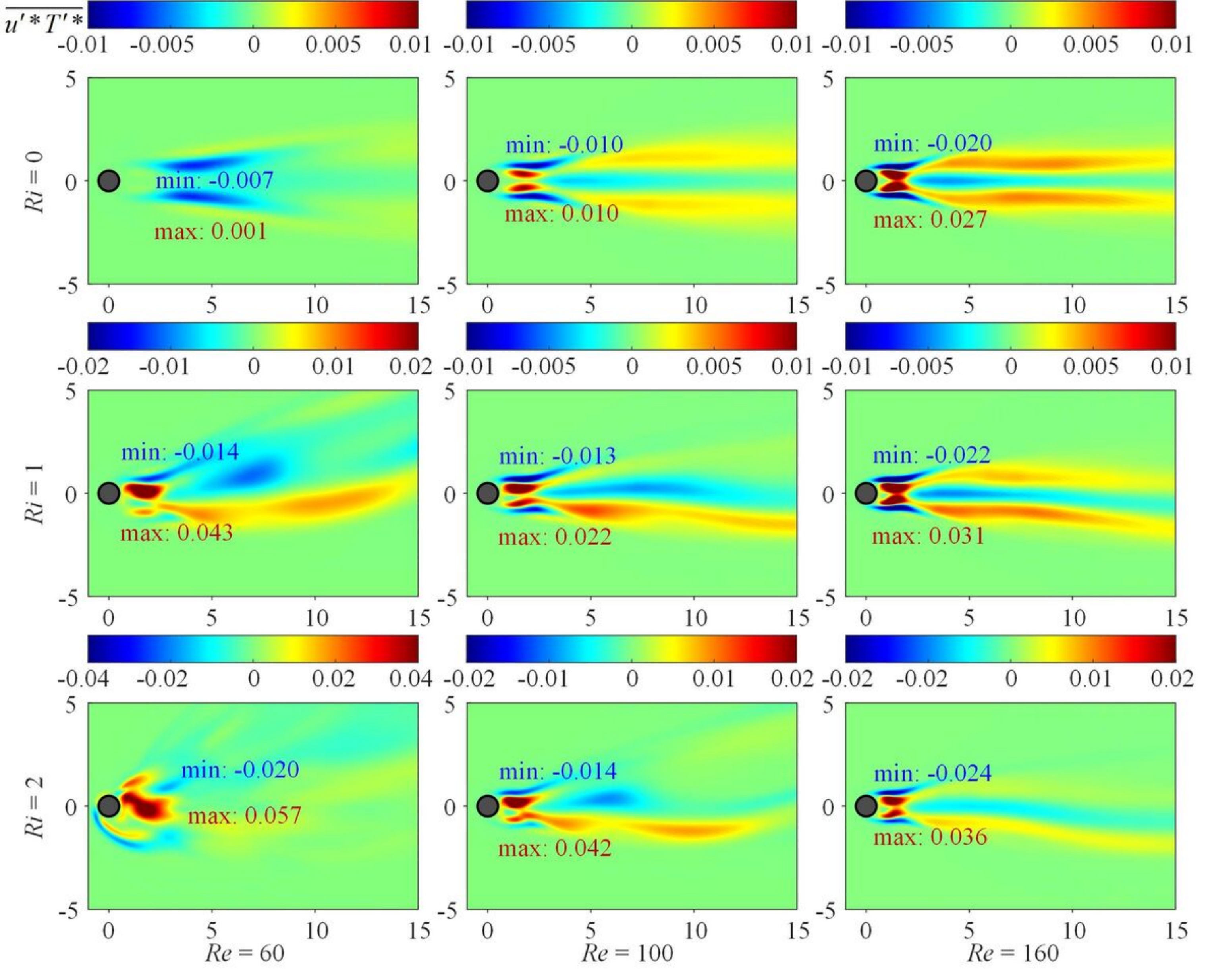

$\overline{u'*T'*}$
-0.01 -0.005 0 0.005 0.01
min: -0.007
max: 0.001
min: -0.010
max: 0.010
min: -0.020
max: 0.027
-0.02 -0.01 0 0.01 0.02
min: -0.014
max: 0.043
min: -0.013
max: 0.022
min: -0.022
max: 0.031
-0.04 -0.02 0 0.02 0.04
-0.02 -0.01 0 0.01 0.02
-0.02 -0.02 0 0.01 0.02
min: -0.020
max: 0.057
min: -0.014
max: 0.042
min: -0.024
max: 0.036
$Ri = 0$
$Ri = 1$
$Ri = 2$
$Re = 60$
$Re = 100$
$Re = 160$

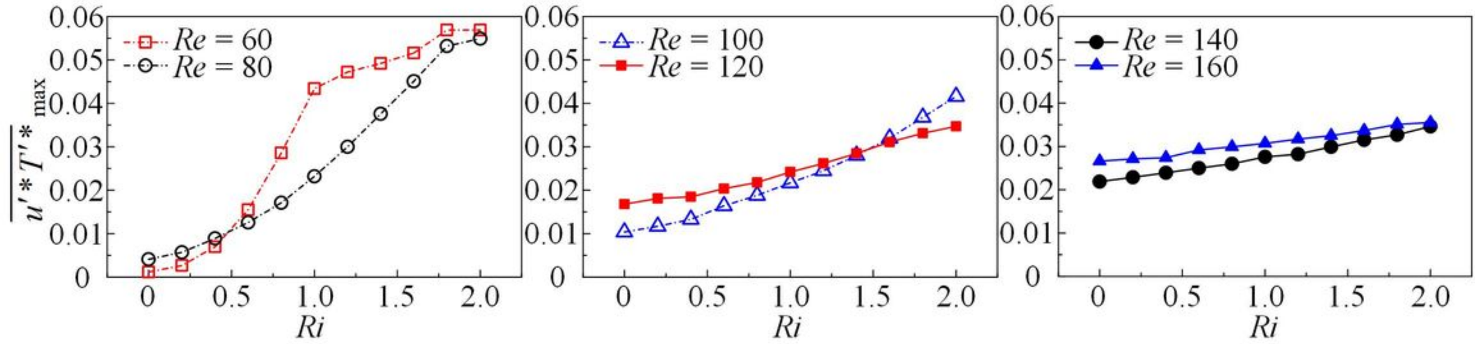

$\overline{u'^*T'^*}_{max}$
0.06
0.05
0.04
0.03
0.02
0.01
0
Re = 60
Re = 80
Re = 100
Re = 120
Re = 140
Re = 160
0
0.5
1.0
1.5
2.0
Ri

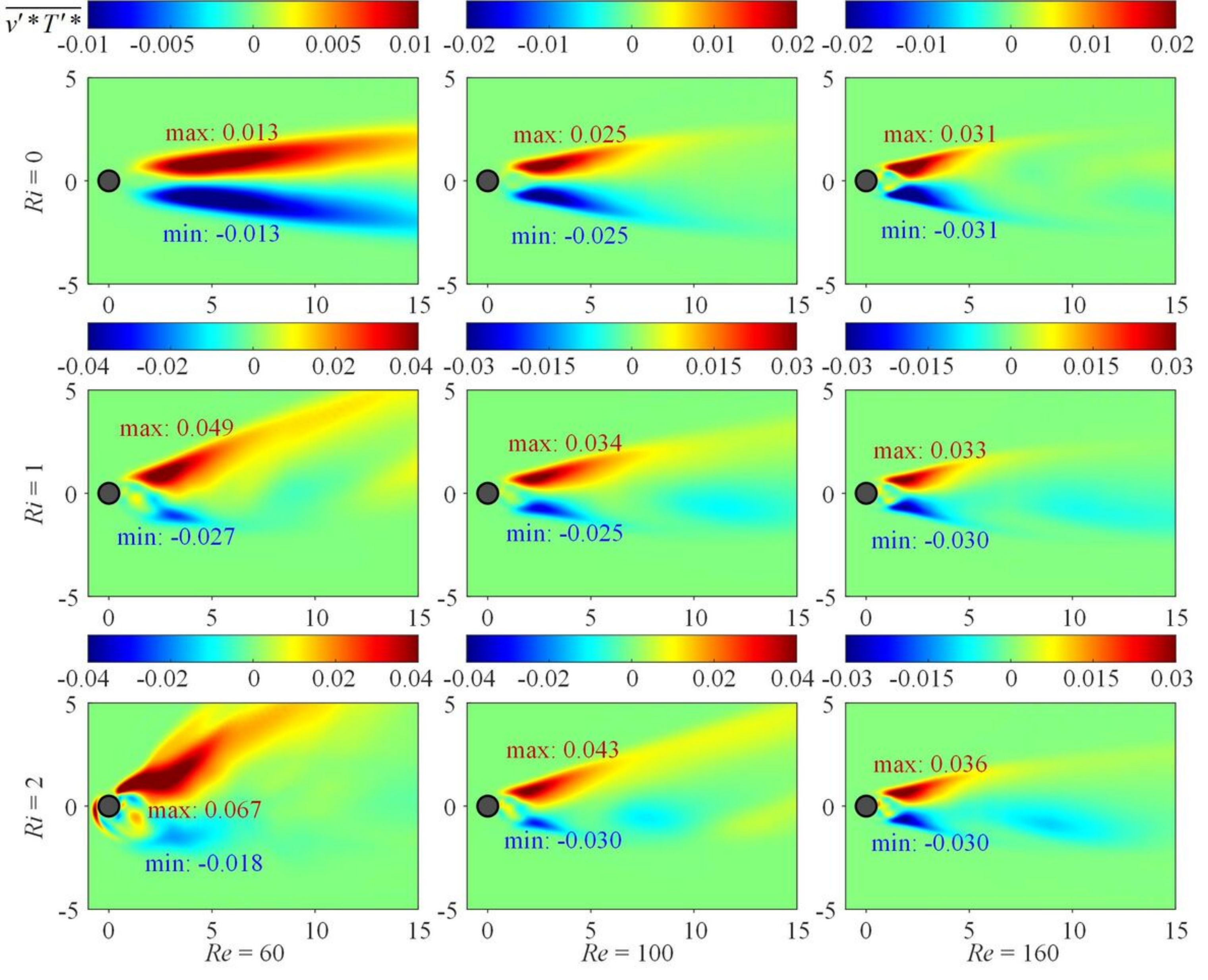

$\overline{v'*T'*}$
max: 0.013
min: -0.013
max: 0.025
min: -0.025
max: 0.031
min: -0.031
max: 0.049
min: -0.027
max: 0.034
min: -0.025
max: 0.033
min: -0.030
max: 0.067
min: -0.018
max: 0.043
min: -0.030
max: 0.036
min: -0.030
$Ri = 0$
$Ri = 1$
$Ri = 2$
$Re = 60$
$Re = 100$
$Re = 160$

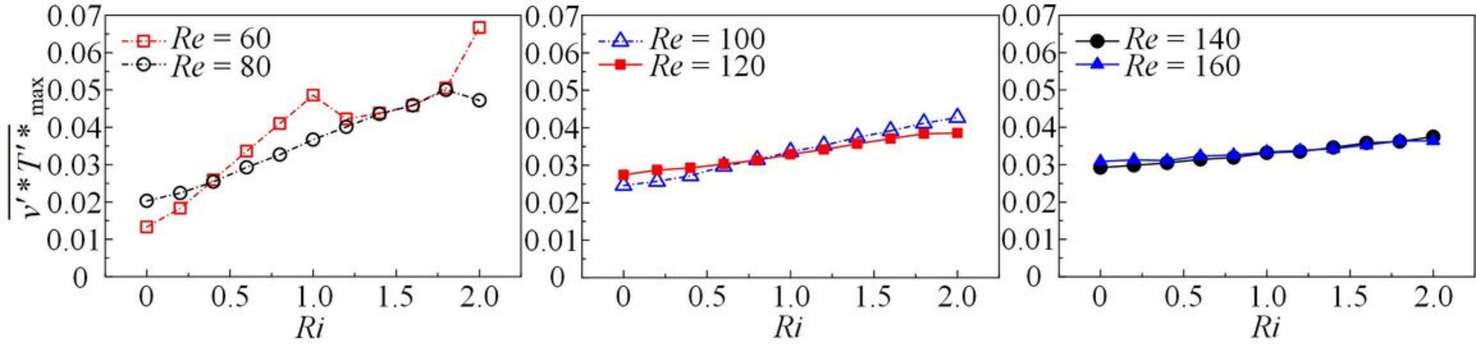

$\overline{v'^*T'^*}_{\max}$
Re = 60
Re = 80
Re = 100
Re = 120
Re = 140
Re = 160
0.07
0.06
0.05
0.04
0.03
0.02
0.01
0
0
0.5
1.0
1.5
2.0
Ri

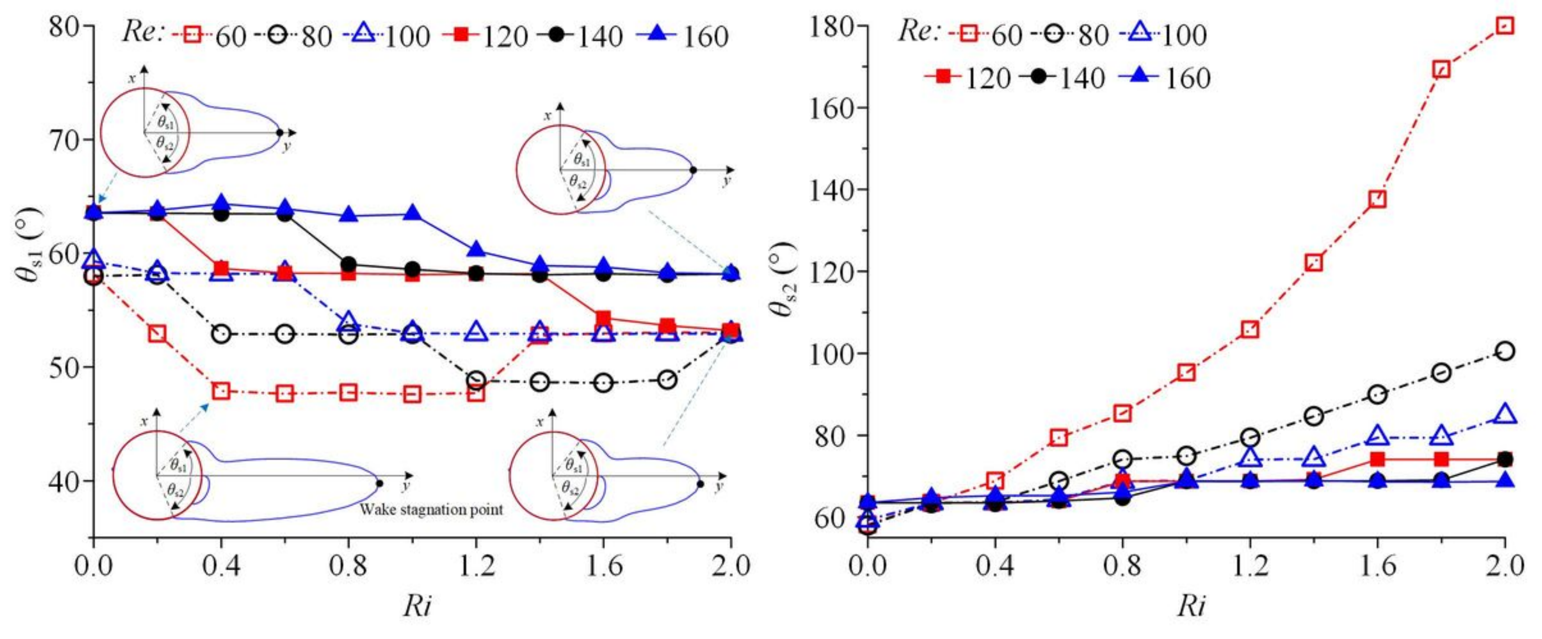

Re: 60 80 100 120 140 160
θ_{s1} (°)
θ_{s2} (°)
Ri
x
y
θ_{s1}
θ_{s2}
Wake stagnation point

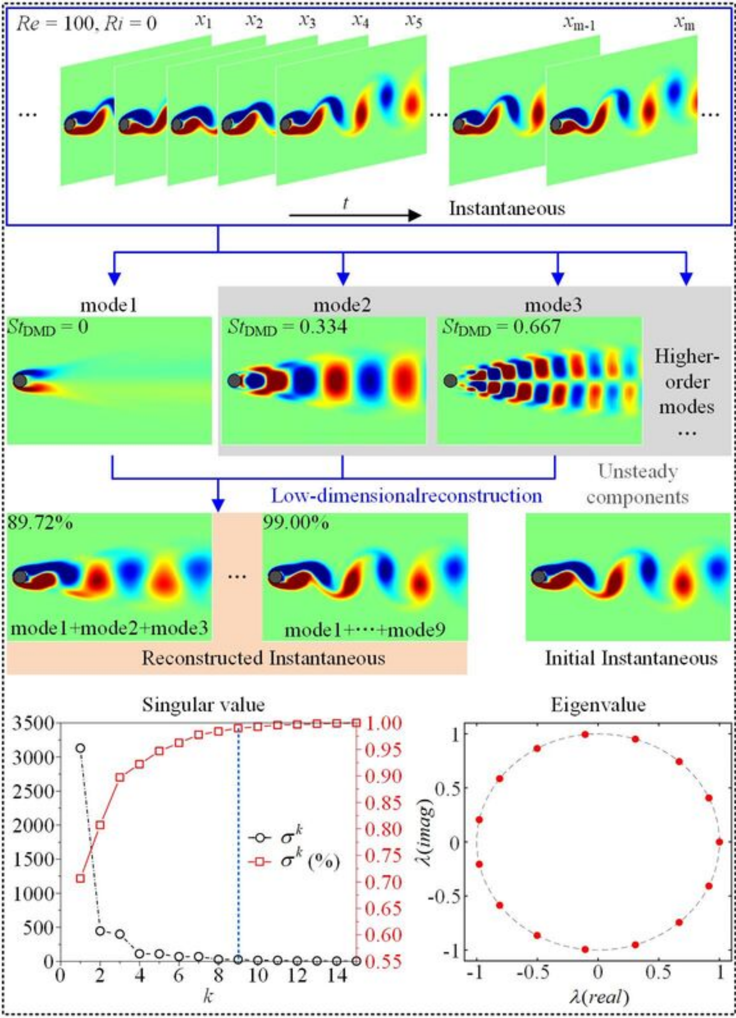

Re = 100, Ri = 0
x1 x2 x3 x4 x5 xm-1 xm
t
Instantaneous
mode1
StDMD = 0
mode2
StDMD = 0.334
mode3
StDMD = 0.667
Higher-order modes
Unsteady components
Low-dimensionalreconstruction
89.72%
mode1+mode2+mode3
99.00%
mode1+⋯+mode9
Reconstructed Instantaneous
Initial Instantaneous
Singular value
σ^k
σ^k (%)
k
Eigenvalue
λ(imag)
λ(real)

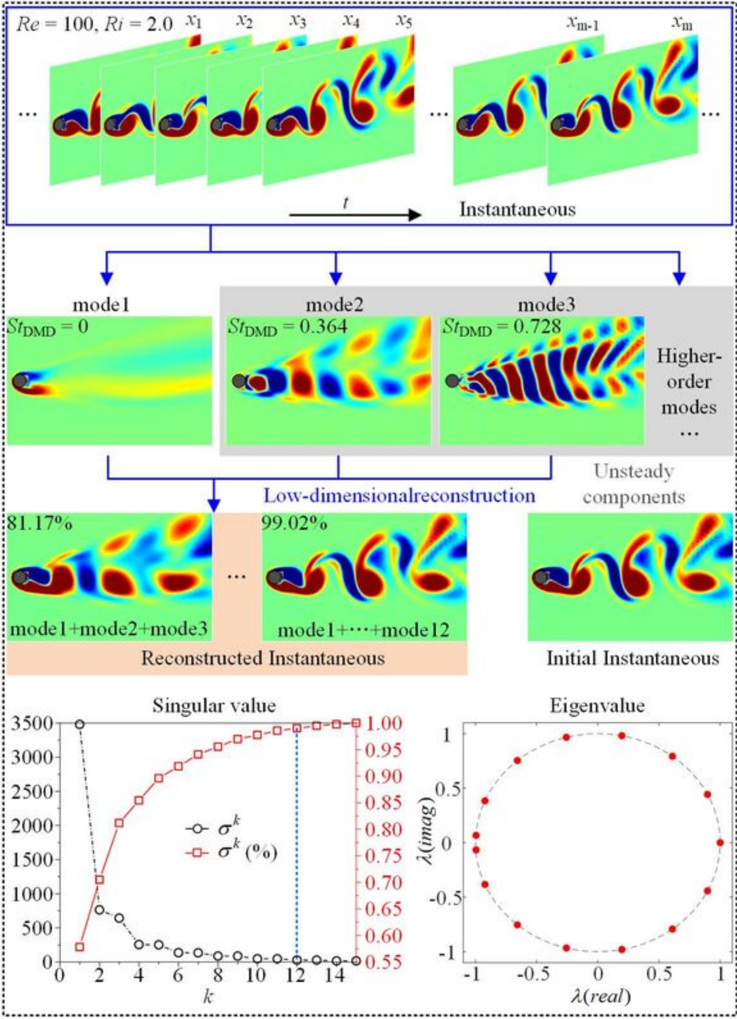

Re = 100, Ri = 2.0
x1 x2 x3 x4 x5 xm-1 xm
t
Instantaneous
mode1
StDMD = 0
mode2
StDMD = 0.364
mode3
StDMD = 0.728
Higher-order modes
...
Unsteady components
Low-dimensionalreconstruction
81.17%
mode1+mode2+mode3
99.02%
mode1+⋯+mode12
Reconstructed Instantaneous
Initial Instantaneous
Singular value
σ^k
σ^k (%)
k
Eigenvalue
λ(imag)
λ(real)

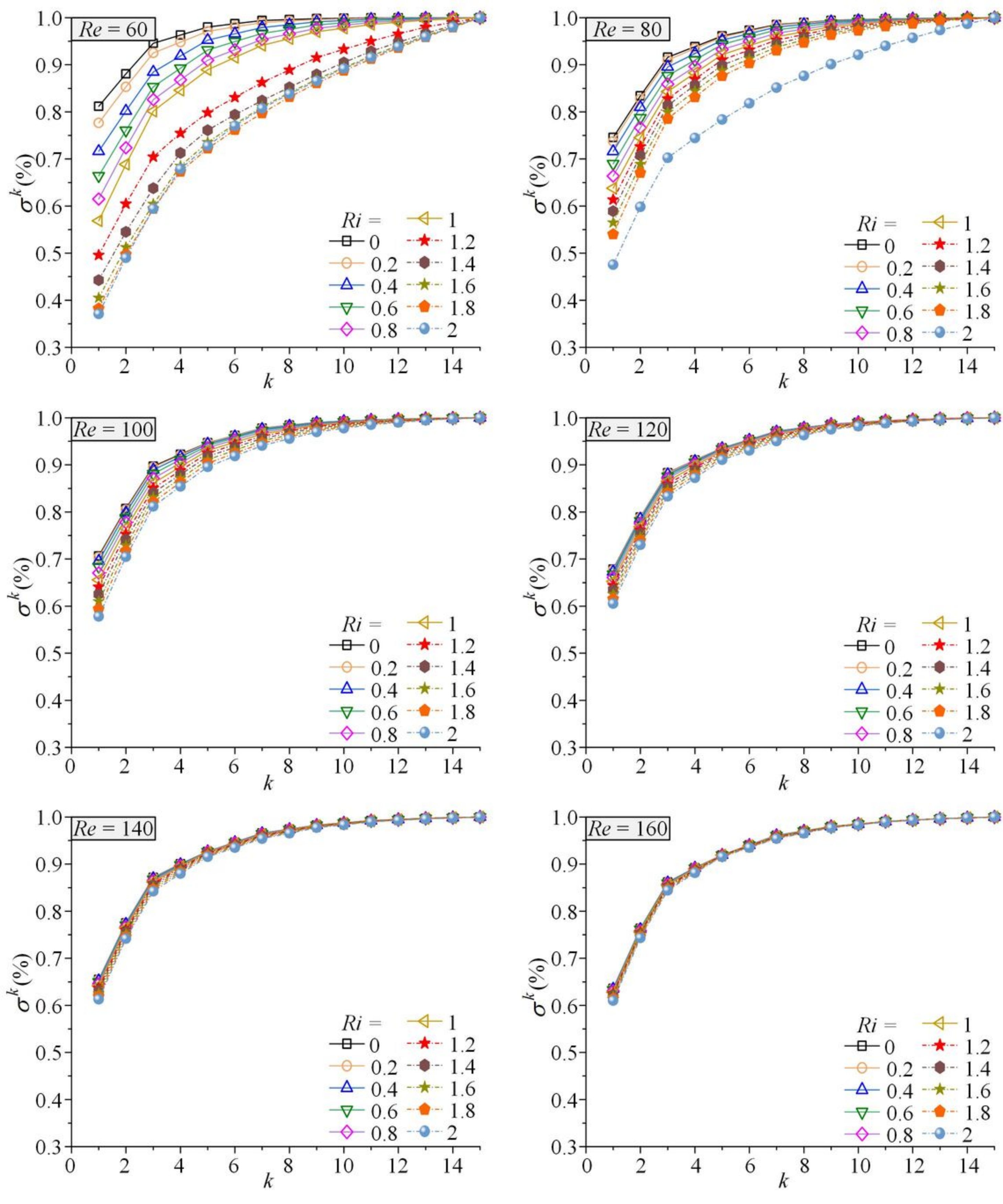

Re = 60
Re = 80
Re = 100
Re = 120
Re = 140
Re = 160
σ^k (%)
k
Ri =
0
0.2
0.4
0.6
0.8
1
1.2
1.4
1.6
1.8
2

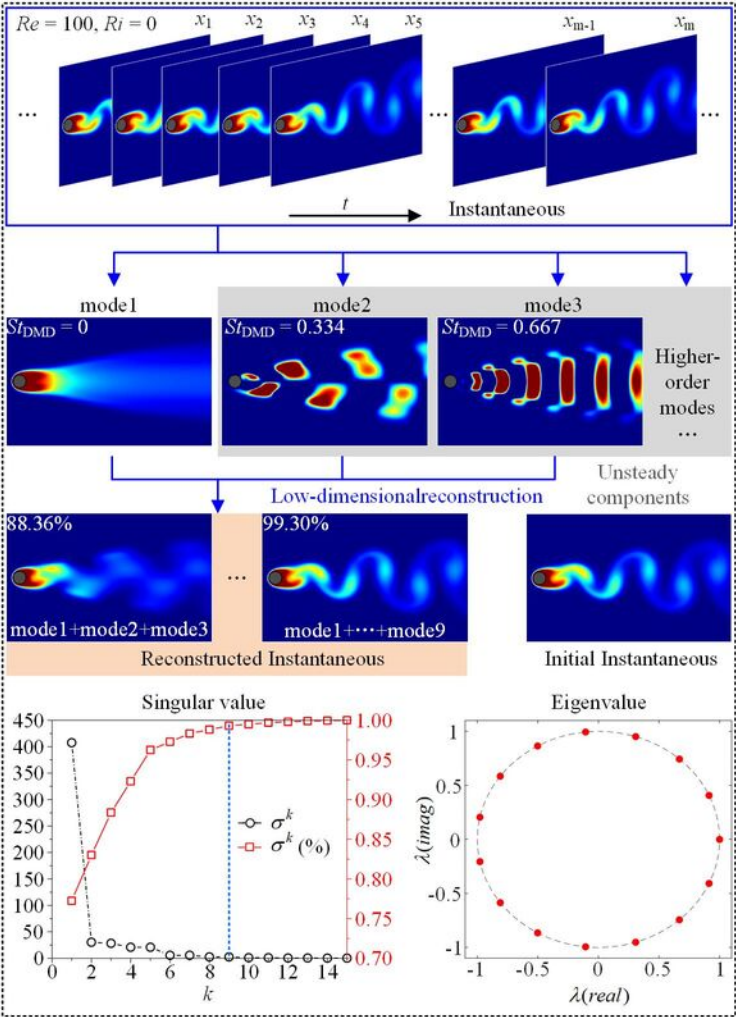

Re = 100, Ri = 0
x1
x2
x3
x4
x5
xm-1
xm
t
Instantaneous
mode1
StDMD = 0
mode2
StDMD = 0.334
mode3
StDMD = 0.667
Higher-order modes
Unsteady components
Low-dimensionalreconstruction
88.36%
mode1+mode2+mode3
99.30%
mode1+⋯+mode9
Reconstructed Instantaneous
Initial Instantaneous
Singular value
σk
σk (%)
k
Eigenvalue
λ(imag)
λ(real)

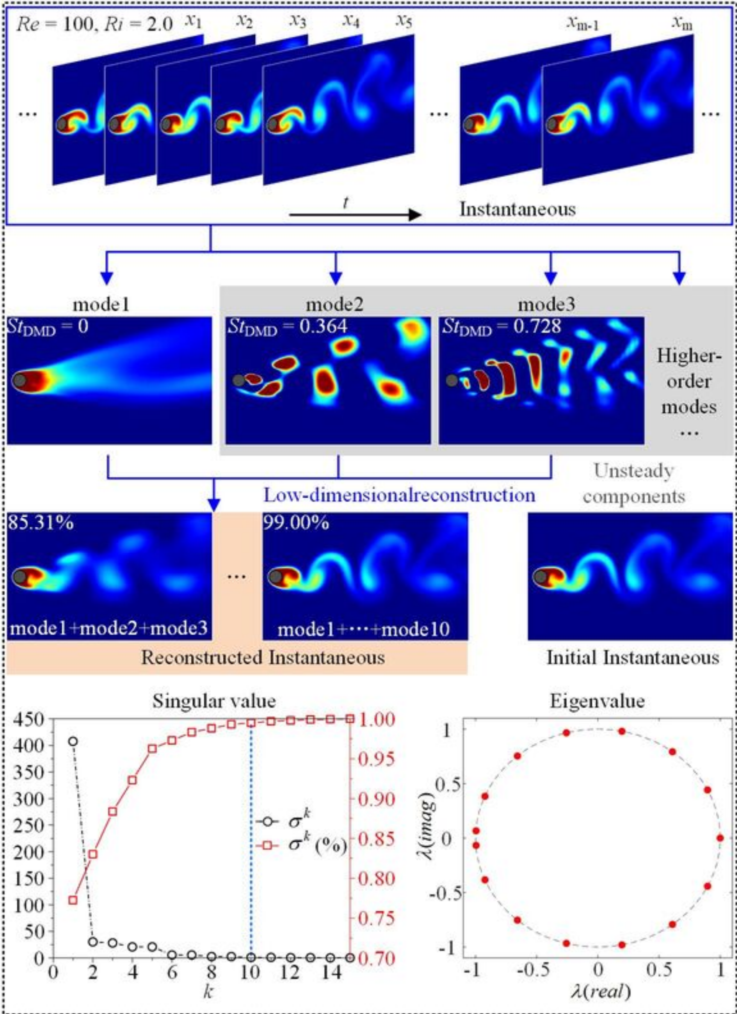

Re = 100, Ri = 2.0
x1
x2
x3
x4
x5
xm-1
xm
t
Instantaneous
mode1
St_DMD = 0
mode2
St_DMD = 0.364
mode3
St_DMD = 0.728
Higher-order modes
...
Unsteady components
Low-dimensionalreconstruction
85.31%
mode1+mode2+mode3
99.00%
mode1+⋯+mode10
Reconstructed Instantaneous
Initial Instantaneous
Singular value
σ^k
σ^k (%)
k
Eigenvalue
λ(imag)
λ(real)

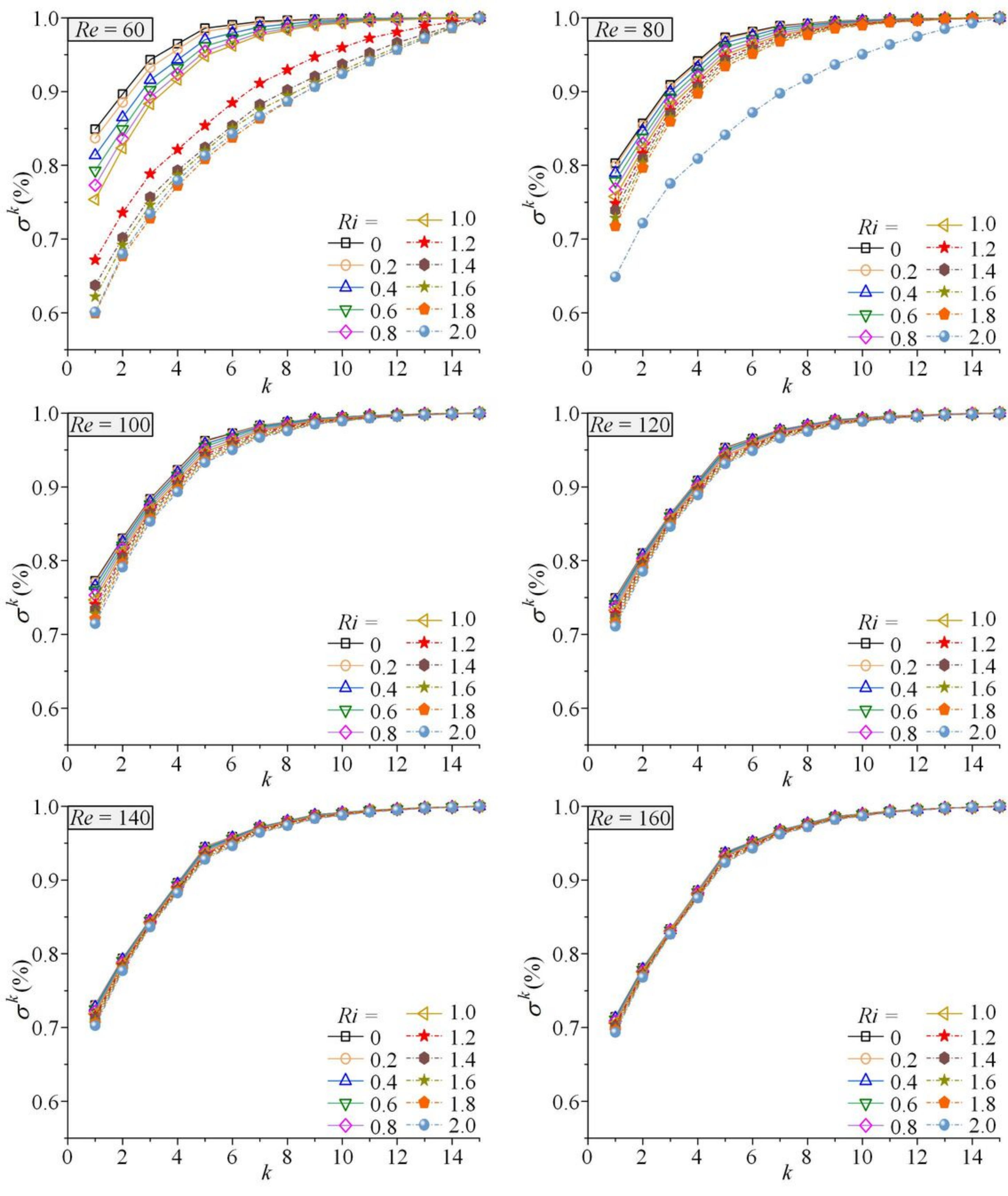

Re = 60
Re = 80
Re = 100
Re = 120
Re = 140
Re = 160
σ^k(%)
k
Ri =
0
0.2
0.4
0.6
0.8
1.0
1.2
1.4
1.6
1.8
2.0